Available online at www.sciencedirect.com
ScienceDirect
Comput. Methods Appl. Mech. Engrg. 354 (2019) 56–95
Computer methods in applied mechanics and engineering
www.elsevier.com/locate/cma

A micromorphically regularized Cam-clay model for capturing size-dependent anisotropy of geomaterials

Eric C. Bryant, WaiChing Sun*

Department of Civil Engineering and Engineering Mechanics, Columbia University, 614 SW Mudd, Mail Code: 4709, New York, NY 10027, United States

Received 30 January 2019; received in revised form 7 May 2019; accepted 7 May 2019
Available online 16 May 2019

Abstract

We introduce a regularized anisotropic modified Cam-clay (MCC) model which captures the size-dependent anisotropic elastoplastic responses for clay, mudstone, shales, and sedimentary rock. By homogenizing the multiscale anisotropic effects induced by clay particle aggregate, clusters, peds, micro-fabric, and mineral contact across length scales, we introduce two distinctive anisotropic mechanisms for the MCC model at the material point and mesoscale levels. We first employ a mapping that links the anisotropic stress state to a fictitious isotropic principal stress-space to introduce anisotropy at the material point scale. Then, the mesoscale anisotropy is introduced via an anisotropic regularization mechanism. This anisotropic regularization mechanism is triggered by introducing gradient-dependence of the internal variables through a penalty method such that the resultant gradient-enhanced plastic flow may exhibit anisotropic responses non-coaxial to the stress gradient of the yield function. The influence of the size-dependent anisotropy on the formation of the shear band and the macroscopic responses of the effective media are analyzed in 2D and 3D numerical examples.

Keywords: Gradient critical state plasticity; Micromorphic regularization; Size-dependent anisotropy

1. Introduction

Clay, mudstone and shales are materials that exhibit different anisotropic response across different length scales. This scale-dependent anisotropy originates from the fabric and microstructures of clay platelet and other fragments of minerals such as quartz and calcite. At the nanoscale, clay particles may aggregate together in sub-microscopic fabric units, which is often referred as domains. These domains then form clusters, which in return form peds that are large enough to be visible. Together with other features, such as joints and fissures, the peds then form a microfabric system that is inherently anisotropic. As shown in Fig. 1 (cf. [1] snf [2]), the anisotropy of clay and crystalline rock is often not just manifested by a single morphological feature (e.g. bedding orientation, inclusion of different materials). Instead, the anisotropy of the material response s is the consequence of multiple microstructural mechanisms that may differ for effective media of different sampling sizes [3].

* Corresponding author.
E-mail address: wsun@columbia.edu (W. Sun).

https://doi.org/10.1016/j.cma.2019.05.003
0045-7825/

Nomenclature

Field variables

$\boldsymbol{u}$	Displacement field
$\tilde{\epsilon}_v^{\mathrm{p}}$	Projected volumetric plastic strain field
$\tilde{\lambda}$	Projected equivalent plastic strain field

Local and internal variables

$\boldsymbol{n}$	Plastic strain direction
p	Pressure
q	Deviatoric stress invariant
$\boldsymbol{\epsilon}$	Strain
$\boldsymbol{\epsilon}^{\mathrm{e}}$	Elastic strain
$\boldsymbol{\epsilon}^{\mathrm{p}}$	Plastic strain
ϵ_v^{p}	Volumetric plastic strain
λ	Equivalent plastic strain, the time integration of the incremental plastic multiplier
$\boldsymbol{\sigma}$	Stress
σ_p	Pressure-like plastic internal variable
σ_q	Deviatoric stress invariant-like plastic internal variable

Elastic parameters

$\boldsymbol{C}^{\mathrm{e}}$	Elastic tangent described by elastic material parameters E, $E_{\boldsymbol{l}}$, $\mu_{\boldsymbol{l}}$, ν, $\nu_{\boldsymbol{l}}$, and the microstructural direction via the Walpole algebra
E	Young's modulus in the isotropic plane described by $\boldsymbol{\chi}$
$\boldsymbol{E}_1$	Symmetric element of the Walpole algebra
$\boldsymbol{E}_2$	Symmetric element of the Walpole algebra
$\boldsymbol{E}_3$	Element of the Walpole algebra
$\boldsymbol{E}_4$	Element of the Walpole algebra
$E_{\boldsymbol{l}}$	Young's modulus in the isotropic plane's normal direction described by $\boldsymbol{\phi}$
$\boldsymbol{F}$	Symmetric element of the Walpole algebra
$\boldsymbol{G}$	Symmetric element of the Walpole algebra
$\boldsymbol{l}$	Microstructural direction unit vector
$\boldsymbol{\phi}$	Microstructural tensorial out-of-plane direction
$\boldsymbol{\chi}$	Microstructural tensorial in-plane direction
$\mu_{\boldsymbol{l}}$	Shear modulus characterizing in-plane shear stress due to shear strain in the microstructural direction
ν	Poisson ratio characterizing transverse in-plane contraction due to tension applied in the perpendicular direction within the plane of isotropy
$\nu_{\boldsymbol{l}}$	Poisson ratio characterizing transverse in-plane contraction due to tension applied in the microstructural direction

Plastic parameters

C_c	Compressibility index
C_r	Re-compressibility index
M	Slope of the critical state line
p_c	Preconsolidation pressure
$\boldsymbol{P}^{\mathrm{p\ dev}}$	Deviatoric plastic map, described by coefficients α^{dev}, β^{dev}, γ^{dev}, and the microstructural direction via the symmetric Walpole subalgebra

$\boldsymbol{P}^{\text{p vol}}$	Volumetric plastic map, described by coefficients α^{vol}, β^{vol}, γ^{dev}, and the microstructural direction via the symmetric Walpole subalgebra
α^{dev}	Deviatoric plastic map coefficient
α^{vol}	Volumetric plastic map coefficient
β^{dev}	Deviatoric plastic map coefficient
β^{vol}	Volumetric plastic map coefficient
γ^{dev}	Deviatoric plastic map coefficient
γ^{vol}	Volumetric plastic map coefficient
Micromorphic parameters	
l_v	Length scale for projected volumetric plastic strain
$\boldsymbol{l}_v$	Unit vector used to construct the anisotropic diffusivity tensor of the projected volumetric plastic strain
l_λ	Length scale for projected equivalent plastic strain
$\boldsymbol{l}_\lambda$	Unit vector used to construct the anisotropic diffusivity tensor of the projected equivalent plastic strain
k_v	Penalty stiffness for the discrepancy between local and projected volumetric plastic strain
k_λ	Relaxation stiffness for the discrepancy between local and projected equivalent plastic strain
K_v	Regularization stiffness for the projected volumetric plastic strain
K_λ	Regularization stiffness for the projected equivalent plastic strain
ϕ_v	Diffusion tensor coefficient for the projected volumetric plastic strain
$\boldsymbol{\phi}_v$	Tensorial out-of-plane direction used to construct the diffusivity tensor for the projected equivalent plastic strain
ϕ_λ	Diffusion tensor coefficient for the projected equivalent plastic strain
$\boldsymbol{\phi}_\lambda$	Tensorial out-of-plane direction used to construct the diffusivity tensor for the projected equivalent plastic strain
χ_v	Volumetric diffusion tensor coefficient
$\boldsymbol{\chi}_v$	Volumetric tensorial in-plane direction, described by volumetric diffusion direction
χ_λ	Diffusion tensor coefficient for the projected equivalent plastic strain
$\boldsymbol{\chi}_\lambda$	Tensorial in-plane direction used to construct the diffusivity tensor for the projected equivalent plastic strain

Furthermore, size effects are also related to the statistical distribution in the severity of flaws. For instance, Weibull's theory predicts that the stress that triggered fracture is proportional to the $V^{1/\beta}$ where V is the volume of the specimen and β is a material constant [4]. On the other hand, experimental observations of size dependence in geological materials have been reported in uniaxial compression and in Brazilian tests [5,6]. In general, these tests often lead to the conclusion that shear strength consistently decreases with increasing dimensions. However, it is important to note that the size-dependent effect is often more profound when a sharp stress gradient presents due to the loading conditions (e.g., punch and indentation tests). This size dependence might also be suppressed when the confining pressure increases [7], but is of great importance in the brittle regime.

The major contribution of this work is the introduction of non-coaxial micromorphic regularization for the anisotropic MCC model. This treatment enables us to represent the distinct anisotropic characteristics at the particle and aggregate scales, via two mathematical treatments – (1) by introducing mapping tensor at the constitutive laws following Semnani et al. [8] and (2) by introducing anisotropic micromorphic regularization via a penalty or relaxation functional following Forest [9], Miehe et al. [10] and Forest et al. [11]. The introduction of the map greatly simplifies the implementation of anisotropic constitutive laws, as demonstrated in previous works such as Semnani et al. [8] and Bennett et al. [12]. Meanwhile, we introduce the anisotropic regularization by a variational model in which an Euler–Lagrange equation leads to the incremental update of the local constitutive law and two sets

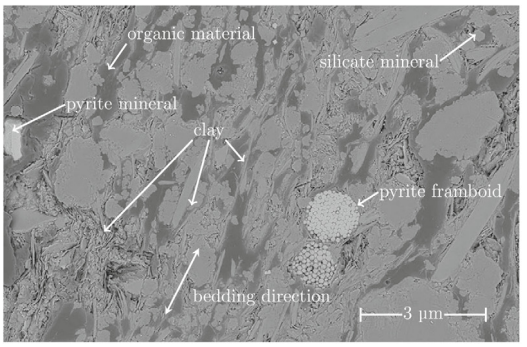

(a) Shale with organic and clay mixture identified as the matrix, characterized however by inorganic and dense organic inclusion, with matrix identification and from Bennett et al. [2015b].

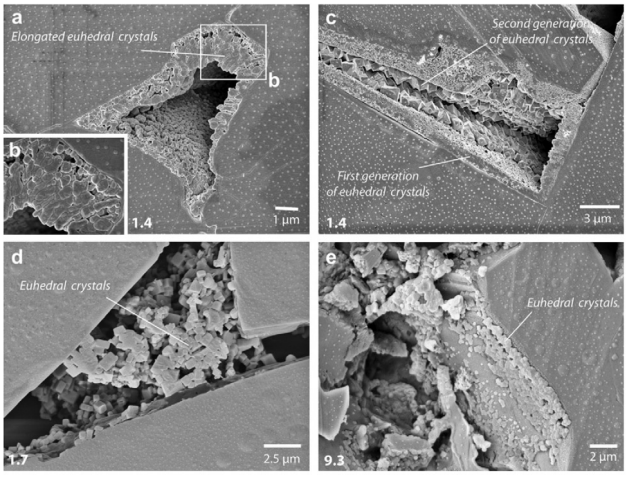

(b) Rock salt heterogeneity with spatial scale decreasing from (a) to (d), showing distribution of gas and brine inclusions at the course scale, compared to brine contained within pores at the fine scale, from Desbois et al. [2012]

Fig. 1. Rock material heterogeneity at the micrometer scale, showing two different materials of significant engineering interest, both characterized by size-dependence of the anisotropy.

of Helmholtz equations that regularize the plastic flow and circumvent pathological mesh dependence. Rather than directly introducing gradient term to the plastic flow, we introduce coupling energy functionals that penalize the difference between the local internal variables and the global projected internal variables updated by the Helmholtz equations. This treatment enables us to bypass the identification of the plastic zone and the projection of the local internal variables typically required for gradient plasticity models [13]. By leveraging the non-coaxiality of the local transversely isotropic plane and the diffusivity tensor in the Helmholtz equations, the new model is able to exhibit plastic flow of different direction than the stress gradient of the isotropically-regularized yield function, without introducing any plastic potential function, differently than the yield function or direction changes commonly employed in generalized plasticity models [14]. To the best of our knowledge, this work is the first micromorphically regularized Cam-clay model, and is designed to capture the size-dependent anisotropy in geological materials.

As pointed out in previous work such as Sun et al. [15], Sun et al. [16], Sun [17], Wang and Sun [18], Scovazzi et al. [19] and Wang and Sun [20], isochoric plastic flow occurring at the critical state may cause significant numerical challenges due to volumetric locking and potential low or zero energy modes sometimes attributed to the failure of geomaterials [18,21–23]. While the micromorphic regularization is already known to be an effective localization limiter, its effect on relaxing the volumetric locking has not yet been examined in detail. Our numerical examples have provided observations and numerical evidence to fill this knowledge gap. Finally, our numerical examples also indicate that the multiscale anisotropic model is capable of capturing the key morphological characteristic of the deformation band in anisotropic materials.

The organization of the rest of the paper is as follows. We first introduce the key elements of the anisotropic MCC model, including the usage of a mapping tensor for the local constitutive law and the gradient-based diffusive penalty stored work functional that provides a non-coaxial regularization for the post-bifurcation responses. Following this, the details of the implementation of the return mapping algorithm are discussed. Numerical examples are given and a brief summary of key results are presented in the conclusion.

As for notations and symbols, bold-faced letters denote tensors; the symbol '$\cdot$' denotes a single contraction of adjacent indices of two tensors (e.g., $\boldsymbol{a}\cdot\boldsymbol{b}=a_ib_i$ or $\boldsymbol{c}\cdot\boldsymbol{d}=c_{ij}d_{jk}$); the symbol ':' denotes a double contraction of adjacent indices of tensor of rank two or higher (e.g., $\boldsymbol{C}^{\mathrm{e}}:\boldsymbol{\epsilon}^{\boldsymbol{e}}=C^{\mathrm{e}}_{ijkl}\epsilon^{e}_{kl}$); the symbol '$\otimes$' denotes a juxtaposition of two vectors (e.g., $\boldsymbol{a}\otimes\boldsymbol{b}=a_ib_j$) or two symmetric second order tensors (e.g., $(\boldsymbol{\alpha}\otimes\boldsymbol{\beta})_{ijkl}=\alpha_{ij}\beta_{kl}$). Moreover, $(\boldsymbol{\alpha}\oplus\boldsymbol{\beta})_{ijkl}=\alpha_{jl}\beta_{ik}$ and $(\boldsymbol{\alpha}\ominus\boldsymbol{\beta})_{ijkl}=\alpha_{il}\beta_{jk}$. We also define identity tensors $(\mathbf{1})_{ij}=\delta_{ij}$ and $(\boldsymbol{I})_{ijkl}=(\delta_{ik}\delta_{jl}+\delta_{il}\delta_{kj})/2$, where δ_{ij} is the Kronecker delta.

2. Micromorphic anisotropic MCC model

In this section, we introduce the formulation of the micromorphic anisotropic MCC model capturing the size-dependent anisotropy of the plastic response. For simplicity, the anisotropically elastic response of the material is assumed to be linear. Then, we incorporate a non-coaxial anisotropic micromorphic regularization into the anisotropic MCC framework previously introduced in [24] and codified in [8]. While both the anisotropic mapping and the anisotropic regularization both lead to transversely isotropic responses, they influence the plastic deformation differently. Local anisotropy introduced through the map may provide the response of a homogenized effective medium. In contrast, the anisotropic regularization provides a mechanism that introduces size-dependent anisotropy, wherein the anisotropic response is sensitive to the physical length scale of the material for a given orientation. Since these two anisotropic mechanisms are not necessarily co-axial, incorporating both can provide more flexibility to capture of the material responses of the microstructure composed of fabric, platelet, and minerals that span multiple length scales. The following assumptions are made throughout this paper.

- The deformation remains infinitesimal such that the infinitesimal strain measure applies, i.e. $\boldsymbol{\epsilon} = (\nabla \boldsymbol{u} + \nabla \boldsymbol{u}^{\mathrm{T}})/2 = \nabla_s \boldsymbol{u}$, where $\boldsymbol{u}$ is the displacement field.
- The deformation process occurs while maintaining the isothermal condition such that the heat transfer can be neglected.
- The inertial force is negligible and hence the material is under a quasi-static condition.

In the geometrically linear regime, the additive strain decomposition of the infinitesimal elastic and plastic strains is valid, i.e.

$$\boldsymbol{\epsilon} = \boldsymbol{\epsilon}^{\mathrm{e}} + \boldsymbol{\epsilon}^{\mathrm{p}}, \tag{1}$$

where superscripting e and p designates elastic and plastic parts of the strain, respectively. The stored work is partitioned into the elastic strain energy and the stored plastic work, i.e.

$$W(\boldsymbol{\epsilon}^{\mathrm{e}}, \boldsymbol{\alpha}, \tilde{\boldsymbol{\alpha}}) = W^{\mathrm{e}}(\boldsymbol{\epsilon}^{\mathrm{e}}) + W^{\mathrm{p}}(\boldsymbol{\alpha}, \tilde{\boldsymbol{\alpha}}), \tag{2}$$

where $\boldsymbol{\alpha}$ is a collection of strain-like internal variables computed from the plastic strain $\boldsymbol{\epsilon}^{\mathrm{p}}$. In contrast, $\tilde{\boldsymbol{\alpha}}$ is a collection of field variables related to the internal variables by relaxation functionals in the stored plastic work W^{p} [25,26]. The total stored plastic work W^{p} is partitioned as

$$W^{\mathrm{p}}(\boldsymbol{\alpha}, \tilde{\boldsymbol{\alpha}}) = W^{\mathrm{p}}_{\boldsymbol{\alpha}}(\boldsymbol{\alpha}) + W^{\mathrm{p}}_{\tilde{\boldsymbol{\alpha}}}(\boldsymbol{\alpha}, \tilde{\boldsymbol{\alpha}}), \tag{3}$$

where $\boldsymbol{\alpha} = \{\lambda, \epsilon^{\mathrm{p}}_v\}$ is the set of history-dependent variables subjected to gradient regularization via a relaxation energy functional that penalizes the discrepancy of $\boldsymbol{\alpha}$ and the set of corresponding field variables constrained by the Helmholtz equation, i.e. $\tilde{\boldsymbol{\alpha}} = \{\tilde{\lambda}, \tilde{\epsilon}^{\mathrm{p}}_v\}$. In this work, we introduce regularization both on the plastic multiplier λ and on the volumetric plastic strain ϵ^{p}_v. This strategy is more complex, more costly and requires more elaborated calibration effects to identify material parameters than the alternative where only one internal variable is regularized in [25,26]. However, introducing the gradient regularization for both the plastic multiplier λ and the volumetric plastic strain ϵ^{p}_v also provides some benefits in capturing the critical state under which the plastic strain becomes isochoric [15,27–29]. In particular, the second Helmholtz equation for the regularized field variable $\tilde{\epsilon}^{\mathrm{p}}_v$ may penalize the sharp gradient of the local volumetric plastic strain by introducing a cost to generate such a sharp gradient. In principle, this technique can also be applied in an element-by-element manner through introducing an assumed strain formulation [23], reduced integration with hourglass control (e.g. [30]) or nonlocal averaging on a patch [31]. Preliminary studies presented in our numerical examples indicate that introducing the Helmholtz equation for the local volumetric plastic strain is sufficient to circumvent the volumetric locking with a more intuitive physical underpinning. Further analysis is certainly required to determine the optimal approach to capture the isochoric plastic flow at the critical state, but such an analysis is out of the scope of current study.

Note that this indirect approach enables the field variables within $\tilde{\boldsymbol{\alpha}}$ to be defined not just inside the plastic zone but on the entire body $\mathcal{B}$ with boundary $\partial\mathcal{B}$ as:

$$\tilde{\lambda} : \mathcal{B} \to \mathbb{R}^+ \cup \{0\} \mid \hat{\boldsymbol{n}} \cdot \boldsymbol{\omega}_\lambda \cdot \nabla \tilde{\lambda} = 0 \text{ on } \partial\mathcal{B}, \quad \tilde{\epsilon}^{\mathrm{p}}_v : \mathcal{B} \to \mathbb{R} \mid \hat{\boldsymbol{n}} \cdot \boldsymbol{\omega}_v \cdot \nabla \tilde{\epsilon}^{\mathrm{p}}_v = 0 \text{ on } \partial\mathcal{B}, \tag{4}$$

where $\hat{\boldsymbol{n}}$ is the boundary unit outward normal, and $\boldsymbol{\omega}_\lambda$ and $\boldsymbol{\omega}_v$ are second-order micromorphic diffusivity tensors. These tensors and the specific form of $W^{\mathrm{p}}_{\tilde{\boldsymbol{\alpha}}}(\boldsymbol{\alpha}, \tilde{\boldsymbol{\alpha}})$ are discussed in Section 2.3.

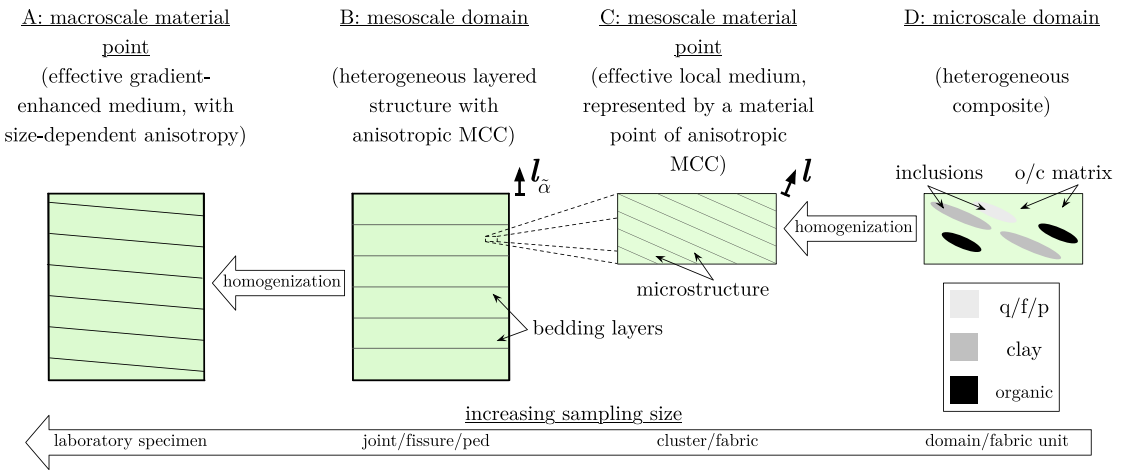

Fig. 2. Schematic of mesoscale and microscale-homogenized material effective media, where $\boldsymbol{l}$ is the microstructural direction whereas $\boldsymbol{l}_{\tilde{\alpha}}$ is the direction characterizing the anisotropic micromorphic regularization of a plastic internal variable α, via the projected internal variable $\tilde{\alpha}$, governed by energy functionals as detailed in Section 2.3, with inhomogeneous microscale identification and constituent categorization after [2]; q/f/p means inorganic quartz, feldspar, or pyrite, and o/c matrix indicates organic and clay matrix.

2.1. Anisotropic elasticity

We employ a linear elasticity model such that the strain energy and elastic strain are related via

$$W^{\mathrm{e}} = \frac{1}{2}\boldsymbol{\epsilon}^{\mathrm{e}} : \boldsymbol{C}^{\mathrm{e}} : \boldsymbol{\epsilon}^{\mathrm{e}}, \tag{5}$$

where $\boldsymbol{C}^{\mathrm{e}}$ is an super-symmetric fourth-order tensor expressing transverse isotropy of the elastic material response (for terminology cf. [32], and for discussion of related Kelvin-notated matrix equivalents exhibiting symmetry such at the solid elastic tangent, see Appendix A).

As such by Eq. (5), we discard in this work: nonlinearity of the material's elastic volumetric response, such that the pressure is semilogarithmic in the trace of the elastic strain during elastic unloading or rebounding; and, any potential coupling of the effective shear moduli to changes in the elastic bulk modulus with confining stress. In fact, elastic nonlinearity has previously been written in a strain energy functional amenable to a variational treatment, e.g. see Eq. (3.4-6) in [33], given that our model's local minimization is already over the elastic strain (per later Section 2.5).

To introduce anisotropy of the elastic response corresponding to the orientation of the isotropic plane's normal, this elastic stiffness tensor $\boldsymbol{C}^{\mathrm{e}}$ is expressed as a function of a second-order microstructural tensor, a dyadic tensor denoted as $\boldsymbol{\phi} = \boldsymbol{l} \otimes \boldsymbol{l}$, where the microstructural direction $\boldsymbol{l}$ is a unit vector normal to the plane of isotropy, for $\boldsymbol{l} \cdot \boldsymbol{l} = 1$. For instance, $\boldsymbol{l}$ would be approximately vertical for many in-situ shale rock layers. The transversely isotropic elastic stiffness tensor is then represented via direction $\boldsymbol{l}$ (cf. [34]):

$$\boldsymbol{C}^{\mathrm{e}} = c_1\boldsymbol{E}_1 + c_2\boldsymbol{E}_2 + c_3(\boldsymbol{E}_3 + \boldsymbol{E}_4) + c_5\boldsymbol{F} + c_6\boldsymbol{G}, \tag{6}$$

where c_1 through c_6 are elastic moduli and $\boldsymbol{E}_1$ through $\boldsymbol{G}$ are fourth-order tensors, related to the elastic input parameters, see Appendix B.

In this work, we introduce a gradient-dependent constitutive law for geomaterials (e.g. clay, mudstone, shales and salt) that may exhibit size-dependent anisotropy due to the complex microstructures. As shown in the example illustrated in Fig. 2, a macroscopic representative elementary volume (e.g. A in Fig. 2) may be formed by mesoscale layers that introduce anisotropy at the macroscopic scale (e.g. the homogenization from B to A in Fig. 2). However, the composite materials that form each layer may also contain microscopic fabrics or domain units (e.g. D in Fig. 2) that introduce a mesoscale anisotropy originating from the microscale composite (e.g. the homogenization from D to C in Fig. 2) but distinctive from those anisotropic effects introduced by the orientation of the homogenized layers (e.g. B in Fig. 2). As such, if we introduce a transversely isotropic effective medium at the scale comparable to the

mesoscale layers, then the Euler angles between the effective principal directions corresponding to the homogenized principal strain and stress tensors of the effective medium may vary when different sizes of the representative elementary volume are subjected to homogenization. This effect is referred as size-dependent anisotropy throughout this paper. To capture this size-dependent anisotropy, we therefore introduce an anisotropic regularization for a transversely isotropic local constitutive law and use the mismatches among the isotropy plane of the local constitutive law and the principal directions of the diffusivity tensors of the gradient terms to replicate the size-dependence of anisotropy across length scales.

2.2. Anisotropic local plasticity

This section describes the local contribution $W^{\mathrm{p}}_{\boldsymbol{\alpha}}$ of the total stored plastic work W^{p}, which is partitioned as $W^{\mathrm{p}}(\boldsymbol{\alpha},\tilde{\boldsymbol{\alpha}}) = W^{\mathrm{p}}_{\boldsymbol{\alpha}}(\boldsymbol{\alpha}) + W^{\mathrm{p}}_{\tilde{\boldsymbol{\alpha}}}(\boldsymbol{\alpha},\tilde{\boldsymbol{\alpha}})$. In particular, we will review the relation between the hardening law and the stored plastic work (cf. Section 2.2.1) and the flow rules introducing via the mapping technique (cf. Section 2.2.2).

2.2.1. Hardening law

The stored work of hardening W^{p}_{c} in the purely local stored plastic work $W^{\mathrm{p}}_{\boldsymbol{\alpha}}$ is computed using an exponential constitutive relation. This admits model parameters (e.g. C_d) resembling the expression of the classical hardening law for the isotropic MCC counterpart (cf. [27,35] and [36]),

$$p_c = p_{c\,0}\exp\left(\frac{\epsilon^{\mathrm{p}}_{v\,0} - \epsilon^{\mathrm{p}}_{v}}{C_d}\right), \quad \dot{\epsilon}^{\mathrm{p}}_{v} = \boldsymbol{b}_v : \dot{\boldsymbol{\epsilon}}^{\mathrm{p}}, \tag{7}$$

where $p_{c\,0} < 0$ is the reference pressure, and $C_d > 0$ is a material parameter related to the difference between the plastic and elastic compressibility of the materials. In the special case where (1) the bulk modulus of the material is $K = -p/C_r$ (which is not the case described in Section 2.1) and (2) the gradient regularization effect is vanished, then the bilogarithmic compressibility law $C_d = C_c - C_r$ introduced in [37] and [38] is recovered over a finite load increment. In other words, the parameter C_d can be obtained from a one-dimensional compression (oedometer) test. However, special caution must be paid to ensure that the plastic deformation of the specimen remains *homogeneous* (such that the Laplacian/diffusion terms of the Helmholtz equations vanish) along the normal compression line and the hysteresis loops.

Note that in this content, $\dot{\epsilon}^{\mathrm{p}}_{v} = \boldsymbol{b}_v : \dot{\boldsymbol{\epsilon}}^{\mathrm{p}}$ is not the increment of the volumetric plastic strain in the physical space but a strain measure in the fictitious space. Symmetric second-order tensor $\boldsymbol{b}_v$ is conventionally $\mathbf{1}$, such that $\epsilon^{\mathrm{p}}_{v}$ is the volumetric plastic strain. For our small-strain kinematic assumption, this implies to a semilogarithmic relation between $-p_c$ and ϵ_v during plastic deformation, cf. Eqs. (3.14-19) in [33]. Integrating p_c to find the stored work

$$W^{\mathrm{p}}_{c} - W^{\mathrm{p}}_{c\,0} = \int_{\epsilon^{\mathrm{p}}_{v\,0}}^{\epsilon^{\mathrm{p}}_{v}} p_c \mathrm{d}\epsilon^{\mathrm{p}'}_{v} = p_{c\,0} C_d \left[1 - \exp\left(\frac{\epsilon^{\mathrm{p}}_{v\,0} - \epsilon^{\mathrm{p}}_{v}}{C_d}\right)\right], \tag{8}$$

where subscripting 0 indicates the reference state. In our numerical examples, we consider the idealized case in which the preconsolidation pressure $p_{c\,0}$ is non-trivial but $\epsilon^{\mathrm{p}}_{v\,0} = 0$ and $p_{c\,0}$ as indicated in Appendix D. For applications in the field scale, a more elaborated calibration is needed to establish the equilibrium state at the beginning of the simulations, as the residual stress and the body force may lead to a deformed initial configuration [39].

2.2.2. Flow rule in mapped space

In our proposed constitutive framework, anisotropy of the responses originates from two sources, the anisotropy from the local constitutive law and the counterpart from anisotropic micromorphic regularization. As to the local plastic anisotropy, we employ an eigen-space mapping strategy. The key idea of this eigen-space mapping idea is to create a mapping in between the physical space and a fictitious isotropic space, such that anisotropic constitutive response in the physical space can be obtained by mapping an isotropic constitutive response obtained from an isotropic plasticity model to the physical space. This strategy has applied as a stress-space mapping in different isotropic yield functions to introduce anisotropy, such as Hashagen and de Borst [40] for the Hoffman yield function, Crook et al. [24] and Semnani et al. [8] for the MCC yield function, Versino and Bennett [41] for the Von Mises yield function and [12] for the Drucker–Prager yield function.

The upshot of this approach is that one may, in theory, create anisotropic constitutive laws from a template of isotropic constitutive law by introducing a linear and one-to-one mapping between the real configuration of the material and the fictitious isotropic configuration, by either stress-space or, as here, strain-space mapping tensors. The anisotropic plasticity mapping can be represented by a super-symmetric fourth-order tensor. This tensor is also built using $\boldsymbol{I}$ as, cf. [8]:

$$\boldsymbol{P}^{\mathrm{p}} = \beta \boldsymbol{P}_1^{\mathrm{p}} + (\alpha + \beta - 2\gamma)\, \boldsymbol{P}_2^{\mathrm{p}} + 2\,(\gamma - \beta)\, \boldsymbol{P}_3^{\mathrm{p}}, \tag{9}$$

where α, β, and γ are plastic anisotropy input parameters, and $\boldsymbol{P}_1^{\mathrm{p}}$ through $\boldsymbol{P}_3^{\mathrm{p}}$ are super-symmetric fourth-order tensors, see Appendix C. Input material parameters are selected such that $\boldsymbol{P}^{\mathrm{p}}$ is invertible and, on that note, $\boldsymbol{P}^{\mathrm{p}}(\alpha, \beta, \gamma) = \boldsymbol{I}$ for $\alpha = \beta = \gamma = 1$. Their plastic map defines the mean pressure and deviatoric stress in the mapped fictitious isotropic stress-space,

$$p^* = \boldsymbol{a}_p : \boldsymbol{\sigma}, \quad q^* = \sqrt{\frac{1}{2}\boldsymbol{\sigma} : \boldsymbol{A}_q : \boldsymbol{\sigma}}, \tag{10}$$

where

$$\boldsymbol{a}_p = \frac{1}{3}\boldsymbol{P}^{\mathrm{p\,vol}} : \boldsymbol{1}, \quad \boldsymbol{A}_q = 3\boldsymbol{P}^{\mathrm{p\,dev}} : \boldsymbol{P}^{\mathrm{dev}} : \boldsymbol{P}^{\mathrm{p\,dev}}, \quad \boldsymbol{P}^{\mathrm{dev}} = \boldsymbol{I} - \boldsymbol{P}^{\mathrm{vol}}, \quad \boldsymbol{P}^{\mathrm{vol}} = \frac{1}{3}\boldsymbol{1} \otimes \boldsymbol{1},$$

for distinct mappings $\boldsymbol{P}^{\mathrm{p\,dev}}(\alpha^{\mathrm{dev}}, \beta^{\mathrm{dev}}, \gamma^{\mathrm{dev}}) \neq \boldsymbol{P}^{\mathrm{p\,vol}}(\alpha^{\mathrm{vol}}, \beta^{\mathrm{vol}}, \gamma^{\mathrm{vol}})$. Superscripting 'dev' and 'vol' relates to independent deviatoric and volumetric maps, respectively. Absent superscript $*$, p and q are computed using $\boldsymbol{I}$ as the plastic mapping tensor. Fourth-order projection tensors $\boldsymbol{P}^{\mathrm{dev}}$ and $\boldsymbol{P}^{\mathrm{vol}}$ are idempotent and orthogonal, cf. [32] or Section 2.6 in [42].

Following the treatment in [43], we consider the plastic deformation obeys the same associative flow rule and that a variational structure exists such that the plastic flow rule is the primitive postulate of the theory, and latterly the elastic domain-describing yield criterion is the derived rule, also cf. [44]. While [43] has demonstrated that such a framework is convenient for extending the isotropic MCC model into the finite deformation regime and enforcing material-frame indifference, our derivation in the subsequent sections indicates that this variational framework also simplify the extension of the anisotropic MCC model to incorporate a gradient-dependent flow rule. For the local anisotropic MCC plasticity, the flow rule is

$$\dot{\boldsymbol{\epsilon}}^{\mathrm{p}} = \dot{\lambda}\boldsymbol{n} \mid \dot{\lambda} \geq 0, \tag{11}$$

where the local equivalent plastic strain's rate $\dot{\lambda}$ is non-negative, $\boldsymbol{n}$ the second-order tensorial direction of plastic flow is not traceless, and $(\dot{\cdot})$ indicates the time derivative of $(\cdot)$. If yielding, plastic strain direction $\boldsymbol{n}$ satisfies the kinematic constraint

$$\boldsymbol{n} : \boldsymbol{B}_\lambda : \boldsymbol{n} = 1, \quad \boldsymbol{B}_\lambda = \frac{3}{M^2}\boldsymbol{P}^{\mathrm{p\,vol}\,-1} : \boldsymbol{P}^{\mathrm{vol}} : \boldsymbol{P}^{\mathrm{p\,vol}\,-1} + \frac{2}{3}\boldsymbol{P}^{\mathrm{p\,dev}\,-1} : \boldsymbol{P}^{\mathrm{dev}} : \boldsymbol{P}^{\mathrm{p\,dev}\,-1}, \tag{12}$$

where $M > 0$ is a dimensionless physical constant, later shown to be the slope of the critical state line, in Sections 2.5.1 and 2.5.2. Our convention is that the symmetric fourth-order tensor $\boldsymbol{A}_{(\cdot)}$ maps stress $\boldsymbol{\sigma}$ from the real stress to fictitious isotropic stress-space, whereas $\boldsymbol{B}_{(\cdot)}$ maps kinematics-related tensorial internal variables, which convention is intended to be in-line with the general quadratic model for plasticity presented in Section 2.5.1 of Simo and Hughes [45].

The rate $\dot{\lambda}$ is positive for change in the local equivalent plastic strain,

$$\dot{\lambda} = \sqrt{\dot{\boldsymbol{\epsilon}}^{\mathrm{p}} : \boldsymbol{B}_\lambda : \dot{\boldsymbol{\epsilon}}^{\mathrm{p}}} \geq 0.$$

Note that $\dot{\lambda}$ is degree one homogeneous in $\dot{\boldsymbol{\epsilon}}^{\mathrm{p}}$, because $(\partial\dot{\lambda}/\partial\dot{\boldsymbol{\epsilon}}^{\mathrm{p}}) : \dot{\boldsymbol{\epsilon}}^{\mathrm{p}} = \dot{\lambda}$. Furthermore, $\dot{\lambda} \in \mathbb{R}$ as $\dot{\boldsymbol{\epsilon}}^{\mathrm{p}} : \boldsymbol{B}_\lambda : \dot{\boldsymbol{\epsilon}}^{\mathrm{p}} \geq 0$ for all $\dot{\boldsymbol{\epsilon}}^{\mathrm{p}}$.

2.3. Anisotropic plastic regularization for non-coaxial plastic flow

The energy functional W^{p} in Eq. (3) contains two types of energy functionals, i.e. [25,26],

$$W^{\mathrm{p}}_{\tilde{\boldsymbol{\alpha}}}(\boldsymbol{\alpha}, \tilde{\boldsymbol{\alpha}}) = \overbrace{\frac{k_\lambda}{2}\left(\tilde{\lambda} - \lambda\right)^2 + \frac{k_v}{2}\left(\tilde{\epsilon}_v^{\mathrm{p}} - \epsilon_v^{\mathrm{p}}\right)^2}^{\text{penalty functionals}} + \overbrace{\frac{K_\lambda l_\lambda^2}{2}\nabla\tilde{\lambda}\cdot\boldsymbol{\omega}_\lambda\cdot\nabla\tilde{\lambda} + \frac{K_v l_v^2}{2}\nabla\tilde{\epsilon}_v^{\mathrm{p}}\cdot\boldsymbol{\omega}_v\cdot\nabla\tilde{\epsilon}_v^{\mathrm{p}}}^{\text{anisotropic regularization functionals}}, \tag{13}$$

where $\boldsymbol{\alpha} = \{\lambda, \epsilon_v^p\}$ and $\tilde{\boldsymbol{\alpha}} = \{\tilde{\lambda}, \tilde{\epsilon}_v^p\}$, k_λ and k_v are stiffness parameters, and penalize difference between local internal variables and field values of $\tilde{\lambda}$ and $\tilde{\epsilon}_v^{\mathrm{p}}$. $K_\lambda > 0$ and $K_v > 0$ are moduli which have the same unit as a stiffness, and $l_\lambda > 0$ and $l_v > 0$ are length scale parameters corresponding to the regularized variables $\tilde{\lambda}$ and $\tilde{\epsilon}_v^{\mathrm{p}}$ respectively.

The first type of energy functionals are the relaxation functionals that penalize the difference between local internal variables and field variables measured by the L_2 norm. The second type of energy functionals are weighted inner products of the gradient of the corresponding field variables that introduce the gradient dependence and the non-coaxiality of the plastic flow. The Euler–Lagrange equation of these two types of energy functional leads to two modified Helmholtz equations of which the corresponding Galerkin form is solved via the finite element method in this work. Notice that the second-order positive-definite diffusivity tensors $\boldsymbol{\omega}_\lambda$ and $\boldsymbol{\omega}_v$, are weighting functions in the weighted inner product. They are used to introduce anisotropy on the gradient-dependence of the field variables $\tilde{\lambda}$ and $\tilde{\epsilon}_v^p$. Since both $\boldsymbol{\omega}_\lambda$ and $\boldsymbol{\omega}_v$ are not isotropic tensors, a bias is therefore introduced in the regularization such that the gradient dependencies are stronger in the principal directions corresponding to the largest eigenvalues of $\boldsymbol{\omega}_\lambda$ and $\boldsymbol{\omega}_v$ than those corresponding to smaller eigenvalues. In other words, the plastic flow direction of each material point is therefore not only depending on the stress gradient of the yield function at the material point but also depends on the directionally biased influence of the neighbors characterized by $\boldsymbol{\omega}_\lambda$ and $\boldsymbol{\omega}_v$. Consequently, the resultant gradient-enhanced plasticity model is associative, but the plastic flow direction is not necessarily coaxial to the stress gradient of the conventional MCC yield function due to the anisotropic regularization.

Note that the anisotropy introduced by the anisotropic diffusivity tensors $\boldsymbol{\omega}_\lambda$ and $\boldsymbol{\omega}_v$ is of different nature than those introduced at the local constitutive laws. In particular, the anisotropic effect introduced via the anisotropic diffusivity tensors exhibits scale effects. Furthermore, since the principal directions of the anisotropic diffusivity tensors are independent of the mapping operators used to introduce anisotropy into the local constitutive law, the Euler angles between the isotropic plane of the local plasticity model and the principal directions of tensors $\boldsymbol{\omega}_\lambda$ and $\boldsymbol{\omega}_v$ can be leveraged to generate a fuller anisotropic constitutive responses for complex materials for which the anisotropic responses are originated from multiple geometrical attributes across length scales (e.g. joints, layers, fabrics, slip systems, lattice).

Remark 1. To simplify the material identification procedure, analogously to the parameter selection in [46] or [47], we associate the volumetric term with the volumetric stiffness constant,

$$K_\lambda \sim a_\lambda = a_v, \quad K_v \sim a_v = \frac{1}{3}\mathbf{1} : \boldsymbol{C}^{\mathrm{e}} : \mathbf{1}, \tag{14}$$

where our notation appropriates that of Walpole [34]. Within the Walpole notation for elastic isotropy, $a = \mathbf{1} : \boldsymbol{C}^{\mathrm{e}} : \mathbf{1}/3$, where the bulk modulus $K = a/3$. Calibration of the regularization might alternatively includes inverse problems, against strain gradients obtained from triaxial tests [48]. That said, our 2D and 3D numerical examples consistently converge through strain softening.

Note that, for a given set of fixed length scale parameters, l_λ and l_v, the discrepancy between the local and the projected internal variables, and the spatial distribution of the projected internal variables are affected by the ratios K_λ/k_λ and K_v/k_v. If these ratios are low, then the discrepancy between the local and the field variables is lower but the field variables may exhibit sharper spatial gradients. If these ratios are high, then the sharp gradient of the projected internal variables may not be admissible, but the discrepancy between the local and field variables could be larger.

Now consider the tensor $\boldsymbol{\omega}_\lambda$ (or $\boldsymbol{\omega}_v$) that describes microstructural attributes aligned with the unit vector $\boldsymbol{l}_\lambda$ for $\boldsymbol{l}_\lambda \cdot \boldsymbol{l}_\lambda = 1$.

Hence, one may express the tensor $\boldsymbol{\omega}_\lambda$ as a function of the tensors $\boldsymbol{\phi}_\lambda = \boldsymbol{l}_\lambda \otimes \boldsymbol{l}_\lambda$ and $\boldsymbol{\chi}_\lambda = \mathbf{1} - \boldsymbol{l}_\lambda \otimes \boldsymbol{l}_\lambda$. Due to the orthogonality and idempotence of $\boldsymbol{\phi}_\lambda$ and $\boldsymbol{\chi}_\lambda$, in the combined formalism of Clayton and Knap [49], Teichtmeister et al. [50], and Bryant and Sun [51], the definition of this mapping relates

$$\boldsymbol{\omega}_\lambda = (\boldsymbol{p}_\lambda \otimes \boldsymbol{p}_\lambda) : \mathbf{1} = \mathbf{1} + \phi_\lambda \boldsymbol{\phi}_\lambda + \chi_\lambda \boldsymbol{\chi}_\lambda, \quad \boldsymbol{p}_\lambda = \boldsymbol{\phi}_\lambda \sqrt{1 + \phi_\lambda} + \boldsymbol{\chi}_\lambda \sqrt{1 + \chi_\lambda}, \tag{15}$$

where coefficients ϕ_λ and χ_λ are dimensionless, as is tensor $\boldsymbol{\omega}_\lambda$. Coefficients $\phi_\lambda \geq -1$ and $\chi_\lambda \geq -1$, such that $\boldsymbol{\omega}_\lambda$ is positive semidefinite. Physically, $\phi_\lambda \gg 0$ penalizes field variable diffusion on planes normal to $\boldsymbol{l}_\lambda$, whereas $\chi_\lambda \gg 0$ penalizes damage diffusion on planes not normal to normal vector $\boldsymbol{l}_\lambda$. For $\phi_\lambda = \chi_\lambda = 0$, $\boldsymbol{p}_\lambda = \mathbf{1}$ such that the mapping reduces to isotropy. $\phi_\lambda \neq \chi_\lambda$ indicates $\boldsymbol{\omega}_\lambda$ is a tensor with one unique and one repeated eigenvalue. These statements apply equally to $\boldsymbol{\omega}_v$.

2.4. Incremental stored plastic work

Our objective is to an incremental form of the stored work functionals, such that the incremental constitutive update can be associated with the Euler–Lagrange equation of a discrete functional (see next section). In particular, we employ a backward-implicit Euler method to integrate plastic work. Consider a finite set consisting of discrete snapshots of time instants $\{t_0, \ldots, t_n, t_{n+1}\}$, for n the time step, with the data at prior time $t_1, t_2, \ldots, t_n$ given. At the new time t_{n+1}, the elastoplastic strain terms are

$$\boldsymbol{\epsilon}_{n+1} = \boldsymbol{\epsilon}^{\mathrm{e}}_{n+1} + \boldsymbol{\epsilon}^{\mathrm{p}}_{n+1}, \quad (\cdot)_{n+1} = (\cdot)_n + \Delta(\cdot)\big|_n^{n+1}. \tag{16}$$

The local stored plastic work has been defined in the mapped-isotropic strain-space by Ortiz and Pandolfi [43], as

$$W^{\mathrm{p}}_{\boldsymbol{\alpha}\, n+1} - W^{\mathrm{p}}_{\boldsymbol{\alpha}\, n} = \underbrace{\frac{1}{2}\left[W^{\mathrm{p}}_c(\epsilon^{\mathrm{p}}_{v\, n+1}) - W^{\mathrm{p}}_c(\epsilon^{\mathrm{p}}_{v\, n})\right] - \frac{M}{2}\overbrace{(\lambda_{n+1} - \lambda_n)\left[\partial_{\epsilon^{\mathrm{p}}_v} W^{\mathrm{p}}_c(\epsilon^{\mathrm{p}}_{v\, n+1})\right]}^{\text{ensure } p_{c\, n+1} \le 0}}_{\text{matched coefficients } 1/2 \text{ and } M/2 \text{ return MCC yield criterion}}. \tag{17}$$

Note the Lagrange multiplier term $M(\lambda_{n+1} - \lambda_n)p_{c\, n+1}/2 = -\Delta\lambda\sigma_{q\, n+1}$ enforces non-positivity of the preconsolidation pressure $p_{c\, n+1}$. The limits of the partial derivatives

$$\frac{\partial W^{\mathrm{p}}_{\boldsymbol{\alpha}\, n+1}}{\partial \Delta\lambda} = \frac{M}{2}\partial_{\epsilon^{\mathrm{p}}_v} W^{\mathrm{p}}_{c\, n+1} = \sigma_{q\, n+1}, \quad \frac{\partial W^{\mathrm{p}}_{\boldsymbol{\alpha}\, n+1}}{\partial \epsilon^{\mathrm{p}}_{v\, n+1}} = \frac{1}{2}\partial_{\epsilon^{\mathrm{p}}_v} W^{\mathrm{p}}_{c\, n+1} - \frac{M}{2}\Delta\lambda\partial^2_{\epsilon^{\mathrm{p}}_v \epsilon^{\mathrm{p}}_v} W^{\mathrm{p}}_{c\, n+1} = \sigma_{p\, n+1}, \tag{18}$$

are

$$\lim_{\Delta\lambda\to 0}\sigma_{q\, n+1} = \lim_{\Delta\lambda\to 0}\left(\frac{\partial W^{\mathrm{p}}_{\boldsymbol{\alpha}\, n+1}}{\partial\Delta\lambda}\right) = -\frac{M}{2}p_{c\, n+1}, \quad \lim_{\Delta\lambda\to 0}\sigma_{p\, n+1} = \lim_{\Delta\lambda\to 0}\left(\frac{\partial W^{\mathrm{p}}_{\boldsymbol{\alpha}\, n+1}}{\partial \epsilon^{\mathrm{p}}_{v\, n+1}}\right) = \frac{1}{2}p_{c\, n+1}. \tag{19}$$

These results are later used to estimate the connection between the two-invariant yield surface and the incremental energy functional, following the treatments in [52] and [43] in Section 2.5.2.

Remark 2. Albeit not considered in this study, anisotropy-adapted viscoplastic regularization is similarly intuitive. One possible way to incorporate viscoplasticity in a variational framework is via appending to the local stored incremental plastic work a term similar to,

$$\frac{\eta_\lambda}{2\Delta t}\left(\lambda_{n+1} - \lambda_n\right)^2 + \frac{\eta_v}{2\Delta t}\left(\epsilon^{\mathrm{p}}_{v\, n+1} - \epsilon^{\mathrm{p}}_{v\, n}\right)^2,$$

where η_λ and η_v are material parameters and $\Delta t = t_{n+1} - t_n$ is the time increment (cf. [52] and [43]).

2.5. Variational constitutive update with anisotropic micromorphic regularization

We derive an discrete energy functional whose Euler–Lagrange equation leads to the governing equation of the local constitutive law and the Helmholtz equations that regularize the boundary value problem. Meanwhile Following Eq. (3.3-13) in [53] e.g., we suppose the mechanical equilibrium equation's numerical solution is staggered w.r.t. solution of the regularizing Helmholtz equations. This staggering is in-line with solution of the mechanically-coupled scalar diffusion equations in [54], for instance.

Furthermore, we employ the variational principle to obtain the Helmholtz equations for $\tilde{\lambda}$ and $\tilde{\epsilon}^{\mathrm{p}}_v$ from the corresponding energy functional. Following the variational update for regularized viscoplastic models (e.g. [47]), the local constitutive update and the corresponding equations that govern the micromorphic regularization can be obtained from one discrete incremental energy functional. From this single incremental energy functional, we may derive the discrete Euler–Lagrange equation, a system of nonlinear equations that constitute both the local constitutive update and the micromorphic field equations [26].

This system of equations is solved via an operator-split scheme. The local constitutive updates are solved in a semi-implicit manner, in the sense that the incremental constitutive laws that updates the local internal variables and the stress are updated via a Newton solver while the incremental solutions of the Helmholtz equations are fixed. Meanwhile, when the incremental solutions of the Helmholtz equations are updated, the internal variables

are frozen. Further discussions about the operator-split scheme can be found in [17,26,55–58]. In this work, the Cauchy stress is integrated incrementally via a return mapping algorithm. As result, we have,

$$\boldsymbol{\epsilon}^{\mathrm{e}}_{n+1} = \boldsymbol{\epsilon}^{\mathrm{e\,tr}}_{n+1} - \Delta\boldsymbol{\epsilon}^{\mathrm{p}}, \quad \boldsymbol{\epsilon}^{\mathrm{e\,tr}}_{n+1} = \boldsymbol{\epsilon}_{n+1} - \boldsymbol{\epsilon}^{\mathrm{p}}_{n}, \tag{20}$$

where $\boldsymbol{\epsilon}^{\mathrm{e\,tr}}_{n+1}$ is the trial elastic strain. The strain and hence elastic trial strain are fixed while solving the local optimization problem, as we employ a standard return mapping algorithm. Thus

$$\frac{\partial \boldsymbol{\epsilon}^{\mathrm{p}}_{n+1}}{\partial \Delta\boldsymbol{\epsilon}^{\mathrm{p}}} = -\left.\frac{\partial \boldsymbol{\epsilon}^{\mathrm{e}}_{n+1}}{\partial \Delta\boldsymbol{\epsilon}^{\mathrm{p}}}\right|_{\boldsymbol{\epsilon}^{\mathrm{e\,tr}}_{n+1}} = \boldsymbol{I}, \quad \left.\frac{\partial \boldsymbol{\epsilon}_{n+1}}{\partial \Delta\boldsymbol{\epsilon}^{\mathrm{p}}}\right|_{\Delta\boldsymbol{\epsilon}} = \boldsymbol{0},$$

during the constitutive update, the algorithm by which we obtain $\boldsymbol{\sigma}_{n+1} = \boldsymbol{C}^{\mathrm{e}} : \boldsymbol{\epsilon}^{\mathrm{e}}_{n+1}$. Then, the identity $\boldsymbol{\epsilon}^{\mathrm{e}}_{n+1}$ in Eq. (20) defines the local minimization problem in the elastic strains. This implies the generalized coordinates

$$\boldsymbol{\zeta}_{n+1} = \{\boldsymbol{\epsilon}^{\mathrm{e}}_{n+1}, \tilde{\lambda}_{n+1}, \tilde{\epsilon}^{\mathrm{p}}_{v\,n+1}\}, \tag{21}$$

where Eq. (13) is used. For a given strain at an incremental step $\boldsymbol{\epsilon}_{n+1}$, the constitutive updates is associated with the Euler–Lagrange equation of the constrained optimization problem which reads,

$$\boldsymbol{\zeta}_{n+1} = \arg\min_{\boldsymbol{\zeta}_{n+1}} W(\boldsymbol{\zeta}_{n+1}). \tag{22}$$

subjected to the following constraint,

$$\Delta\lambda = \sqrt{\Delta\boldsymbol{\epsilon}^{\mathrm{p}}_{n+1} : \boldsymbol{B}_{\lambda} : \Delta\boldsymbol{\epsilon}^{\mathrm{p}}_{n+1}} \geq 0, \quad \Delta\epsilon^{\mathrm{p}}_{v\,n+1} = \boldsymbol{b}_{v} : \Delta\boldsymbol{\epsilon}^{\mathrm{p}}_{n+1}. \tag{23}$$

Note that the inequality in (23) is satisfied if $\boldsymbol{B}_{\lambda}$ is positive semi-definite (or positive definite). The micromorphic field equation that governs the relations between the global and local internal variables are obtained from the stationary conditions of Eq. (22) with respect to the global internal variables $\tilde{\lambda}_{n+1}$ and $\tilde{\epsilon}^{\mathrm{p}}_{v\,n+1}$, i.e.,

$$\frac{\delta W(\boldsymbol{\zeta}_{n+1})}{\delta \tilde{\lambda}_{n+1}} = k_{\lambda}(\tilde{\lambda}_{n+1} - \lambda_{n+1}) - K_{\lambda} l_{\lambda}^{2} \nabla \cdot (\boldsymbol{\omega}_{\lambda} \cdot \nabla \tilde{\lambda}_{n+1}) = 0, \ \text{in } \mathcal{B}, \tag{24}$$

$$\frac{\delta W(\boldsymbol{\zeta}_{n+1})}{\delta \tilde{\epsilon}^{\mathrm{p}}_{v\,n+1}} = k_{v}(\tilde{\epsilon}^{\mathrm{p}}_{v\,n+1} - \epsilon^{\mathrm{p}}_{v\,n+1}) - K_{v} l_{v}^{2} \nabla \cdot (\boldsymbol{\omega}_{v} \cdot \nabla \tilde{\epsilon}^{\mathrm{p}}_{v\,n+1}) = 0, \ \text{in } \mathcal{B}, \tag{25}$$

where the trivial boundary conditions, e.g. $\hat{\boldsymbol{n}} \cdot \boldsymbol{\omega}_{\lambda} \cdot \nabla \tilde{\lambda}_{n+1} = 0$ on $\partial\mathcal{B}$, are applied. On the other hand, the system of equations for the local constitutive updates can be obtained incrementally from the first variation of $W(\boldsymbol{\zeta}_{n+1})$ with respect to the elastic strain $\boldsymbol{\epsilon}^{\mathrm{e}}_{n+1}$ (see Appendix C.1 for the detailed derivation), i.e.,

$$\begin{aligned}\frac{\delta W(\boldsymbol{\zeta}_{n+1})}{\delta \boldsymbol{\epsilon}^{\mathrm{e}}_{n+1}} = {} & \overbrace{\boldsymbol{\sigma}_{n+1} - \sigma_{q\,n+1}\frac{\partial \Delta\lambda}{\partial \Delta\boldsymbol{\epsilon}^{\mathrm{p}}} - \sigma_{p\,n+1}\boldsymbol{b}_{v}}^{\text{purely local terms}} \\ & + \overbrace{k_{\lambda}\left(\tilde{\lambda}_{n+1} - \lambda_{n+1}\right)\frac{\partial \Delta\lambda}{\partial \Delta\boldsymbol{\epsilon}^{\mathrm{p}}} + k_{v}\left(\tilde{\epsilon}^{\mathrm{p}}_{v\,n+1} - \epsilon^{\mathrm{p}}_{v\,n+1}\right)\boldsymbol{b}_{v}}^{\text{micromorphic terms}} = \boldsymbol{0},\end{aligned} \tag{26}$$

where we used the definitions of $\boldsymbol{\sigma}_{n+1}$, $\partial W^{\mathrm{p}}_{\boldsymbol{\alpha}\,n+1}/\partial\Delta\lambda$, and $\partial W^{\mathrm{p}}_{\boldsymbol{\alpha}\,n+1}/\partial\epsilon^{\mathrm{p}}_{v\,n+1}$.

Remark 3. Direct substitution of law Eq. (7) curtails hardening force-related expressions otherwise proliferating in local-to-global variational updates, cf. e.g. [47]. Similarly per Section 2.4, viscoplasticity incorporates by a quadratic function of the plastic strain increment. Thus the regularized constitute update devolves to minimization Eq. (22).

2.5.1. Yield criterion

In the Euler–Lagrange equation. (26), we substitute $\partial\Delta\lambda/\partial\Delta\boldsymbol{\epsilon}^{\mathrm{p}} = \boldsymbol{B}_{\lambda} : \boldsymbol{n}_{n+1}$ such that

$$\boldsymbol{0} = \boldsymbol{\sigma}_{n+1} - \sigma_{q\,n+1}\boldsymbol{B}_{\lambda} : \boldsymbol{n}_{n+1} - \sigma_{p\,n+1}\boldsymbol{b}_{v} + k_{\lambda}\left(\tilde{\lambda}_{n+1} - \lambda_{n+1}\right)\boldsymbol{B}_{\lambda} : \boldsymbol{n}_{n+1} + k_{v}\left(\tilde{\epsilon}^{\mathrm{p}}_{v\,n+1} - \epsilon^{\mathrm{p}}_{v\,n+1}\right)\boldsymbol{b}_{v}. \tag{27}$$

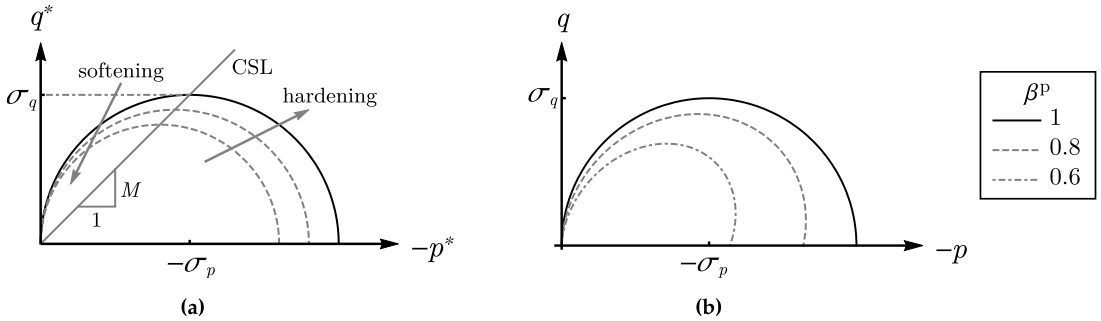

Fig. 3. Geometric interpretation of the mapped two-invariant yield criterion, Eq. (30): (a) introducing M as the slope of the critical state line (CSL) in the starred scalar space, after [43], and with softening and hardening trends after [36]; and, (b) unmapped two-invariant yield criterion parameterized by the mapping coefficient, varying $\beta^{\mathrm{dev}} = \beta^{\mathrm{vol}}$ at fixed $\alpha^{\mathrm{dev}} = \alpha^{\mathrm{vol}} = \gamma^{\mathrm{dev}} = \gamma^{\mathrm{vol}} = 1$, after [8].

Interiority within the elastic domain can be determined by rearranging the Euler–Lagrange equation to solve for $\boldsymbol{n}_{n+1}$. At the trail state $\boldsymbol{\epsilon}^{\mathrm{e}}_{n+1} = \boldsymbol{\epsilon}^{\mathrm{e\,tr}}_{n+1}$, the tensorial flow direction evaluates as

$$\boldsymbol{n}^{\mathrm{tr}}_{n+1} = \frac{1}{\sigma^{\mathrm{tr}}_{q\,n+1} - k_\lambda\left(\tilde{\lambda}_{n+1} - \lambda^{\mathrm{tr}}_{n+1}\right)} \boldsymbol{B}^{-1}_{\lambda} : \left[\boldsymbol{\sigma}^{\mathrm{tr}}_{n+1} - \sigma^{\mathrm{tr}}_{p\,n+1}\boldsymbol{b}_v + k_v\left(\tilde{\epsilon}^{\mathrm{p}}_{v\,n+1} - \epsilon^{\mathrm{p\,tr}}_{v\,n+1}\right)\boldsymbol{b}_v\right]. \tag{28}$$

If the stress is within the elastic domain, and given the kinematic constraint on the tensorial direction in Eq. (12), the yield criterion can be written as

$$\varphi(\boldsymbol{n}^{\mathrm{tr}}_{n+1}) = \boldsymbol{n}^{\mathrm{tr}}_{n+1} : \boldsymbol{B}_\lambda : \boldsymbol{n}^{\mathrm{tr}}_{n+1} - 1 \leq 0, \tag{29}$$

expressed quadratically in $\boldsymbol{n}^{\mathrm{tr}}_{n+1}$ to recover the yield criterion in quadratic terms of the mapped stress invariants (next section). Note that Eqs. (27), (28), and (29) combine to completely describe the variational update applied in Section 4.1. Followingly, change in the field variables $\tilde{\lambda}$ and $\tilde{\epsilon}^{\mathrm{p}}_v$ not just regularizes but can also trigger the onset of local yielding.

2.5.2. *Mapped two-invariant yield criterion*

Now we establish the connection between our derivation based on the variational principle and the formulation in [8]. The superscript tr is dropped for brevity. First, assume that $\boldsymbol{b}_v = \boldsymbol{P}^{\mathrm{p\,vol}\,-1} : \boldsymbol{1}$. Then, we eliminate the gradient dependence of the plastic flow by setting $k_\lambda = k_v = 0$. By substituting the definition of $\boldsymbol{n}_{n+1}$ in (28) into the yield function and simplifying the expression, we obtain,

$$\frac{\sigma^2_{q\,n+1}}{M^2}\varphi_{n+1} = \left(p^*_{n+1} - \sigma_{p\,n+1}\right)^2 + \frac{1}{M^2}\left(q^{*\,2}_{n+1} - \sigma^2_{q\,n+1}\right) \leq 0. \tag{30}$$

Applying the relations in Eq. (19), Eq. (30) can be rewritten as,

$$\boxed{\lim_{\Delta\lambda\to 0}\left(\frac{\sigma^2_{q\,n+1}}{M^2}\varphi_{n+1}\right) = p^*_{n+1}\left(p^*_{n+1} - p_{c\,n+1}\right) + \frac{q^{*\,2}_{n+1}}{M^2} \leq 0,} \tag{31}$$

at time step t_{n+1}, i.e. a necessary condition for the stress to be admissible. As a result, our model may be reduced to the anisotropic yield function in [8] when the gradient regularization vanishes. It can also be reduced to the classical modified Cam-clay model (cf. Eq. (6.18) in [36] when the mapping becomes identity) (see Fig. 3).

3. Balance and evolution equations

We solve the balance of linear equilibrium equation, i.e.

$$\nabla \cdot \boldsymbol{\sigma} + \rho\boldsymbol{g} = \boldsymbol{0}, \tag{32}$$

where $\boldsymbol{\sigma}$ is the Cauchy stress, ρ the density, and $\boldsymbol{g}$ the gravitational acceleration vector. We employ a hyperelastic energy functional such that the stress $\boldsymbol{\sigma} = \partial W^{\mathrm{e}}/\partial\boldsymbol{\epsilon}^{\mathrm{e}}$. Hence, the local internal variables λ and ϵ^{p}_v are updated

incrementally once the solution of the nonlinear static equilibrium equation is obtained via an implicit solver, with the same local-to-global hierarchy described in [44], regarding the variational constitutive update.

However, to introduce nonlocality in the constitutive law, we supply an additional set of governing equations to evolve the field variables $\tilde{\lambda}$ and $\tilde{\epsilon}_v^{\mathrm{p}}$. Both evolution equations are characterized variationally via introduction of diffusive functionals in Eq. (13), which depends on the spatial gradients of $\tilde{\lambda}$ and $\tilde{\epsilon}_v^{\mathrm{p}}$. In practice, we solve an equivalent nondimensionalized system (cf. [25]) with Laplacian coefficients of the regularization equation

$$\tilde{l}_\lambda = l_\lambda \sqrt{K_\lambda / k_\lambda}, \quad \tilde{l}_v = l_v \sqrt{K_v / k_v}. \tag{33}$$

Thus, each field variable accords with some Helmholtz equation, e.g.

$$\tilde{\alpha} - \tilde{l}^2 \nabla \cdot (\boldsymbol{\omega} \cdot \nabla \tilde{\alpha}) = \alpha, \tag{34}$$

for $\tilde{\alpha}$ a field variable, α the corresponding internal variable, $\tilde{l}$ a length, and $\boldsymbol{\omega}$ a dimensionless second-order tensor. The only imposed boundary condition for the Helmholtz equations is the trivial Neumann boundary condition.

This technique is referred to as micromorphic regularization in [25] and [46]. The nondimensionalizations $\sqrt{K_\lambda / k_\lambda}$ and $\sqrt{K_v / k_v}$ help us to explain convergence towards mesh independence even during material softening. See the results section, and for explanatory analysis [47].

4. Local–global constitutive updates

Due to the introduction of the micromorphic regularization, the constitutive update is obtained from a global–local split algorithm, such that the global evolution equations update the strain and the micromorphic field variables, while the local return mapping algorithm provides the incremental updates of the elastic (and equivalently the plastic) strain, internal variables, and plastic flow direction [47]. The governing equations for the micromorphic regularization are obtained from the stationary condition of the energy functional listed in Eq. (22). The elastic strain $\boldsymbol{\epsilon}_{n+1}^{\mathrm{e}}$ is defined from the strain update in Eq. (20), and results from optimality of the local minimization problem.

4.1. Local system

The local incremental stress update is obtained by a conventional return mapping algorithm. For clarity, the algorithm is summarized in Alg. 1. As necessary, we map or reconstruct required symmetric tensors from their Kelvin-notated vector equivalents per Eq. (44), and super-symmetric fourth-order tensors per. Eq. (45), Appendix A.

Algorithm 1 Local return-mapping

Require: From the global system, the strain increment $\Delta\boldsymbol{\epsilon}$ as well as, for the micromorphic regularization, field variables $\tilde{\lambda}$ and $\tilde{\epsilon}_v^{\mathrm{p}}$

1: A trial state is established
   a. set $\boldsymbol{\epsilon}_{n+1}^{\mathrm{e\ tr}} = \boldsymbol{\epsilon}_{n+1}^{\mathrm{e}} + \Delta\boldsymbol{\epsilon}$, $\lambda_{n+1}^{\mathrm{tr}} = \lambda_n$, $\epsilon_{v\ n+1}^{\mathrm{p\ tr}} = \epsilon_{v\ n}^{\mathrm{p}}$, $\sigma_{q\ n+1}^{\mathrm{tr}} = \sigma_{0\ n}$, and $\sigma_{p\ n+1}^{\mathrm{tr}} = p_{0\ n}$
   b. evaluate $\boldsymbol{n}_{n+1}^{\mathrm{tr}}$ per Eq. (28)
2: **if** $\varphi(\boldsymbol{n}_{n+1}^{\mathrm{tr}}) \leq 0$ **then**
   a. the deformation is elastic per Eq. (29), set internal variables $(\cdot)_{n+1} = (\cdot)_{n+1}^{\mathrm{tr}}$
   b. set $\boldsymbol{\sigma}_{n+1} = \boldsymbol{C}^{\mathrm{e}} : \boldsymbol{\epsilon}_{n+1}^{\mathrm{e}}$ and the solid tangent $\boldsymbol{C}^{\mathrm{e}}$
3: **else**
   a. the deformation is inelastic, obtain the local system by parameterizing the Euler–Lagrange equation with $\boldsymbol{n}(\Delta\boldsymbol{\epsilon}_{n+1}^{\mathrm{p}})$, $\lambda(\Delta\boldsymbol{\epsilon}_{n+1}^{\mathrm{p}})$, and $\epsilon_v^{\mathrm{p}}(\Delta\boldsymbol{\epsilon}_{n+1}^{\mathrm{p}})$ under dependence $\Delta\boldsymbol{\epsilon}^{\mathrm{p}}(\boldsymbol{\epsilon}_{n+1}^{\mathrm{e}})$
   b. at local system iteration $k = 0$, guess the initial solution per Eq. (37)
   c. using Newton's method or a variant, iteratively solve the local nonlinear system for $\boldsymbol{\epsilon}_{n+1}^{\mathrm{e}}$
   d. set $\boldsymbol{\sigma}_{n+1} = \boldsymbol{C}^{\mathrm{e}} : \boldsymbol{\epsilon}_{n+1}^{\mathrm{e}}$ and the solid tangent $\boldsymbol{C}_{n+1}^{\mathrm{ep}}$ per Eq. (41)
4: Return mapping completes
   a. w.r.t the equilibrium equation, pass to the global system the stress $\boldsymbol{\sigma}_{n+1}$ and the solid tangent
   b. for the micromorphic regularization, also pass the local variables λ_{n+1} and $\epsilon_{v\ n+1}^{\mathrm{p}}$

Local nonlinearity is treated as follows. Define the local numerical system and residual in matrix–vector notation:

$$\left.\begin{aligned}\overline{\mathbf{x}}^k &= \left[\overline{\boldsymbol{\epsilon}}^{\mathrm{e}}_{n+1}\right]^k_{6\times 1}\\ \overline{\mathbf{r}}^k &= \Big[\,\mathbf{C}^{\mathrm{e}}\overline{\boldsymbol{\epsilon}}^{\mathrm{e}}_{n+1} - \sigma_{q\,n+1}\mathbf{B}_\lambda\overline{\mathbf{n}}_{n+1} - \sigma_{p\,n+1}\overline{\mathbf{b}}_v\\ &\qquad + k_\lambda\Big(\tilde{\lambda}_{n+1}-\lambda_{n+1}\Big)\mathbf{B}_\lambda\overline{\mathbf{n}}_{n+1} + k_v\Big(\tilde{\epsilon}^{\mathrm{p}}_{v\,n+1}-\epsilon^{\mathrm{p}}_{v\,n+1}\Big)\overline{\mathbf{b}}_v\,\Big]^k_{6\times 1}\end{aligned}\right\} \tag{35}$$

where k is the iteration, $\overline{\mathbf{x}}^k$ the Kelvin-notated vector equivalent of the local unknowns at k, $\overline{\mathbf{r}}^k$ the Kelvin-notated vector equivalent of the local residual at k, $\overline{\mathbf{b}}_v$ the Kelvin-notated vector equivalent of $\boldsymbol{b}_v$, and $\mathbf{B}_\lambda$ the Kelvin-notated vector equivalent of $\boldsymbol{B}_\lambda$ (for bold font and overline notation convention for Kelvin-notated equivalents, see Appendix A). The local tangent operator is then

$$\left.\frac{\partial\overline{\mathbf{r}}}{\partial\overline{\mathbf{x}}}\right|^k_{\overline{\boldsymbol{\epsilon}}^{\mathrm{e\,tr}}_{n+1}} = \left[\frac{\partial\overline{\mathbf{r}}}{\partial\overline{\boldsymbol{\epsilon}}^{\mathrm{e}}_{n+1}}\right]^k_{6\times 6}, \tag{36}$$

as derived in Appendix C.1, where

$$\begin{aligned}\frac{\partial\overline{\mathbf{r}}}{\partial\overline{\boldsymbol{\epsilon}}^{\mathrm{e}}_{n+1}} &= \mathbf{C}^{\mathrm{e}} + \frac{\sigma_{q\,n+1}}{\Delta\lambda}\left[\mathbf{B}_\lambda - (\mathbf{B}_\lambda\overline{\mathbf{n}}_{n+1})\,(\mathbf{B}_\lambda\overline{\mathbf{n}}_{n+1})^{\mathrm{T}}\right] - \frac{M}{2}\partial_{\epsilon^{\mathrm{p}}_v}p_{c\,n+1}\left[(\mathbf{B}_\lambda\overline{\mathbf{n}}_{n+1})\,\overline{\mathbf{b}}^{\mathrm{T}}_v + \overline{\mathbf{b}}_v\,(\mathbf{B}_\lambda\overline{\mathbf{n}}_{n+1})^{\mathrm{T}}\right]\\ &\quad + \frac{1}{2}\left(\partial_{\epsilon^{\mathrm{p}}_v}p_{c\,n+1} - M\Delta\lambda\partial^2_{\epsilon^{\mathrm{p}}_v\epsilon^{\mathrm{p}}_v}p_{c\,n+1}\right)\overline{\mathbf{b}}_v\overline{\mathbf{b}}^{\mathrm{T}}_v - \frac{k_\lambda\left(\tilde{\lambda}_{n+1}-\lambda_{n+1}\right)}{\Delta\lambda}\left[\mathbf{B}_\lambda - (\mathbf{B}_\lambda\overline{\mathbf{n}}_{n+1})\,(\mathbf{B}_\lambda\overline{\mathbf{n}}_{n+1})^{\mathrm{T}}\right]\\ &\quad + k_\lambda\,(\mathbf{B}_\lambda\overline{\mathbf{n}}_{n+1})\,(\mathbf{B}_\lambda\overline{\mathbf{n}}_{n+1})^{\mathrm{T}} + k_v\overline{\mathbf{b}}_v\overline{\mathbf{b}}^{\mathrm{T}}_v,\end{aligned}$$

and

$$\overline{\mathbf{n}}_{n+1} = \frac{\mathbf{B}_\lambda\Delta\overline{\boldsymbol{\epsilon}}^{\mathrm{p}}}{\Delta\lambda} = \frac{\mathbf{B}_\lambda\Delta\overline{\boldsymbol{\epsilon}}^{\mathrm{p}}}{\sqrt{\Delta\overline{\boldsymbol{\epsilon}}^{\mathrm{p}\,\mathrm{T}}\mathbf{B}_\lambda\Delta\overline{\boldsymbol{\epsilon}}^{\mathrm{p}}} + k_{\overline{\boldsymbol{\epsilon}}}} \quad \text{for} \quad \Delta\overline{\boldsymbol{\epsilon}}^{\mathrm{p}} = \overline{\boldsymbol{\epsilon}}^{\mathrm{e\,tr}}_{n+1} - \overline{\boldsymbol{\epsilon}}^{\mathrm{e}}_{n+1} \quad \text{with} \quad \mathbf{B}_\lambda\overline{\mathbf{n}}_{n+1} = \mathbf{B}^{\mathrm{T}}_\lambda\overline{\mathbf{n}}_{n+1}.$$

Small parameter $k_{\overline{\boldsymbol{\epsilon}}}$ is taken as 1×10^{-15}.

Our local tangent matrix $(\partial\overline{\mathbf{r}}/\partial\overline{\mathbf{x}})^k$'s symmetry redounds to the model design's variational consistency, the hallmark of which is the cascading dependence $p_c(\Delta\overline{\boldsymbol{\epsilon}}^{\mathrm{p}})$ and $\Delta\overline{\boldsymbol{\epsilon}}^{\mathrm{p}}(\overline{\boldsymbol{\epsilon}}^{\mathrm{e}}_{n+1})$, in this the MCC context.

4.1.1. Trial state

Converging a local system requires passing an initial guess to Newton's method. Our guess, at iteration $k=0$, approximates the elastic trial state:

$$\overline{\boldsymbol{\epsilon}}^{\mathrm{e}\,k=0}_{n+1} = \left[\overline{\boldsymbol{\epsilon}}^{\mathrm{e\,tr}}_{n+1} - \Delta\lambda\overline{\mathbf{n}}^{\mathrm{tr}}_{n+1}\right]^{k=0}_{6\times 1} \quad \text{for} \quad \Delta\overline{\boldsymbol{\epsilon}}^{\mathrm{p}\,k=0} = \left[\Delta\lambda\overline{\mathbf{n}}^{\mathrm{tr}}_{n+1}\right]^{k=0}_{6\times 1}. \tag{37}$$

Thus at $k=0$ we set $\overline{\boldsymbol{\epsilon}}^{\mathrm{e}}_{n+1}\approx\overline{\boldsymbol{\epsilon}}^{\mathrm{e\,tr}}_{n+1}$ and $\Delta\overline{\boldsymbol{\epsilon}}^{\mathrm{p}}\approx\overline{\mathbf{0}}$, with $\Delta\lambda^{k=0}$ a small number taken as 1×10^{-10}.

4.1.2. Stored work update

In-line with the semilogarithmic relation, we use as derivatives

$$p_{c\,n+1} = p_{c\,n}\exp\left(\frac{\epsilon^{\mathrm{e}}_{v\,n+1}-\epsilon^{\mathrm{e\,tr}}_{v\,n+1}}{C_d}\right), \quad \partial_{\epsilon^{\mathrm{p}}_v}p_{c\,n+1} = -\frac{p_{c\,n}}{C_d}\exp\left(\frac{\epsilon^{\mathrm{e}}_{v\,n+1}-\epsilon^{\mathrm{e\,tr}}_{v\,n+1}}{C_d}\right).$$

As such, the stored plastic work of consolidation's increments follow

$$W^{\mathrm{p}}_{c\,n+1} - W^{\mathrm{p}}_{c\,n} = p_{c\,n}C_d\left[1-\exp\left(\frac{\epsilon^{\mathrm{e}}_{v\,n+1}-\epsilon^{\mathrm{e\,tr}}_{v\,n+1}}{C_d}\right)\right] = C_d\,(p_{c\,n}-p_{c\,n+1})\,. \tag{38}$$

4.2. Consistent tangent operator (CTO)

A consistent tangent operator $\mathbf{C}^{\mathrm{ep}}_{n+1} = \partial\overline{\boldsymbol{\sigma}}_{n+1}/\partial\overline{\boldsymbol{\epsilon}}_{n+1}$ is useful to converge the global system for the displacements, cf. Eq. (7.127-136) in [59], also see the next section. The CTO is evaluated after convergence of the local system,

when

$$\frac{\partial \overline{\boldsymbol{\epsilon}}^{\mathrm{e\ tr}}_{n+1}}{\partial \overline{\boldsymbol{\epsilon}}_{n+1}} = \frac{\partial \left(\overline{\boldsymbol{\epsilon}}^{\mathrm{e}}_{n} + \overline{\boldsymbol{\epsilon}}_{n+1} - \overline{\boldsymbol{\epsilon}}_{n} \right)}{\partial \overline{\boldsymbol{\epsilon}}_{n+1}} = \mathbf{I}, \quad \text{hence} \quad \frac{\partial \overline{\boldsymbol{\epsilon}}^{\mathrm{e\ tr}}_{n+1}}{\partial \overline{\boldsymbol{\epsilon}}^{e}_{n+1}} = \frac{\partial \overline{\boldsymbol{\epsilon}}^{\mathrm{e\ tr}}_{n+1}}{\partial \overline{\boldsymbol{\epsilon}}_{n+1}} : \frac{\partial \overline{\boldsymbol{\epsilon}}_{n+1}}{\partial \overline{\boldsymbol{\epsilon}}^{e}_{n+1}} = \frac{\partial \overline{\boldsymbol{\epsilon}}_{n+1}}{\partial \overline{\boldsymbol{\epsilon}}^{e}_{n+1}},$$

whereas

$$\left.\frac{\partial \Delta \overline{\boldsymbol{\epsilon}}^{\mathrm{p}}}{\partial \overline{\boldsymbol{\epsilon}}^{\mathrm{e}}_{n+1}}\right|_{\overline{\boldsymbol{\epsilon}}^{\mathrm{e\ tr}}} = \left.\frac{\partial \left(\overline{\boldsymbol{\epsilon}}^{\mathrm{e\ tr}}_{n+1} - \overline{\boldsymbol{\epsilon}}^{\mathrm{e}}_{n+1} \right)}{\partial \overline{\boldsymbol{\epsilon}}^{\mathrm{e}}_{n+1}}\right|_{\overline{\boldsymbol{\epsilon}}^{\mathrm{e\ tr}}} = -\mathbf{I}, \quad \left.\frac{\partial \Delta \overline{\boldsymbol{\epsilon}}^{\mathrm{p}}}{\partial \overline{\boldsymbol{\epsilon}}^{\mathrm{e\ tr}}_{n+1}}\right|_{\overline{\boldsymbol{\epsilon}}^{\mathrm{e}}_{n+1}} = \left.\frac{\partial \left(\overline{\boldsymbol{\epsilon}}^{\mathrm{e\ tr}}_{n+1} - \overline{\boldsymbol{\epsilon}}^{\mathrm{e}}_{n+1} \right)}{\partial \overline{\boldsymbol{\epsilon}}^{\mathrm{e\ tr}}_{n+1}}\right|_{\overline{\boldsymbol{\epsilon}}^{\mathrm{e}}_{n+1}} = \mathbf{I}.$$

As CTO is evaluated after convergence of the local system, we drop superscripts k and $n+1$ and let $\overline{\mathbf{x}} = \overline{\boldsymbol{\epsilon}}^{\mathrm{e}}$, for the remainder of this section.

To identify the CTO, we rewrite the purely local Euler–Lagrange equation in residual form, as

$$\overline{\boldsymbol{\sigma}} - \overline{\mathbf{s}}(\Delta \overline{\boldsymbol{\epsilon}}^{\mathrm{p}}) = \overline{\mathbf{0}} \tag{39}$$

where $\overline{\mathbf{s}}$ corresponds to the plastic back-stress as described in [52], and is

$$\overline{\mathbf{s}}(\Delta \overline{\boldsymbol{\epsilon}}^{\mathrm{p}}) = \sigma_q \frac{\mathbf{B}_\lambda \Delta \overline{\boldsymbol{\epsilon}}^{\mathrm{p}}}{\sqrt{\Delta \overline{\boldsymbol{\epsilon}}^{\mathrm{p}\,\mathrm{T}} \mathbf{B}_\lambda \Delta \overline{\boldsymbol{\epsilon}}^{\mathrm{p}}}} + \sigma_p \overline{\mathbf{b}}_v \quad \text{and} \quad \Delta \overline{\boldsymbol{\epsilon}}^{\mathrm{p}} = \overline{\boldsymbol{\epsilon}}^{\mathrm{e\ tr}} - \overline{\boldsymbol{\epsilon}}^{\mathrm{e}} \quad \Rightarrow \quad \left.\frac{\partial \overline{\mathbf{r}}}{\partial \overline{\mathbf{x}}}\right|_{\overline{\boldsymbol{\epsilon}}^{\mathrm{e\ tr}}} = \mathbf{C}^{\mathrm{e}} + \frac{\partial \overline{\mathbf{s}}}{\partial \Delta \overline{\boldsymbol{\epsilon}}^{\mathrm{p}}},$$

assuming invertible $\partial \overline{\mathbf{r}} / \partial \overline{\mathbf{x}}$, the local system's tangent at the converged state from Eq. (36). Apply the identity $\overline{\boldsymbol{\sigma}} = \mathbf{C}^{\mathrm{e}} \overline{\boldsymbol{\epsilon}}^{\mathrm{e}}$ and differentiate the Euler–Lagrange equation in residual form,

$$\frac{\partial}{\partial \overline{\boldsymbol{\epsilon}}^{\mathrm{e}}} \left(\mathbf{C}^{\mathrm{e}} \overline{\boldsymbol{\epsilon}}^{\mathrm{e}} \right) - \frac{\partial \overline{\mathbf{s}}}{\partial \Delta \overline{\boldsymbol{\epsilon}}^{\mathrm{p}}} \left(\left.\frac{\partial \Delta \overline{\boldsymbol{\epsilon}}^{\mathrm{p}}}{\partial \overline{\boldsymbol{\epsilon}}^{\mathrm{e}}}\right|_{\overline{\boldsymbol{\epsilon}}^{\mathrm{e\ tr}}} + \left.\frac{\partial \Delta \overline{\boldsymbol{\epsilon}}^{\mathrm{p}}}{\partial \overline{\boldsymbol{\epsilon}}^{\mathrm{e\ tr}}}\right|_{\overline{\boldsymbol{\epsilon}}^{\mathrm{e}}} \frac{\partial \overline{\boldsymbol{\epsilon}}^{\mathrm{e\ tr}}}{\partial \overline{\boldsymbol{\epsilon}}^{\mathrm{e}}} \right) = \mathbf{C}^{\mathrm{e}} - \frac{\partial \overline{\mathbf{s}}}{\partial \Delta \overline{\boldsymbol{\epsilon}}^{\mathrm{p}}} \left(-\mathbf{I} + \mathbf{I} \frac{\partial \overline{\boldsymbol{\epsilon}}}{\partial \overline{\boldsymbol{\epsilon}}^{\mathrm{e}}} \right) = \overline{\mathbf{0}}. \tag{40}$$

Rearranging for

$$\frac{\partial \overline{\boldsymbol{\epsilon}}}{\partial \overline{\boldsymbol{\epsilon}}^{\mathrm{e}}} = \left(\frac{\partial \overline{\mathbf{s}}}{\partial \Delta \overline{\boldsymbol{\epsilon}}^{\mathrm{p}}} \right)^{-1} \left(\mathbf{C}^{\mathrm{e}} + \frac{\partial \overline{\mathbf{s}}}{\partial \Delta \overline{\boldsymbol{\epsilon}}^{\mathrm{p}}} \right),$$

$\mathbf{C}^{\mathrm{ep}}$ is evaluated via the chain rule. Noting that $\mathbf{C}^{\mathrm{ep}} = \partial \overline{\boldsymbol{\sigma}} / \partial \overline{\boldsymbol{\epsilon}} = \mathbf{C}^{\mathrm{e}} (\partial \overline{\boldsymbol{\epsilon}}^{\mathrm{e}} / \partial \overline{\boldsymbol{\epsilon}}) = \mathbf{C}^{\mathrm{e}} (\partial \overline{\boldsymbol{\epsilon}} / \partial \overline{\boldsymbol{\epsilon}}^{\mathrm{e}})^{-1}$,

$$\mathbf{C}^{\mathrm{ep}} = \left[\mathbf{C}^{\mathrm{e}} \left(\frac{\partial \overline{\boldsymbol{\epsilon}}}{\partial \overline{\boldsymbol{\epsilon}}^{\mathrm{e}}} \right)^{-1} \right]_{6\times 6} = \left[\mathbf{C}^{\mathrm{e}} \left(\left.\frac{\partial \overline{\mathbf{r}}}{\partial \overline{\mathbf{x}}}\right|_{\overline{\boldsymbol{\epsilon}}^{\mathrm{e\ tr}}} \right)^{-1} \left(\left.\frac{\partial \overline{\mathbf{r}}}{\partial \overline{\mathbf{x}}}\right|_{\overline{\boldsymbol{\epsilon}}^{\mathrm{e\ tr}}} - \mathbf{C}^{\mathrm{e}} \right) \right]_{6\times 6}, \tag{41}$$

where we have substituted to write $\mathbf{C}^{\mathrm{ep}}$ in $\mathbf{C}^{\mathrm{e}}$, and $\partial \overline{\mathbf{r}} / \partial \overline{\mathbf{x}}$. As such, the consistent tangent computation exclusively reuses the solid elastic tangent, $\mathbf{C}^{\mathrm{e}}$, and the local tangent at the converged state, $\partial \overline{\mathbf{r}} / \partial \overline{\mathbf{x}}$. On this point, contrast against [8]. Consequently, our implementation is straightforward and generic with respect to additional (e.g. micromorphic or viscoplastic) physics.

4.3. Spatial discretization

The stress $\boldsymbol{\sigma}$ and consistent tangent $\boldsymbol{C}^{\mathrm{ep}}$ evolved from solution of the quadrature point problem is used to converge the global equilibrium equation for the displacements $\boldsymbol{u}$. Unless otherwise noted, the spatial domain is discretized with standard low-order quadrilateral finite elements. The implementation of the spatial discretization is done using the finite element library `deal.ii` [60], whereas the implicit nonlinear PDE solver, including the assembly procedure of the residuals and the corresponding tangents, and the Newton–Raphson scheme are modified from the software code base `geocentric` [61,62].

5. Plastic flow near and at the anisotropic critical state

Consider Eq. (41). The local tangent is symmetric, and so is its inverse $(\partial \overline{\mathbf{r}} / \partial \overline{\mathbf{x}})^{-1}$. As such the product of $\mathbf{C}^{\mathrm{e}}$, $(\partial \overline{\mathbf{r}} / \partial \overline{\mathbf{x}})^{-1}$, and $\partial \overline{\mathbf{s}} / \partial \Delta \overline{\boldsymbol{\epsilon}}^{\mathrm{p}}$ is also symmetric. Therefore $\mathbf{C}^{\mathrm{ep}}$ is defined by a maximum of 21 independent components (being a symmetric six-by-six matrix). As such, the CTO tensor $\boldsymbol{C}^{\mathrm{ep}}$ exhibits not only the minor, but also the major, symmetry — this fact traces from the symmetry of second derivatives. A characteristic of variational constitutive updates, this is carefully noted in [52] for instance.

Consequently the stability analysis simplifies. For detained exposition, see for example Eq. (2-15) in [63]. However in brief, consider two solutions given by

$$\text{solution (i)}: \quad (\dot{\boldsymbol{\sigma}}, \dot{\boldsymbol{u}}), \quad \text{and} \quad \text{solution (ii)}: \quad (\dot{\boldsymbol{\sigma}}^*, \dot{\boldsymbol{u}}^*).$$

Solution (i) is the local solution, and satisfies the mechanical equilibrium equation and boundary conditions in rate form. Presume solution (ii) also satisfies the equilibrium equation and boundary conditions in rate form. Observe our material is incrementally linear, being that:

$$\frac{\partial \boldsymbol{s}}{\partial \Delta \boldsymbol{\epsilon}^{\mathrm{p}}} : \dot{\boldsymbol{\epsilon}}^{\mathrm{p}} = \frac{\partial \boldsymbol{s}}{\partial \Delta \boldsymbol{\epsilon}^{\mathrm{p}}} : \left(\dot{\boldsymbol{\epsilon}} - \dot{\boldsymbol{\epsilon}}^{\mathrm{p}}\right) = \boldsymbol{C}^{\mathrm{e}} : \dot{\boldsymbol{\epsilon}}^{\mathrm{e}}.$$

where we use Eq. (1). The rate of stress is then linear in the rate of strain, per

$$\dot{\boldsymbol{\sigma}} = \boldsymbol{C}^{\mathrm{e}} : \dot{\boldsymbol{\epsilon}}^{\mathrm{e}} = \overbrace{\boldsymbol{C}^{\mathrm{e}} : \left(\boldsymbol{C}^{\mathrm{e}} + \frac{\partial \boldsymbol{s}}{\partial \Delta \boldsymbol{\epsilon}^{\mathrm{p}}}\right)^{-1} : \frac{\partial \boldsymbol{s}}{\partial \Delta \boldsymbol{\epsilon}^{\mathrm{p}}}}^{\boldsymbol{C}^{\mathrm{ep}}} : \dot{\boldsymbol{\epsilon}}. \tag{42}$$

Hence operator $\boldsymbol{C}^{\mathrm{ep}}$ linearly relates $\dot{\boldsymbol{\sigma}}$ and $\dot{\boldsymbol{\epsilon}}$, necessitated by the definition of the CTO in Eq. (41). With incremental linearity established, the local uniqueness condition (to left) coincides with the local stability condition (to right):

$$[\![\dot{\boldsymbol{\epsilon}}]\!] : \left(\dot{\boldsymbol{\sigma}}^* - \dot{\boldsymbol{\sigma}}\right) > 0 \quad \text{and} \quad \mathrm{sym}(\boldsymbol{C}^{\mathrm{ep}}) = \boldsymbol{C}^{\mathrm{ep}} \iff [\![\dot{\boldsymbol{\epsilon}}]\!] : \boldsymbol{C}^{\mathrm{ep}} : [\![\dot{\boldsymbol{\epsilon}}]\!] > 0,$$

where $[\![\dot{\boldsymbol{\epsilon}}]\!] \neq \boldsymbol{0}$. Physically, $[\![\dot{\boldsymbol{\epsilon}}]\!]$ is interpreted physically as a jump in the strain rate $[\![\dot{\boldsymbol{\epsilon}}]\!] = \dot{\boldsymbol{\epsilon}}^* - \dot{\boldsymbol{\epsilon}}$.

With $\boldsymbol{C}^{\mathrm{ep}}$ super-symmetric, in that the constitutive update is variational, our evaluation of local stability simplifies. In particular, we avoid the oftentimes intricate procedures to resolve the roots of a second-order acoustic tensor, for elaboration cf. [64]. Instead for our $\boldsymbol{C}^{\mathrm{ep}}$ super-symmetric, the local uniqueness condition (to left) furthermore coincides with the determinate condition (to right):

$$[\![\dot{\boldsymbol{\epsilon}}]\!] : \left(\dot{\boldsymbol{\sigma}}^* - \dot{\boldsymbol{\sigma}}\right) > 0 \quad \text{and} \quad \mathrm{sym}(\boldsymbol{C}^{\mathrm{ep}}) = \boldsymbol{C}^{\mathrm{ep}} \iff \det(\mathrm{sym}(\boldsymbol{C}^{\mathrm{ep}})) = \det(\boldsymbol{C}^{\mathrm{ep}}) = 0,$$

where $[\![\dot{\boldsymbol{\epsilon}}]\!] \neq \boldsymbol{0}$ (also reference Eq. (9.4-9) in [36]).

Consequently, at last we motivate the immediately prior discussion on uniqueness and stability. Specifically consider the expression for the CTO, focusing on the micromorphic contribution to the consistent tangent in Eq. (41). From that equation, observe that unfortunately full rank of the local system $\partial \overline{\mathbf{r}}/\partial \overline{\mathbf{x}}$ is a necessary but not sufficient condition for invertibility of the consistent tangent $\mathbf{C}^{\mathrm{ep}}$. In particular for nonsingular $\mathbf{C}^{\mathrm{ep}}$, then the tangent of the plastic back-stress in the plastic strain increment $\partial \overline{\mathbf{s}}/\partial \Delta \overline{\boldsymbol{\epsilon}}^{\mathrm{p}}$ must also be nonsingular.

Accordingly, our reason to introduce multiple micromorphic fields becomes clear. Given that the volumetric plastic strain directly controls hardening behavior, per the exponential relations Eq. (7) and Eq. (8), it is immediately and physically intuitive to regularize ϵ_v through the field variable $\tilde{\epsilon}_v^{\mathrm{p}}$. However from the terms in the local tangent Eq. (36), for instance, observe that the volumetric field variable $\tilde{\epsilon}_v^{\mathrm{p}}$ contributes exactly nothing to $(\partial \overline{s}/\partial \Delta \overline{\epsilon}^{\mathrm{p}})_{ii}$ for $i \geq 4$ with $\overline{\mathbf{b}}_v \sim \overline{\mathbf{1}}$, as here.

Remark 4. As volumetric regularization contributes only $\overline{\mathbf{b}}_v \overline{\mathbf{b}}_v^{\mathrm{T}} \sim \overline{\mathbf{1}}\overline{\mathbf{1}}^{\mathrm{T}}$ to $\partial \overline{\mathbf{s}}/\partial \Delta \overline{\boldsymbol{\epsilon}}^{\mathrm{p}}$, we incorporate a second micromorphic field $\tilde{\lambda}$. Our goal is to circumvent the rank deficiency in the shear-associated sub-matrix of $\partial \overline{\mathbf{s}}/\partial \Delta \overline{\boldsymbol{\epsilon}}^{\mathrm{p}}$ (furthermore, which has physical significance as the tangent of the plastic stress in the increment of the plastic strain), such that $\partial \overline{\mathbf{s}}/\partial \Delta \overline{\boldsymbol{\epsilon}}^{\mathrm{p}}$ and hence the CTO are nonsingular. As highlighted immediately prior in this section, the determinate and uniqueness conditions coincide for $\boldsymbol{C}^{\mathrm{ep}} = \mathrm{sym}(\boldsymbol{C}^{\mathrm{ep}})$. Thus by adding the second field $\tilde{\lambda}$, we extend the well-posedness of certain boundary value problems, for instance during strain localization. Hence our purpose in regularizing the equivalent plastic strain differs from the gradient-dependent MCC model in [13], for instance, who attribute benefit from λ-regularization to their $\lambda \in \mathbb{R}^+ \cup \{0\}$ and $\dot{\lambda} \geq 0$, in comparison to the plastic strain's trace which, as emphasized in [13], may decrease.

5.1. Micromorphic regularization as remedy for volume locking

As pointed out in [15,17] and recently in [29], volume locking may occur in low-order finite element when volume-preserving plastic flow occurs. While selective integration or assume strain formulation may overcome the

Table 1
Anisotropy rubric.

	Micromorphic isotropy	Micromorphic anisotropy
Local isotropy	LI-MI	LI-MA
Local anisotropy	LA-MI	LA-MA

locking, these treatments must be used with stabilized formulation or hourglass control to prevent spurious spatial oscillation [65–68].

In essence, the regularization provided by the gradient-dependent diffusive functional Eq. (13) is both an effective localization limiter, penalizing the difference between the local plastic strain ϵ_v^{p} and the assumed strain $\tilde{\epsilon}_v^{\mathrm{p}}$ regularized via a Helmholtz equation, as well as a stabilization term. In other words, the avoidance of locking is attributable to: undesirable over-sampling of volumetric sampling points for numerical integration in low-order finite elements overcome by the Laplacian operator in the Helmholtz equation. The regularization method constrains the spatial fluctuation of the both the local plastic strain ϵ_v^{p} and the assumed strain $\tilde{\epsilon}_v^{\mathrm{p}}$ (provided that the length scale parameter $\tilde{l}_v = l_v\sqrt{K_v/k_v}$ is sufficiently large relative to the mesh size).

In that two micromorphic variables are introduced, note that effects of $\tilde{\lambda}$ scale with k_λ. In the next section, our numerical experiments are converged through sequenced strain localization events using (relatively) small values of k_λ, as compared to a_λ and hence to the volumetric a_v. While a complete mathematical analysis is out of the scope of this paper (but will be considered in the future), interested readers may refer to the assumed deformation gradient formulation in Section 3 of Sun et al. [15]) for a similar strategy applied to volume-preserving poroelasticity problems.

6. Numerical examples

We present two sets of boundary value problems, testing the proposed model's capability to replicate size-dependent anisotropy, and examining the effects of anisotropy across different length scales on formation of deformation bands, at various initial consolidation states. The first set of simulations represents 2D plane strain compression, with the anisotropic numerical specimen oriented such that every structural direction, such as microstructural vector $\boldsymbol{l}$, is in-plane. In contrast, the 3D simulations are designed to showcase 3D anisotropic responses in drained triaxial compression tests.

Unless otherwise specified, we assign dimensions on diagrams in mm and approximate the elastic parameter μ_l using Eq. (46). For materials that exhibit a plastically isotropic response, we set $\boldsymbol{b}_v = \mathbf{1}$, and

$$\overbrace{\alpha^{\mathrm{dev}} = \beta^{\mathrm{dev}} = \gamma^{\mathrm{dev}} = \alpha^{\mathrm{vol}} = \beta^{\mathrm{vol}} = \gamma^{\mathrm{vol}}}^{\text{purely local coefficients}} = 1, \quad \overbrace{\phi_\lambda = \chi_\lambda = \phi_v = \chi_v}^{\text{micromorphic coefficients}} = 0. \tag{43}$$

For $\boldsymbol{b}_v = \mathbf{1}$ and $\boldsymbol{P}^{\mathrm{p\,vol}} = \boldsymbol{I}$, this implies $\boldsymbol{b}_v = \boldsymbol{P}^{\mathrm{p\,vol}\,-1} : \mathbf{1} = \mathbf{1}$ (cf. Appendix C).

To capture the growth of micromorphic field variables' boundary layer, the length scale must be sufficiently larger than the mesh size. Furthermore, in the numerical examples presented in this section, the micromorphic material parameters are identified by introducing the following assumptions to simplify the calibration procedure. First, we assume that $\tilde{l}_\lambda = \tilde{l}_v$ per Eq. (33). This treatment implies that $k_\lambda = K_\lambda$ and $k_v = K_v$, unless otherwise noted. In turn, K_λ and K_v are parameterized by a_λ and a_v, as given by Eq. (14). Unless otherwise noted, the local direction vector $\boldsymbol{l}$ is equal to $\boldsymbol{l}_\lambda = \boldsymbol{l}_v$. The displacement prescribed in the boundary leads to compression in the axial direction.

Anisotropy of the local material response vs. anisotropy associated with the micromorphic field variables' diffusivity tensors is categorized by the rubric in Table 1. The table's entries are used to classify our numerical examples and parameterizations thereof.

6.1. 2D plane strain compression

The geometry of the plane strain test is presented in Fig. 4(a). This figure represents uniaxial compression with a uniform, compressive, and normal confining stress σ_c applied at the lateral boundaries. The material initial state is specified by the over-consolidation ratio (OCR). For the highly overconsolidated simulations, OCR = 30 and $p_{c\,0} =$

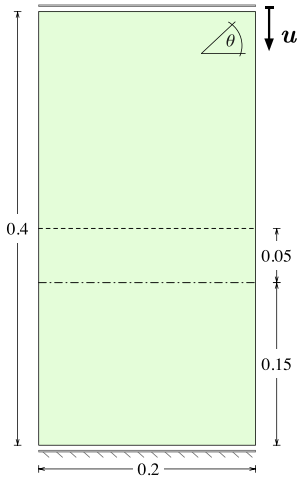

(a) Setup of the boundary value problem, with normal confining stress σ_c applied along lateral boundaries.

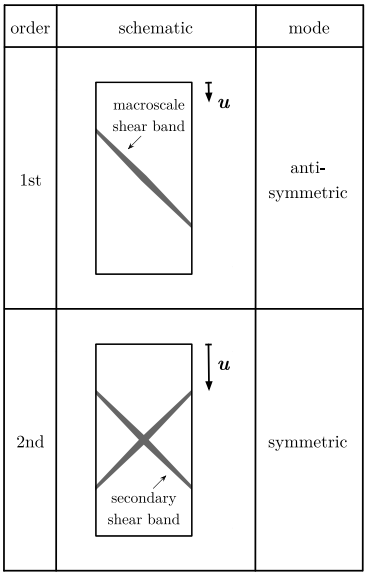

(b) Relevant antisymmetric and symmetric mode types.

Fig. 4. Geometry of the numerical specimen for plane strain plasticity simulations, showing: (a) the sampled transects as a dashed line and a dot-dashed line; and, (b) bifurcation modal schematic abridged from the interpretation of Ikeda et al. [69].

-30 MPa, implying $\sigma_c = -1$ MPa. For simulations performed on a normally consolidated numerical specimen, we set $p_{c\,0}$ to be -30 MPa, hence $\sigma_c = -30$ MPa. The loading increment along the displacement-controlled boundary is $\Delta u_2 = -5.0 \times 10^{-6}$ mm downwards.

The local material parameters loosely coordinate with the calibrated parameters for the Tournemire shale specimen (cf. Appendix E). Due to the introduction of anisotropy from the micromorphic regularization, the material parameters are adjusted to distinguish the material-point and mesoscale anisotropies as follows. The elastic response is characterized by the Young's modulus and Poisson ratio $E = E_{\boldsymbol{l}} = 14000$ MPa and $\nu = \nu_{\boldsymbol{l}} = 0.20$. Microstructural direction $\boldsymbol{l}$ and the eigenvectors of the micromorphic diffusivities are varied in the numerical examples to examine the anisotropic responses.

The slope of the critical state line in the fictitious isotropic stress-space and the modified compression index are $M = 1.2$ and $C_d = 0.005$ accordingly. Anisotropic plasticity material parameters are labeled in the parametric studies. In general, in this section, the local and micromorphic material parameters are not varied simultaneously, such that their respective influence can be individuated. Micromorphic length scales are $\tilde{l}_\lambda = \tilde{l}_v = 0.005$ mm, whereas $K_\lambda = a_\lambda \times 10^{-2}$, and $K_v = a_v$. Heuristically from the numerical simulations we ran, K_λ / k_λ and K_v / k_v must be sufficiently small such that the numerical boundary value problem remains solvable.

The initial mesh is conformal with the geometry in Fig. 4(a). The rectangular quadrilateral cells in each row number 7, and the elements in each column number 15, totaling $n_0 = 105$ elements in the initial mesh. Each additional level of refinement equally partitions every cell at the previous level of refinement into four cells (in 2D). Therefore, the refined mesh contains $n_0 \times 4^{l_h}$ cells for l_h levels of refinement. For all simulations excluding the mesh refinement study, $l_h = 3$.

At a high OCR, local anisotropy induces staggered antisymmetric and subsequent symmetric strain localization. The localization modes are characterized in Fig. 4(b). Fig. 5 evidences the model's numerical recovery of these modes. Fig. 5(a) show the response of the numerical specimen composed of an isotropic material with symmetric loading. Hence, only the symmetric localization modes are recovered in the numerical simulations. For the case where the microstructural angle $\theta_{\boldsymbol{l}} = 0$ in Fig. 5(b), the material is anisotropic but the local microstructural direction coincides with the normal vector describing a plane of loading symmetry. In this case, only symmetric shear bands

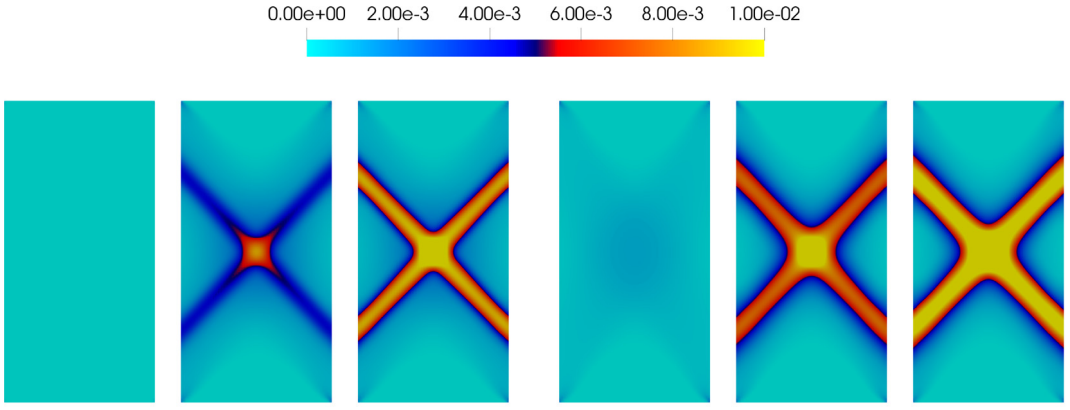

(a) Local elastoplastic isotropy.

(b) Local anisotropy with $\theta_l = 0$.

(c) Local anisotropy with $\theta_l = \pi/4$.

(d) Local anisotropy with $\theta_l = \pi/2$.

Fig. 5. Equivalent plastic strain λ for plane strain compression isotropic case vs. anisotropic cases with OCR $=$ 30 and rotation of microstructural direction, inducing local anisotropy in (b–d) by setting $E = 2400$ MPa and $\beta^{\text{dev}} = \beta^{\text{vol}} = 0.8$, at $u_2 = -0.4,\ -0.8,\ -1.0 \times 10^{-3}$ mm (LA-MI, see Table 1 for classification).

form. On the contrary, in the case where $\theta_l = \pi/4$ in Fig. 5(c), the microstructural direction misaligns with the loading's symmetry. An antisymmetric mode localizes at $u_2 = -0.8 \times 10^{-3}$ mm, preceding the secondary symmetric mode at 1.0×10^{-3} mm.

In two important scenarios, strain localization is effectively suppressed due to the change of the orientation of the numerical specimen. In the case shown in Fig. 5(d), the orientation of the transversely isotropic plane at $\theta_i = pi/2$ leads to reduction of compliance in the loading direction and therefore staunches strain localization. On the other hand, the plastic strain is diffusive at lower OCR, as shown in Fig. 6. This is achieved by lowering the OCR, hence σ_c to -30 MPa. The evidence showcased in this parametric study indicates that the plastic flow and hardening can both be affected by (1) rotating the microstructural direction and/or (2) increasing lateral compression. Different material orientations leading to different constitutive responses indicates that the anisotropy of the material is captured.

Hardening is captured quantitatively in Fig. 7(a) and (b), corresponding respectively to $\boldsymbol{l}$-rotation and diminishing σ_c. We compare global body-averaged values for the material state, Figs. 8 and 9. The regularized model captures phase change induced by local material anisotropy and/or degree of initial consolidation. Most notably, in Fig. 8, rotation of the microstructural direction itself induces phase change $\boldsymbol{l}$. In particular, for microstructural angle $\theta_l = \pi/2$, the deformation remains both diffuse and compactive. Similarly, for normal consolidation with OCR $= 1$ in Fig. 9, p^* grows monotonically more compressive with decreasing ϵ_v.

6.1.1. Diffusive anisotropy study

In this parametric study, we does not introduce anisotropy in the local material parameters, i.e. the classical MCC is used in the local constitutive update. Instead, we introduce anisotropy in the diffusion term of the Helmholtz

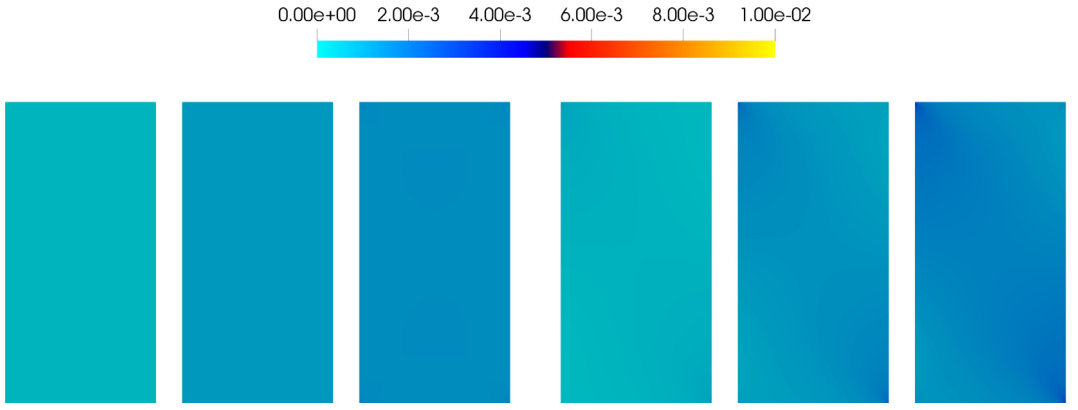

(a) Isotropy. **(b)** Local anisotropy with $\theta_l = \pi/4$.

Fig. 6. Equivalent plastic strain λ for comparison of isotropic vs. anisotropic plane strain compression cases with OCR $= 1$ and hence normal consolidation, inducing local anisotropy in (b) by setting $E = 2400$ MPa and $\beta^{\text{dev}} = \beta^{\text{vol}} = 0.8$, at $u_2 = -0.4,\ -0.8,\ -1.0 \times 10^{-3}$ mm (LA-MI).

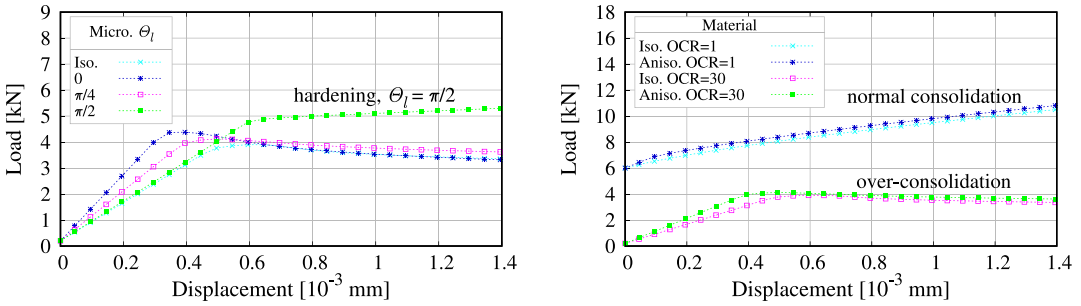

(a) Local isotropy vs. anisotropy with rotation of $\boldsymbol{l}$. **(b)** Over-consolidation vs. normal consolidation.

Fig. 7. Plane strain compression case with isotropy and anisotropy comparisons, vertical force vs. vertical displacement curves, showing: (a) isotropic case vs. anisotropic cases with increasing microstructural angle θ_l; and, (b) isotropy vs. anisotropy with $\theta_l = \pi/4$ at two over-consolidation ratios (OCR) (LA-MI).

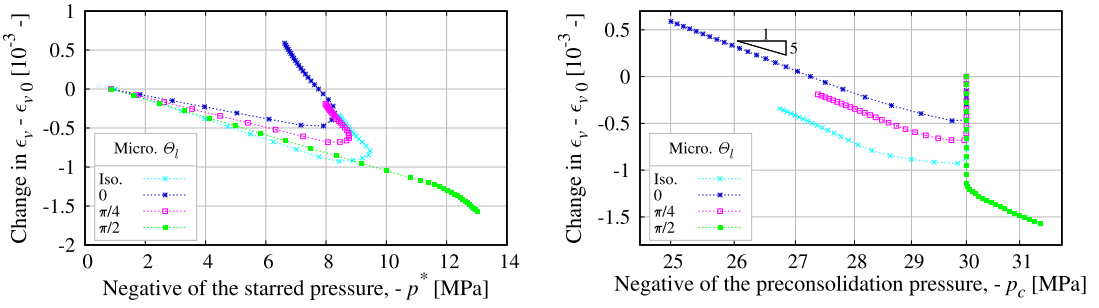

(a) Body-averaged state path. **(b)** Semilog plot evidencing fair recovery for the isotropic case of the slope $-(C_d) \times 10^3$.

Fig. 8. Plane strain compression case comparing local isotropy and anisotropy with increasing microstructural angle θ_l, globally averaged material state curves, showing: (a) and (b), loading paths for change in ϵ_v, such that loading paths begin at 0 in the ordinate axis (LA-MI).

equation. The resultant gradient-dependent plastic flow induces anisotropy. As such, both the plastic flow and the consequent strain localization can be manipulated by the diffusive field mapping in Eq. (15).

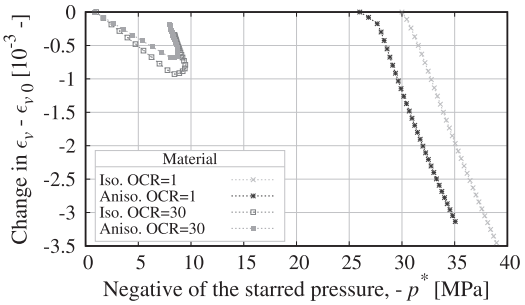

(a) Body-averaged state path, computing $-p^*$ with p^* by Eq. (10).

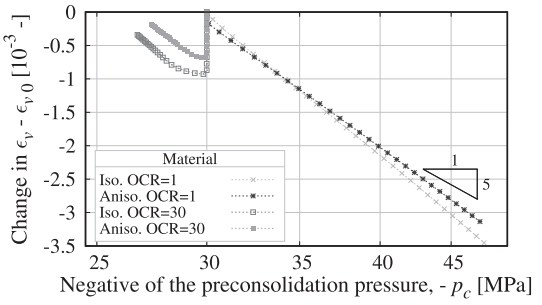

(b) Semilog plot evidencing fair recovery for the homogeneously deforming bodies of the slope $-(C_d) \times 10^3$, absent localization with OCR = 1.

Fig. 9. Plane strain compression case comparing local isotropy and anisotropy with microstructural angle $\theta_l = \pi/4$ at two over-consolidation ratios (OCR), globally averaged material state curves, showing: (a) and (b), loading paths for change in ϵ_v, such that loading paths begin at 0 in the ordinate axis. Note that cases labeled OCR = 30 correspond to Fig. 5(a–b) and OCR = 1 to Fig. 6(a–b) (LA-MI).

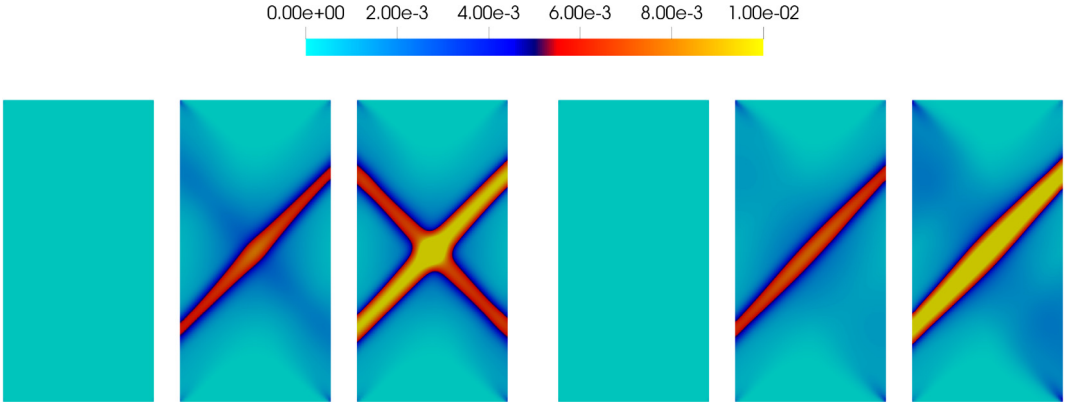

(a) Anisotropic diffusion $\phi_v = 1$.

(b) Anisotropic diffusion $\phi_v = 16$.

Fig. 10. Equivalent plastic strain λ for diffusively anisotropic plane strain compression case, with $\boldsymbol{l}_v$ described by $\theta_v = \pi/4$, at $u_2 = -0.4,\ -0.8,\ -1.0 \times 10^{-3}$ mm.

Micromorphic anisotropy alters both the bifurcation modes and the persistent shear band (the dominant pattern of the localized deformation [48]). Fig. 10 demonstrates the distribution of the equivalent plastic strain in the numerical specimen. Specifically, increasing $\phi_v > 0$ induces an antisymmetric localization mode parallel to diffusivity's eigenvector direction $\boldsymbol{l}_v$; compare Fig. 10(a) to (b).

Previous studies have considered this effect, Forest [9] for instance. However, our examples' parameterization highlights two inter-linked consequences. The micromorphic diffusivity's anisotropy promotes both antisymmetric strain banding (cf. Fig. 4(b)), and also rotation of the plastic strain's eigenvector direction. Notably this parameterization's the local material parameters are isotropic, such that practically the model reduces to the isotropic two-invariant minimization of Ortiz and Pandolfi [43]. Nonetheless the mesoscale material response is clearly anisotropic. Clearly, the orientation of the plastic strain's direction changes with the increasingly anisotropic diffusivity tensor, per Fig. 11.

In that the mesoscale plastic deformation is anisotropic, the band's antisymmetry exacerbated by increasing ϕ_v. Parameter ϕ_v controls the anisotropy of the diffusivity tensor, and changes from 0 (the isotropic case) to 16. In Fig. 11, this parameter is shown to control rotations of the plastic strain direction. Changing the principal direction indicates that the anisotropic regularization alone is sufficient to induce a globally anisotropic responses in the numerical specimen. Yet, such a change in the plastic flow direction does not require the introduction of a nonassociative plastic potential.

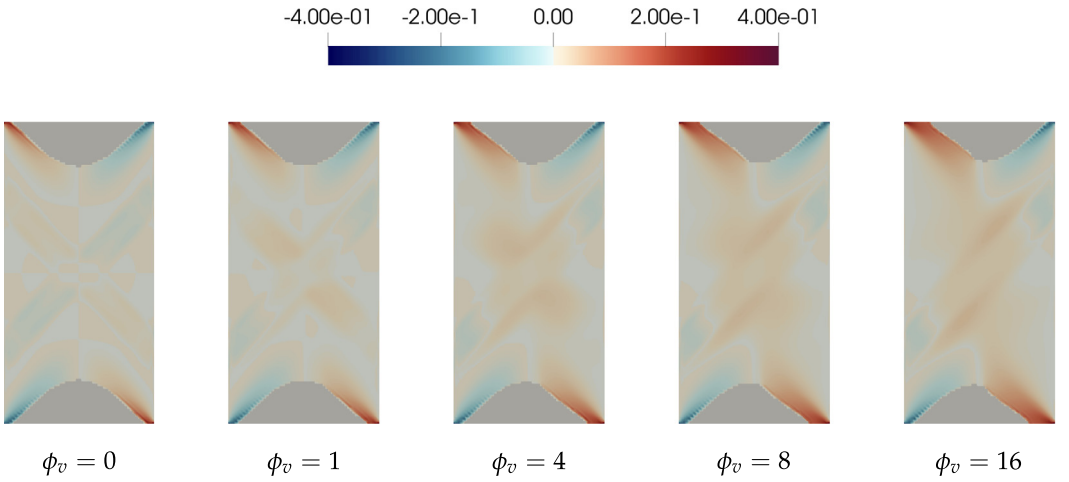

Fig. 11. Angle from horizontal of plastic strain's eigenvector corresponding to its greatest (most dilative) in-plane eigenvalue (in radians), for diffusively anisotropic plane strain compression case, with $\boldsymbol{l}_v$ described by $\theta_v = \pi/4$, at $u_2 = -1.0 \times 10^{-3}$ mm. Regions where $\boldsymbol{\epsilon}^{\mathrm{p}} = \mathbf{0}$ are grayed-out (LI-MA).

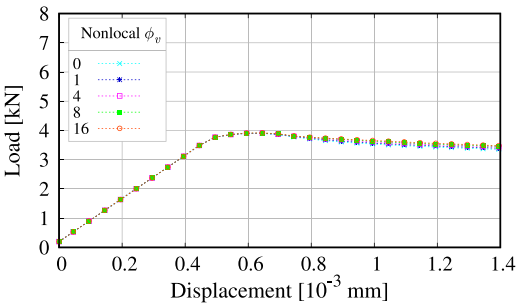

(a) Force-displacement curves.

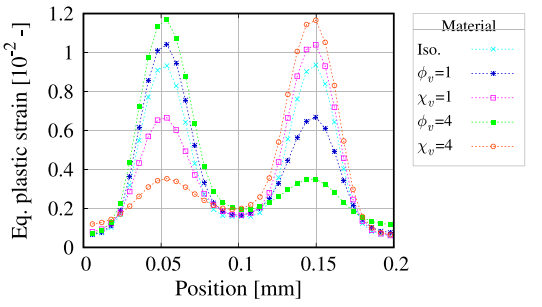

(b) Profiles of equivalent plastic strain λ, at $u_2 = -1.0 \times 10^{-3}$ mm.

Fig. 12. Diffusively anisotropic plane strain compression case, showing: (a) vertical force vs. vertical displacement curves with increasing anisotropic diffusion ϕ_v; and, (b) profiles of equivalent plastic strain λ across transect indicated as a dot-dashed line in Fig. 4(a) (LI-MA).

In contrast to ϕ_v, increasing χ_v in Fig. 12(b) engenders much the same bifurcation mode as local anisotropy in Fig. 5(c). As measured by the reaction force in Fig. 12(a), for these cases, the micromorphic anisotropy insignificantly affects the force–displacement curves. Yet, the anisotropy in the diffusion term nonetheless imposes noticeable influence on the spatial distribution of equivalent plastic strain as shown in Fig. 12(b). This combination indicates that the diffusivity can help to calibrate the macroscopic localization pattern, independent of the reaction forces.

To analyze whether micromorphic material parameters can be identified from inverse problems such that the resultant material laws can replicate the plastic deformation and pattern of strain localization consistent with observations, we conduct additional simulations with different values for the micromorphic material parameter k_v. Recall that increasing this material parameter will make any discrepancy between the local plastic volumetric strain ϵ_v^p measure and the field value $\tilde{\epsilon}_v^p$ costs more energy. Therefore, as the value of k_v increases, the influence of the anisotropic responses also increase such that (1) the resultant plastic strain becomes more diffusive and (2) the principal direction of the plastic strain rotates in response to the anisotropy induced by the diffusivity tensor, as shown in Figs. 13 and 14.

This point merits further numerical investigation regarding macroscopic strain-hardening, as well. In Figs. 15 and 16, the relaxation stiffnesses k_λ and k_v are simultaneously increased over the baseline values. The plastic deformation phases change to hardening, with no remainder strain localization, at the maximum tested k_λ. Under consideration

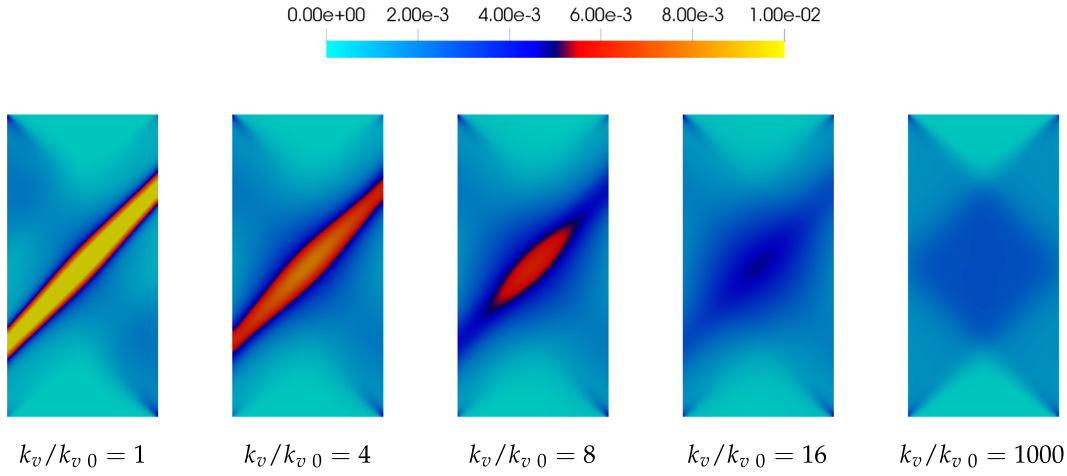

Fig. 13. Equivalent plastic strain λ for diffusively anisotropic plane strain compression case, with $\phi_v = 16$ and $\boldsymbol{l}_v$ described by $\theta_v = \pi/4$, at $u_2 = -1.0 \times 10^{-3}$ mm (LI-MA).

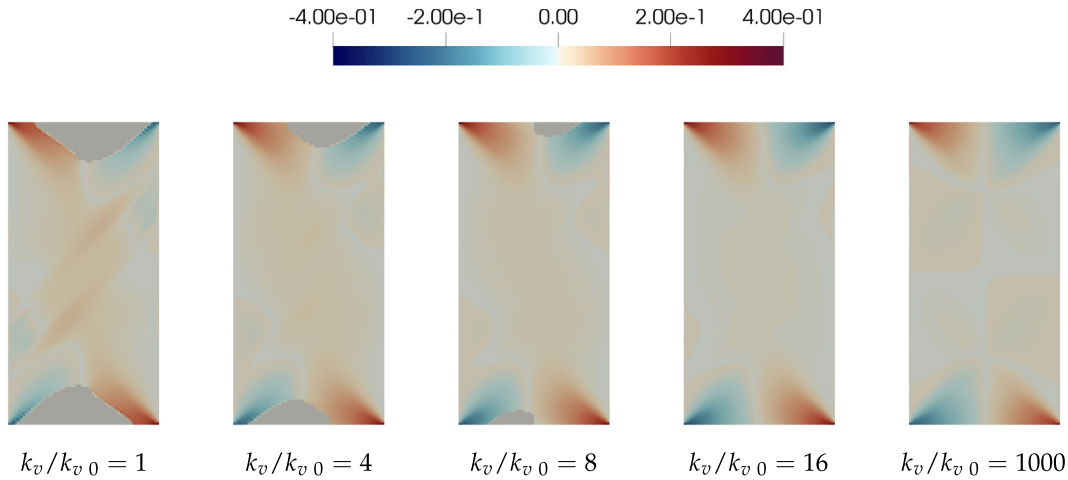

Fig. 14. Angle from horizontal of plastic strain's eigenvector corresponding to its greatest (most dilative) in-plane eigenvalue (in radians), for diffusively anisotropic plane strain compression case, with $\phi_v = 16$ and $\boldsymbol{l}_v$ described by $\theta_v = \pi/4$, at $u_2 = -1.0 \times 10^{-3}$ mm. Regions where $\boldsymbol{\epsilon}^{\mathrm{p}} = \mathbf{0}$ are grayed-out (LI-MA).

of Eq. (13), we observe that penalization of differences between the local internal variables vs. the micromorphic field reorients the plastic strain direction, most noticeably away from the fixed-displacement boundaries.

The reaction forces for parameterizations of the penalty stiffnesses, Fig. 17, concur with our attribution of phase change due to increasing k_λ. Overall, increasing the equivalent plastic strain λ-associated relaxation stiffens is observed to yield macroscopic plastic strain patterns similar to normal consolidation. Moreover, the equivalent plastic strain distributes essentially evenly across the body.

6.1.2. Mesh refinement study

Fig. 18 demonstrates the convergence toward mesh-independent behavior, attributable to the micromorphic regularization. For a relatively large characteristic element length h with $l_h = 1$ as in Fig. 18(a), the mesh is simply too coarse to resolve the regularizing field variable's gradient. For $l_h \geq 3$ in Fig. 18(b–c), the gradient profile is sufficiently resolved. As a consequence for $l_h \geq 3$, the boundary force–displacement curves overlap during softening per Fig. 19(a). Also across the transects in Fig. 19(b), differences between the local λ's maximal and minimal values significantly reduce for increasing l_h.

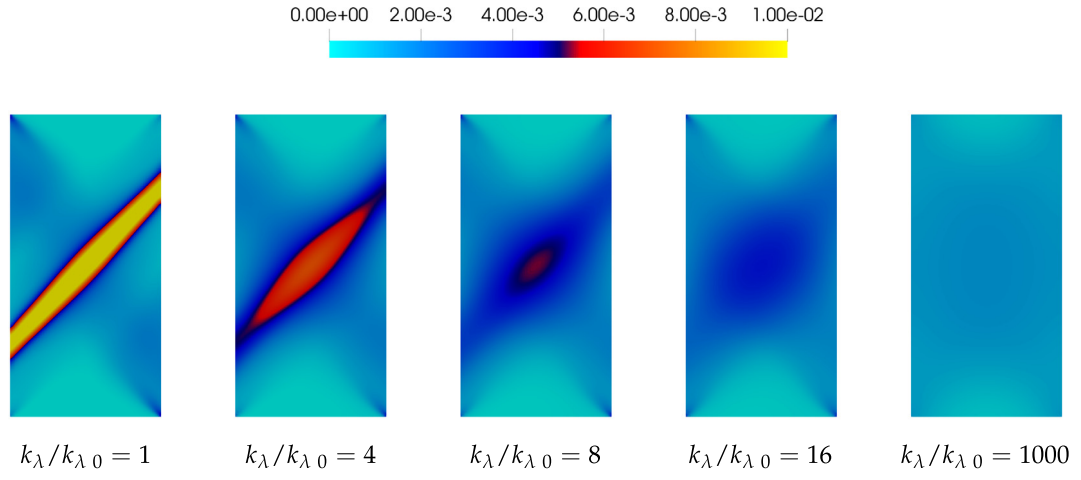

Fig. 15. Equivalent plastic strain λ for diffusively anisotropic plane strain compression case, with $\phi_v = 16$ and $\boldsymbol{l}_v$ described by $\theta_v = \pi/4$, at $u_2 = -1.0 \times 10^{-3}$ mm. Labeled by $k_\lambda/k_{\lambda\,0}$, however this parameterization holds $k_\lambda/k_{\lambda\,0} = k_v/k_{v\,0}$ (LI-MA).

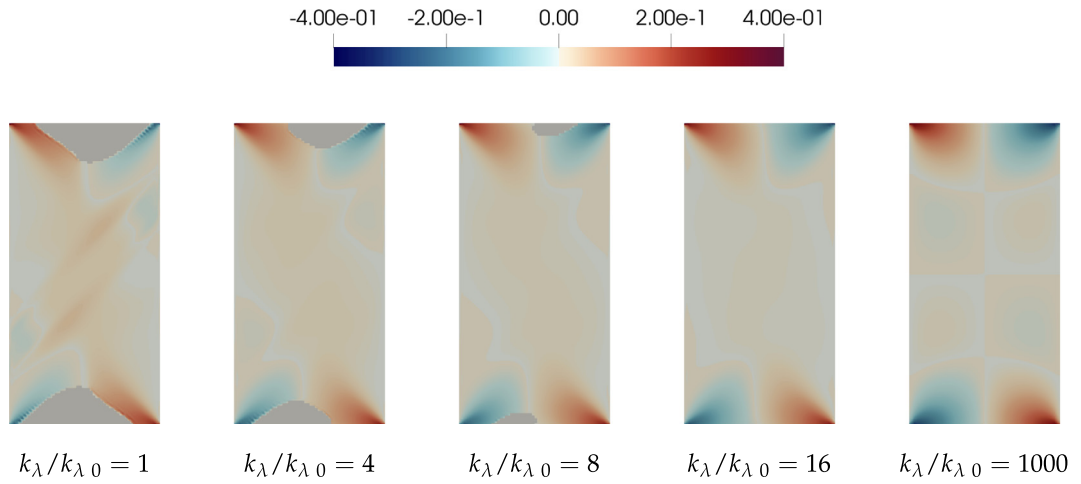

Fig. 16. Angle from horizontal of plastic strain's eigenvector corresponding to its greatest (most dilative) in-plane eigenvalue (in radians), for diffusively anisotropic plane strain compression case, with $\phi_v = 16$ and $\boldsymbol{l}_v$ described by $\theta_v = \pi/4$, at $u_2 = -1.0 \times 10^{-3}$ mm. Labeled by $k_\lambda/k_{\lambda\,0}$, however this parameterization holds $k_\lambda/k_{\lambda\,0} = k_v/k_{v\,0}$. Regions where $\boldsymbol{\epsilon}^{\mathrm{p}} = \boldsymbol{0}$ are grayed-out (LI-MA).

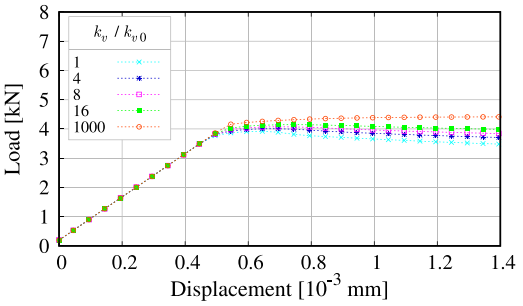

(a) Diffusive anisotropy with increasing only $k_v/k_{v\,0}$.

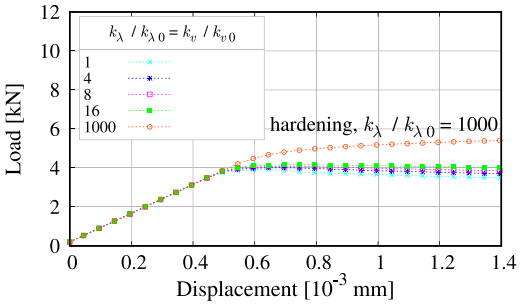

(b) Diffusive anisotropy with increasing $k_\lambda/k_{\lambda\,0} = k_v/k_{v\,0}$.

Fig. 17. Plane strain compression case with increasing penalty stiffness, vertical force vs. vertical displacement curves, showing: (a) $\phi_v = 16$ and varying $k_v/k_{v\,0}$ only; and, (b) $\phi_v = 16$ and varying $k_\lambda/k_{\lambda\,0} = k_v/k_{v\,0}$ (LI-MA).

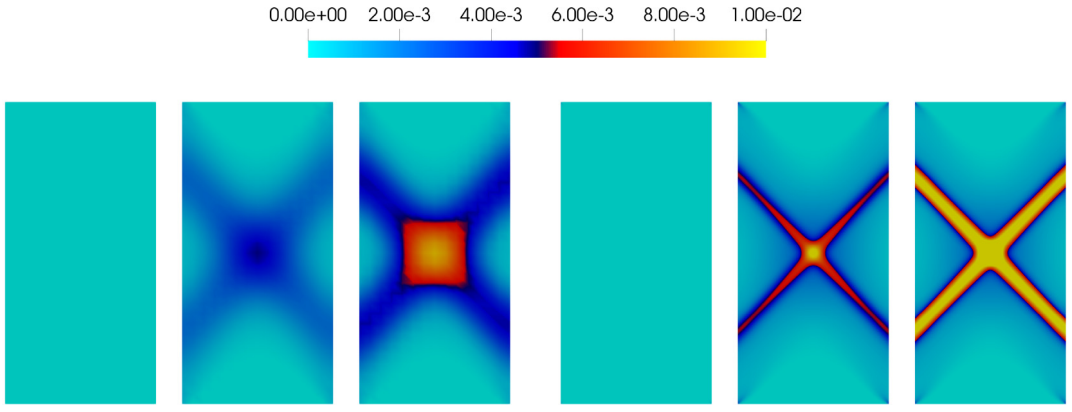

(a) Refinement level $l_h = 1$. **(b)** Refinement level $l_h = 4$.

Fig. 18. Equivalent plastic strain λ for isotropic plane strain compression case with mesh refinement, at $u_2 = -0.4,\ -0.8,\ -1.0 \times 10^{-3}$ mm (LI-MI).

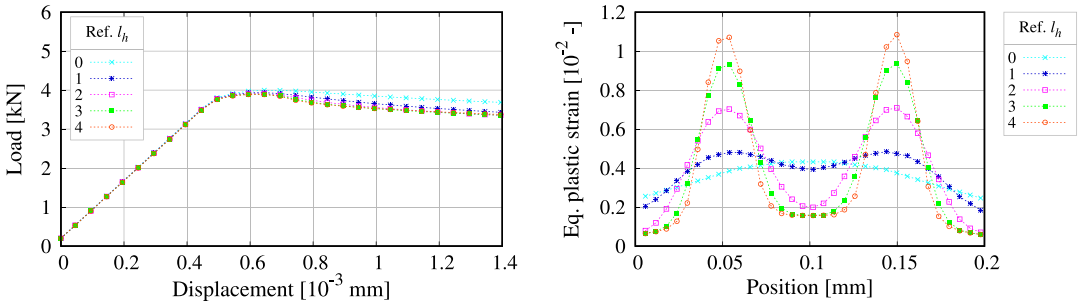

(a) Force-displacement curves. **(b)** Profiles of equivalent plastic strain λ, at $u_2 = -1.0 \times 10^{-3}$ mm.

Fig. 19. Isotropic plane strain compression case with mesh refinement, showing: (a) vertical force vs. vertical displacement curves, with visually overlapping curves for additional refinement levels $l_h = 3$ and $l_h = 4$; and, (b) profiles of equivalent plastic strain λ across transect indicated as a dashed line in Fig. 4(a). Note that cases for the refinement levels $l_h = 1, 4$ correspond to Fig. 18 (LI-MA).

Convergence of the boundary forces with increasing mesh refinement proves to be a good proxy for convergence of the globally averaged material state, Fig. 20(a). Two trends merit further discussion. First as l_h increases, both p_c and p^* converge simultaneously, during the material softening phase postceding the elastic deformation, labeled on Fig. 20(a) and clear in Fig. 20(b). Second, convergence during plastic deformation coincides with sharpening symmetric mode shear bands; compare to the profile of equivalent plastic strain λ in Fig. 19(b) for $l_h \geq 3$.

Lastly, certain meshes are too coarse and poorly capture localization, e.g. refinement level $l_h \leq 1$, see Fig. 18(a). Conversely, these coarse meshes exhibit diffuse softening, and therefore the globally averaged ϵ_v vs. $-p_c$ semilog curves approach the slope predicted by the local hardening rule in Eq. (7). In particular, $l_h = 0$ is associated with a purely concave equivalent plastic strain λ profile in Fig. 19(b). In our case however, due to the micromorphic regularization, increased mesh refinement facilitates resolving the shear bands, along with convergence of the global state path and boundary force.

Figs. 18–20 and the mesh refinement study are treated as a baseline for the diffusive anisotropy. For the isotropic baseline cases, the normalization Eq. (33) describes an approximate maximum for the mesh characteristic length. Subsequently, inducing micromorphic anisotropy, any $\phi_\lambda > 0$ or $\chi_\lambda > 0$ guarantee out-diffusion of the field variable $\tilde{\lambda}$. Hence inevitably, by dint of this parameterization, we sufficiently resolve the regularizing field's gradient. The same holds for $\tilde{\epsilon}^{\mathrm{p}}_v$, see Eq. (15).

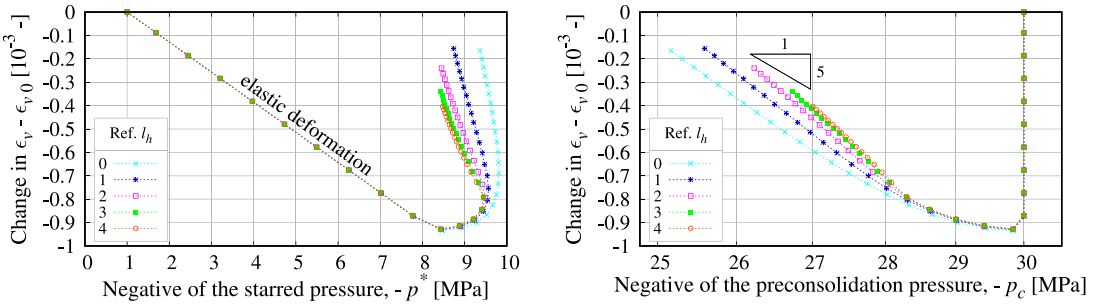

(a) Body-averaged state path, evidencing convergence with additional mesh refinement as refinement level l_h increases.

(b) Semilog plot evidencing convergence with additional mesh refinement, but departing from recovery for the inhomogeneously deforming bodies of the slope $-(C_d) \times 10^3$, as strain localizes with OCR = 30.

Fig. 20. Isotropic plane strain compression case with mesh refinement, globally averaged material state curves, showing: (a) and (b), loading paths for change in ϵ_v, such that loading paths begin at 0 in the ordinate axis. Note that cases for the refinement levels $l_h = 1, 2, 3, 4$ correspond to Fig. 18(a–d) (LI-MA).

6.1.3. Micromorphic stiffness study

Thus far in Section 6.1, shear bands develop within the simulated domain, while retaining numerical stability, at the rate-independent limit. In this subsection, we show the credit for this combination accrues to the pressure-dimensioned coefficients in Eq. (14). Viz., nonlocal equivalent plastic strain $\tilde{\lambda}$'s micromorphic stiffness was a small but workable value, $K_\lambda = a_\lambda \times 10^{-2}$. In contrast, the nonlocal trace $\tilde{\epsilon}_v^{\mathrm{p}}$'s stiffness was relatively greater, with $K_v = a_v$. Given that the prior examples' $K_v \gg K_\lambda$, their diffusive regularization was principally imparted by the trace-like field variable $\tilde{\epsilon}_v^{\mathrm{p}}$. This was key to the successful regularization, unlike the below examples.

Instead consider the converse scenario: micromorphic stiffness K_v goes to a small value; consequently the trace field variable $\tilde{\epsilon}_v^{\mathrm{p}}$ exerts negligible effect; and, direct regularization of the plastic hardening is effectively discontinued. Specifically, all other parameters are held equal, $\tilde{\epsilon}_v^{\mathrm{p}}$'s micromorphic stiffness is dropped to $K_v = a_v \times 10^{-10}$. Given that $k_v = K_v \approx 0$ MPa, the volumetric penalty term remains small in Eq. (13), even for large differences between local internal variable ϵ_v and field variable $\tilde{\epsilon}_v^{\mathrm{p}}$. Thus, the model does not exhibit significant size effect (see Fig. 23).

In this first scenario, the numerical boundary value problems exhibit instability. Fig. 21(a–c) depicts this phenomenon, which is measured in Fig. 22(d): conditionally, based upon the microstructural angle θ_I, in that most simulations in Fig. 21 fail to converge through localized softening. In the same vein in Fig. 22(b), oscillatory equivalent plastic strain λ profiles correspond to the non-convergent cases, evidencing divergence upon localization. Hence, for practical purposes, diminishing K_v stymies the appearance of regularized shear band-like strain localization phenomena.

Alternatively, under-weighting the trace-like $\tilde{\epsilon}_v^{\mathrm{p}}$ may inhibit strain localization. Specifically, shear bands are also stifled by the ultimate parameterization: the coefficients applied to compute the micromorphic stiffness are reversed. Instead of setting $K_\lambda = a_\lambda \times 10^{-2}$ and $K_v = a_v$ as in Fig. 5, we set $K_\lambda = a_\lambda$ and $K_v = a_v \times 10^{-2}$ in Fig. 24. Due to this change, the shear bands are suppressed for all microstructural angles θ_I.

In this second scenario, the relative weight attributed to the nonlocal plastic volumetric deformation reduces. Remember that, given that normalized diffusive length $\tilde{l}_\lambda = \tilde{l}_v$, equivalent spatial averaging for both $\tilde{\lambda}$ and $\tilde{\epsilon}_v^{\mathrm{p}}$ is effectuated by the regularizing Helmholtz equations. Furthermore, by dint of Eq. (14), we set the baseline stiffnesses $a_\lambda = a_v$. Thus, a bolstered $\tilde{\lambda}$-penalty energy suppresses shear bands per Fig. 24, even though deviatoric and volumetric deformation couples through $\boldsymbol{B}_\lambda$. Conversely as the trace-related micromorphic stiffness K_v increases, strain successfully localizes like in the initial examples (i.e. Fig. 5). We summarize the different regularization parameterizations in Table 2.

6.2. 3D triaxial compression

For the 3D simulations, local elastoplastic material parameters are identical to those in the 2D plane strain cases with OCR = 30. Micromorphic stiffness are identically obtained via Eq. (14). The boundary value problem's

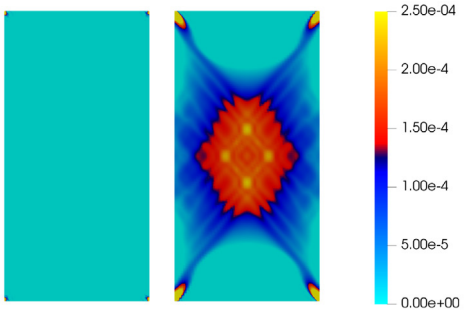

(a) Local elastoplastic isotropy case does not run to completion, at $u_2 = -0.4,\ -0.505 \times 10^{-3}$ mm.

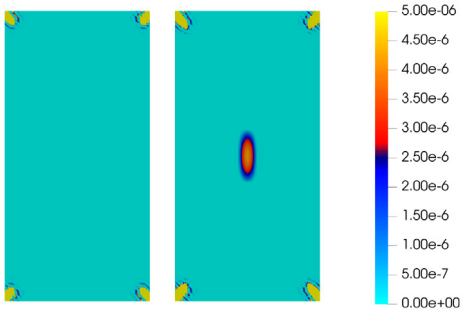

(b) Local anisotropy with microstructural angle $\theta_l = 0$ case does not run to completion, at $u_2 = -0.3,\ -0.315 \times 10^{-3}$ mm.

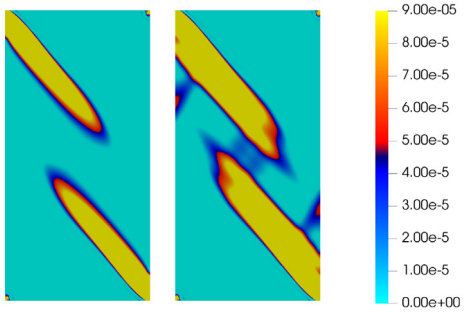

(c) Local anisotropy with microstructural angle $\theta_l = \pi/4$ case does not run to completion, at $u_2 = -0.4,\ -0.405 \times 10^{-3}$ mm.

Fig. 21. Equivalent plastic strain λ for plane strain compression isotropic case vs. anisotropic cases with OCR $= 30$ and rotation of microstructural direction, but with lowered micromorphic stiffness $K_v = a_v \times 10^{-10} \approx 0$ MPa.

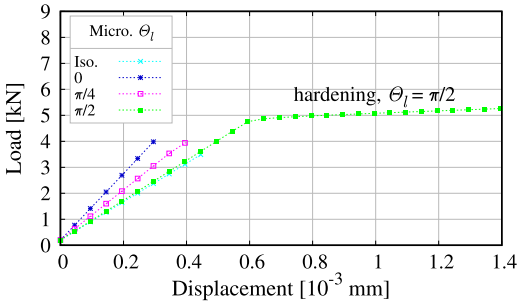

(a) Force-displacement curves, indicating only the anisotropic macroscopic hardening case with microstructural angle $\theta_l = \pi/2$ completes.

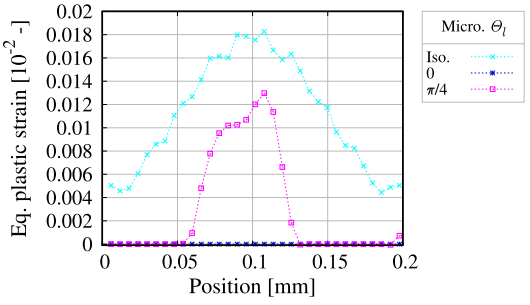

(b) Profiles of equivalent plastic strain λ, for boundary displacements u_2 at failure indicated in captions to Fig. 21.

Fig. 22. Plane strain compression case comparing local isotropy and anisotropy with micromorphic stiffness $K_v \approx 0$ MPa, showing: (a) vertical force vs. vertical displacement curves; and, (b) profiles of equivalent plastic strain λ across transect indicated as a dashed line in Fig. 4(a) (LA-MI).

geometry is enlarged and 3D, Fig. 25(a). The geometry's dimensions approximate the inch-scale used for triaxial test specimens of common rocks [71,72]. Compressive confining stress $\sigma_c = -1$ MPa is applied on the lateral boundary. The loading increment along the displacement-controlled boundary is $\Delta u_3 = 5.0 \times 10^{-4}$ mm downwards, which

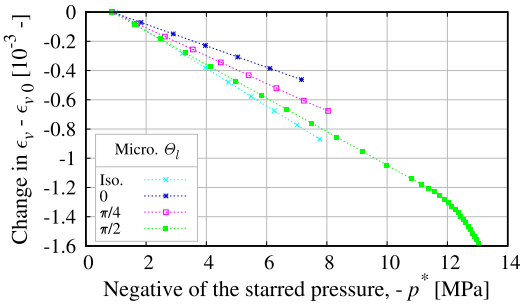

(a) Body-averaged state path, indicating only the anisotropic case with microstructural angle $\theta_l = \pi/2$ completes.

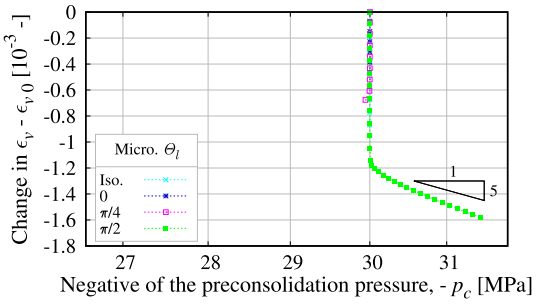

(b) Semilog plot evidencing fair recovery for the harding case of the slope $-(C_d) \times 10^3$, with all softening cases failing to complete.

Fig. 23. Plane strain compression case comparing local isotropy and anisotropy with micromorphic stiffness $K_v \approx 0$ MPa, globally averaged material state curves, showing: (a) and (b), loading paths for change in ϵ_v, such that loading paths begin at 0 in the ordinate axis. Neither the isotropic case nor the anisotropic cases with microstructural angles $\theta_l = 0, \pi/4$ run to completion (LA-MI).

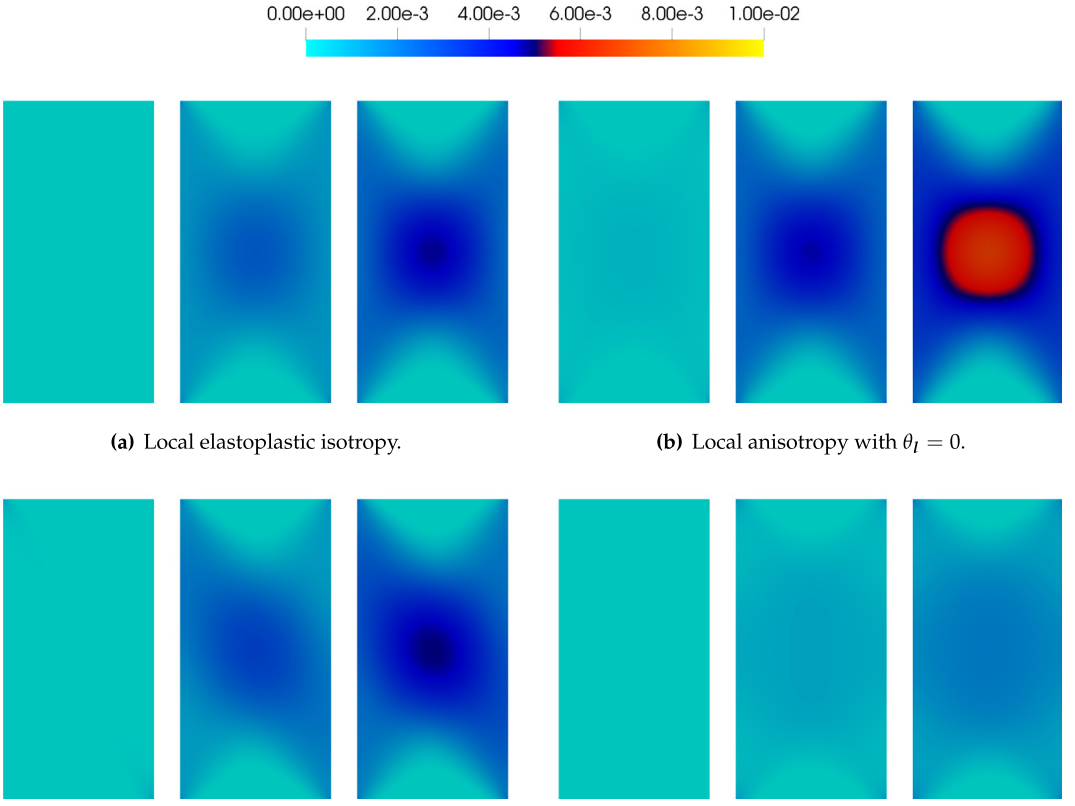

(a) Local elastoplastic isotropy.

(b) Local anisotropy with $\theta_l = 0$.

(c) Local anisotropy with $\theta_l = \pi/4$.

(d) Local anisotropy with $\theta_l = \pi/2$.

Fig. 24. Equivalent plastic strain λ for plane strain compression isotropic case vs. anisotropic cases with OCR = 30 and rotation of microstructural direction, but with reversed nonlocal stiffnesses $K_\lambda = a_\lambda$ and $K_v = a_v \times 10^{-2}$, at $u_2 = -0.4,\ -0.8,\ -1.0 \times 10^{-3}$ mm (LA-MI).

has been scaled w.r.t. the problem dimensions from the 2D cases. The displacements are fixed at zero along the bottom surface.

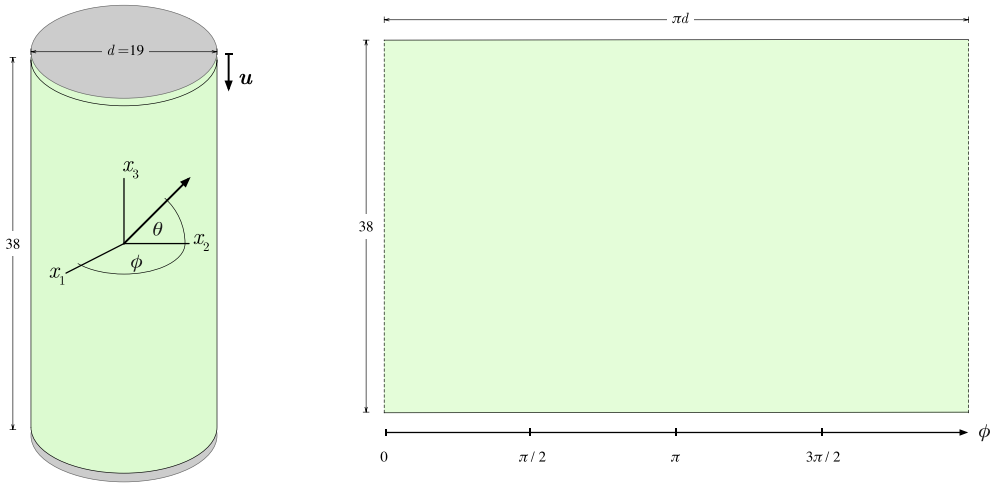

(a) Setup of the boundary value problem, with normal confining stress σ_c applied along lateral boundary.

(b) Unrolled view of lateral boundary surface with dimensions, enfranchised because the principal and hence Gaussian curvatures on the cylinder's lateral surface are zero, a standard result.

Fig. 25. Geometry of the numerical specimen for 3D plasticity simulations, showing: (a) Euler angles θ and ϕ, for the axis origin located at the centroid of the cylinder; and, (b) unrolled lateral surface parameterized by ϕ, in the manner of Tien et al. [70].

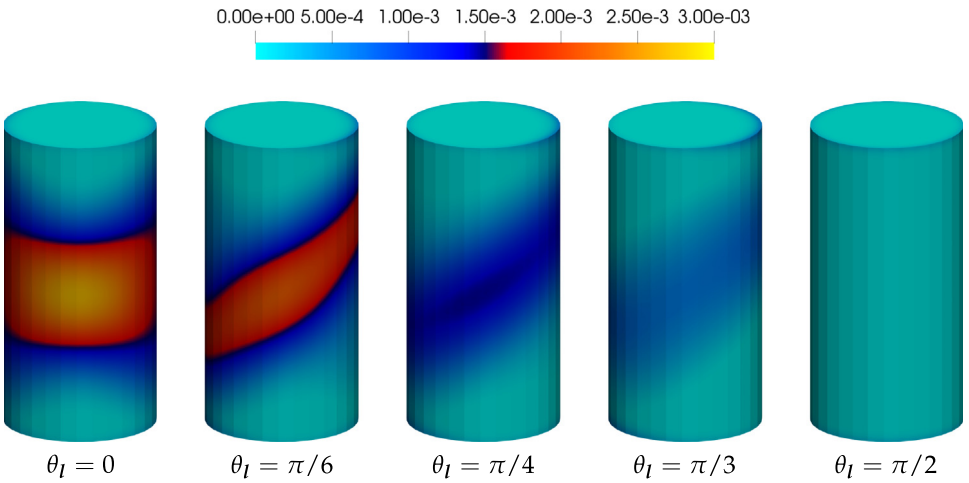

Fig. 26. Micromorphic equivalent plastic strain variable $\tilde{\lambda}$ for 3D compression anisotropic cases with OCR = 30, inducing local anisotropy by setting $E = 2400$ MPa and $\beta^{\text{dev}} = \beta^{\text{vol}} = 0.8$, at $u_3 = 0.05$ mm downwards (LA-MI).

Table 2
Micromorphic regularization stiffness and convergence summary.

$\tilde{l}_\lambda$ [mm]	a_λ [MPa]	k_λ [MPa]	K_λ [MPa]	k_v [MPa]	K_v [MPa]	Softening	Localization
$\tilde{l}_v$	a_v	$a_\lambda \times 10^{-2}$	$a_\lambda \times 10^{-2}$	a_v	a_v	Stable	Yes
$\tilde{l}_v$	a_v	a_λ	a_λ	$a_v \times 10^{-2}$	$a_v \times 10^{-2}$	Stable	No
$\tilde{l}_v$	a_v	$a_\lambda \times 10^{-2}$	$a_\lambda \times 10^{-2}$	≈ 0	≈ 0	Unstable	–

Numerical parameters are as follows. The baseline diffusive lengths are $\tilde{l}_\lambda = \tilde{l}_v = 0.5$ mm, approximating the sub-microscale length of composite deformation behavior, identified for layered, bedded sedimentary rock with clay

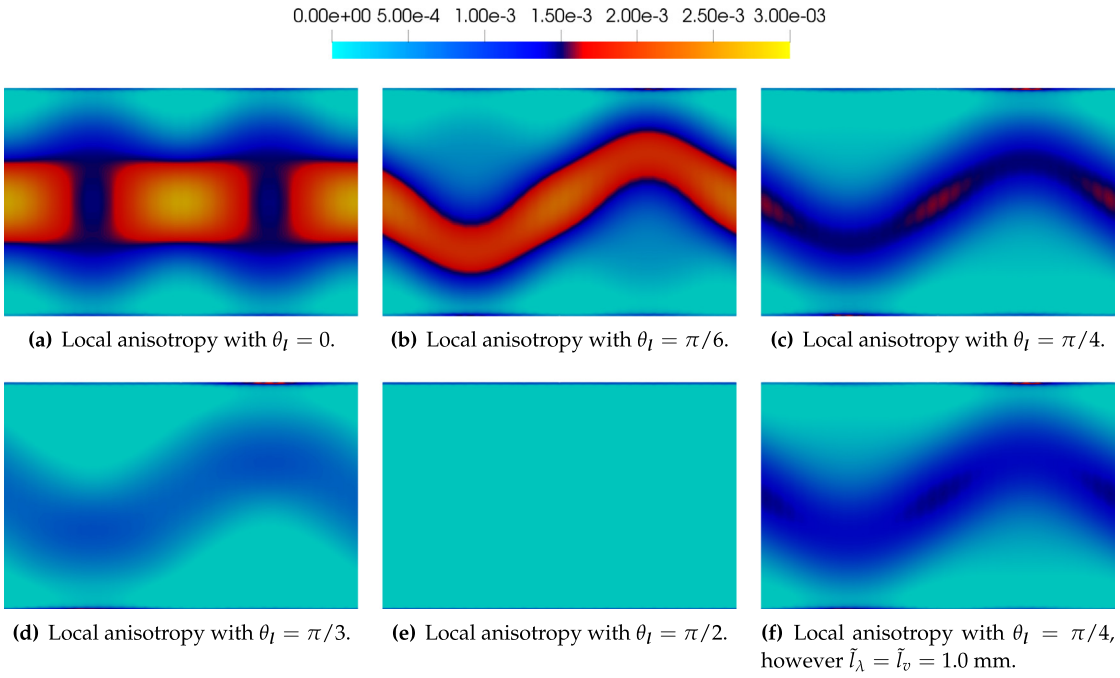

(a) Local anisotropy with $\theta_l = 0$. **(b)** Local anisotropy with $\theta_l = \pi/6$. **(c)** Local anisotropy with $\theta_l = \pi/4$.

(d) Local anisotropy with $\theta_l = \pi/3$. **(e)** Local anisotropy with $\theta_l = \pi/2$. **(f)** Local anisotropy with $\theta_l = \pi/4$, however $\tilde{l}_\lambda = \tilde{l}_v = 1.0$ mm.

Fig. 27. Equivalent plastic strain λ for 3D compression anisotropic cases with OCR = 30 and rotation of microstructural direction, inducing local anisotropy by setting $E = 2400$ MPa and $\beta^{\text{dev}} = \beta^{\text{vol}} = 0.8$, at $u_3 = 0.05$ mm downwards. Unrolled view of the lateral surface is explained by Fig. 25(b) and is in the manner of Tien et al. [70] (LA-MI).

matrix in [73]. Interpreting the mesh-independent convergence of the 2D boundary force–displacement curves and global state paths, the maximum characteristic element length $h = 0.5\ \tilde{l}_\lambda < 0.7\ \tilde{l}_\lambda$. As such, we import an initial unstructured mesh containing $n_0 = 1539$ elements. Each additional level of refinement l_h equally partitions every cell at the previous level of refinement into eight cells (in 3D). The refined mesh contains $n_0 \times 8^{l_h} = 787968$ cells for $l_h = 3$, requiring computations distributed over 24 processors.

Parameterizing θ_l normalizes $\boldsymbol{l} \sim [0, 1, \tan(\theta_l)]$, restricting $\boldsymbol{l} \cdot \boldsymbol{l} = 1$. Results are presented in Figs. 26–28. As anticipated, for $\theta_l = 0$, the result is periodic in ϕ with period π. Symmetric shear bands develop about axis $\theta = 0$. For $0 < \theta_l < \pi/2$ in contrast, the strain localization is antisymmetric about axis $\gamma = \pi$, i.e. the unrolled surface's centerline.

In comparison to the 2D results, two tends are most notable. First, onset of the plastic response is primarily dominated by the local elastic anisotropy, Fig. 29. Second, because the plane strain constraint is relaxed, we observe strain localization for all Euler angles θ_l parameterizing the local microstructural direction. This is obvious in the body-averaged state paths, Fig. 30(a).

Doubling the micromorphic length scales $\tilde{l}_\lambda = \tilde{l}_v$ elicits the anticipated result. Regardless of the centerline and width of diffuse plastic zone occurring prior to localization are unaffected. As deformation localizes, however, the micromorphic length scale becomes important: compare Fig. 27(c) to (f). For the baseline case, a thin sinusoidal internal structure is apparent (in the unrolled view), but disappears for the doubled micromorphic length-scale. Yet the antisymmetric and eventual symmetric band's concentrated profile only minorly enhances the specimens' overall compliance, Fig. 30(b).

7. Conclusion

We introduce a mathematical framework that captures the distinctive anisotropies induced at local and mesoscopic scales. The local anisotropy is replicated via an operator that maps the physical anisotropic responses to a fictitious isotropic space, such that the yield function can be a function of invariants in the fictitious space. Meanwhile, the mesoscale anisotropy is induced by a gradient-regularization mechanism that is inherently anisotropic. Using a

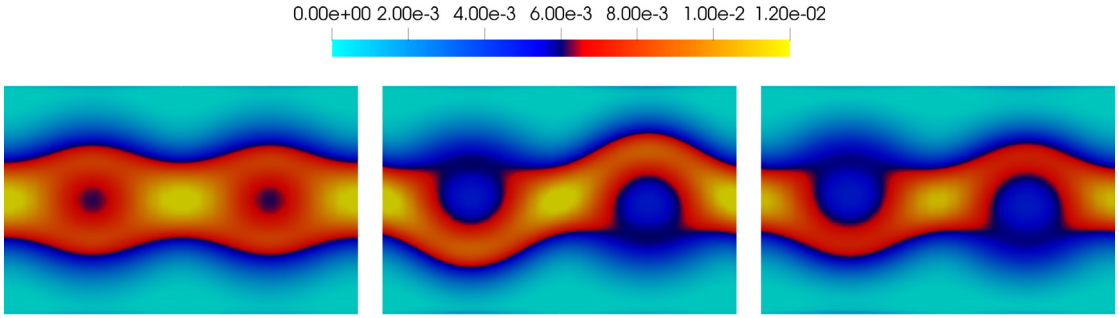

(a) Local anisotropy with $\theta_l = 0$. **(b)** Local anisotropy with $\theta_l = \pi/6$. **(c)** Local anisotropy with $\theta_l = \pi/4$.

(d) Local anisotropy with $\theta_l = \pi/3$. **(e)** Local anisotropy with $\theta_l = \pi/2$. **(f)** Local anisotropy with $\theta_l = \pi/4$, however $\tilde{l}_\lambda = \tilde{l}_v = 1.0$ mm.

Fig. 28. Equivalent plastic strain λ for 3D compression anisotropic cases with OCR $= 30$ and rotation of microstructural direction, inducing local anisotropy by setting $E = 2400$ MPa and $\beta^{\text{dev}} = \beta^{\text{vol}} = 0.8$, at $u_3 = 0.125$ mm downwards. Unrolled view of the lateral surface is explained by Fig. 25(b) and is in the manner of Tien et al. [70] (LA-MI).

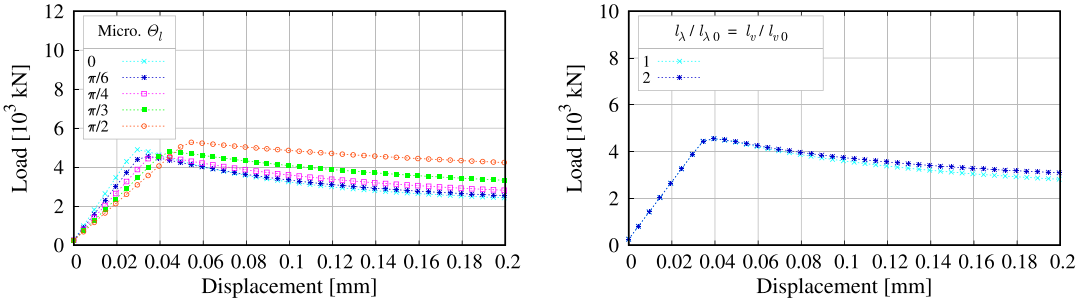

(a) Local anisotropy with rotation of $\boldsymbol{l}$. **(b)** Baseline micromorphic lengths vs. doubled micromorphic lengths.

Fig. 29. D compression case, vertical force vs. vertical displacement curves, showing: (a) anisotropic cases with increasing microstructural angle θ_l; and, (b) anisotropy with $\theta_l = \pi/4$ at two micromorphic regularization lengths (LA-MI).

variational framework that employs penalty between local internal variables and solutions of the modified Helmholtz equations, we introduce relaxation energy functionals and concomitant anisotropic regularization of the projected internal variables. The resultant incremental energy functional yields Euler–Lagrange equations that provide the incremental constitutive update. Important upshots of this local–global penalty approach include: (1) the ease of introducing gradient-dependent flow rules without requiring significant modification in the local return mapping algorithm; (2) allowing the co-existence of different anisotropic features interacting across length scales; (3) enabling mesoscale plastic flow directions not necessarily co-axial to the stress gradient of the yield function, without requiring the introduction of plastic potential; (4) resolving spurious mesh dependency in the softening regimes; (5) imposing no requirement for the identification of plastic zone at each incremental time step. Our numerical simulations performed on homogeneous numerical specimens indicates that the new constitutive law is capable of

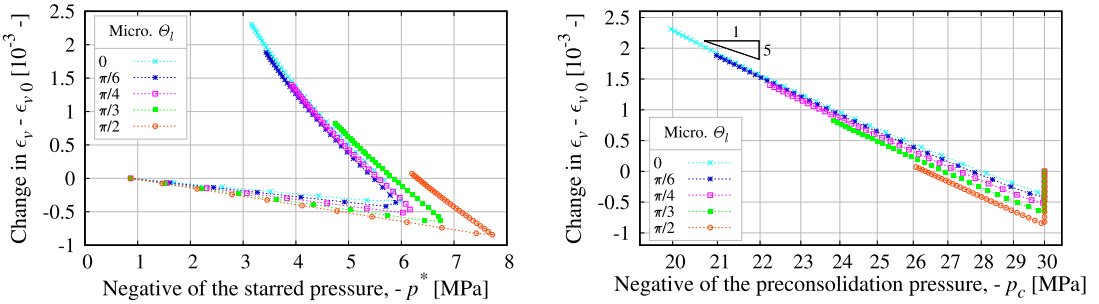

(a) Body-averaged state path, evidencing softening with some localization in all 3D cases.

(b) Semilog plot, evidencing softening with some localization in all 3D cases and fair recovery of the slope $-(C_d) \times 10^3$.

Fig. 30. 3D compression case comparing local anisotropy with increasing microstructural angle θ_l, globally averaged material state curves, showing: (a) and (b), loading paths for change in ϵ_v, such that loading paths begin at 0 in the ordinate axis (LA-MI).

replicating an unusually wide spectrum of complex elastoplastic macroscopic responses. Various types of shear band of different orientations, band width and forms are evidenced, and induced by changing the structural orientations, local material parameters, and the anisotropic regularization. This ability to replicate a diverse responses is a necessary feature for surrogate models or effective media to sufficiently represent complex microstructures whose anisotropic behaviors originated from different features across length scales.

Future work may include the formulation of sequential inverse problems and sensitivity analysis on the material parameters for the micromorphic-enhanced constitutive laws (cf. [74]), the incorporation of multi-physical coupling effects due to heat transfer and pore-fluid diffusion inside the porous materials, and the extension of this mathematical framework in the finite deformation range. In particular, it is likely that an additive kinematic framework that employs the logarithmic strain space in [75] might be used to extend the current model to the finite strain regime while ensuring objectivity. However, as proven recently by Neff and Ghiba [76], a major challenge would be to ensure that the rank-one convexity is preserved during the plastic flow for the additive logarithmic plasticity model with non-coaxial plastic deformation $\boldsymbol{C} \cdot \boldsymbol{C}^{p-1} \neq \boldsymbol{C}^{p-1} \cdot \boldsymbol{C}$. The authors are currently undertaking this challenge and will report the results if sufficient progress have been made.

Acknowledgments

This research is supported by the Earth Materials and Processes program from the US Army Research Office under grant contract W911NF-18-2-0306, the Dynamic Materials and Interactions Program from the Air Force Office of Scientific Research, United States under grant contract FA9550-17-1-0169, the Nuclear Energy University program, United States from the Department of Energy under grant contract DE-NE0008534 as well as the Mechanics of Materials and Structures program at National Science Foundation, United States under grant contract CMMI-1462760. These supports are gratefully acknowledged. The views and conclusions contained in this document are those of the authors, and should not be interpreted as representing the official policies, either expressed or implied, of the sponsors, including the Army Research Laboratory or the U.S. Government. The U.S. Government is authorized to reproduce and distribute reprints for government purposes notwithstanding any copyright notation herein.

Appendix A. Kelvin notation

Kelvin notation is a *reduced* matrix/vector notation: it accounts for symmetry of second- and fourth-order tensors. Thus for symmetric second-order stress tensor $\boldsymbol{\sigma} = \partial W^{\mathrm{e}}/\partial \boldsymbol{\epsilon}^{\mathrm{e}}$ and elastic strain tensor $\boldsymbol{\epsilon}^{\mathrm{e}}$, we compare traditional

Voigt-notated versus Kelvin-notated vector equivalents:

$$\overline{\boldsymbol{\sigma}} = \begin{bmatrix} \overline{\sigma}_1 \\ \overline{\sigma}_2 \\ \overline{\sigma}_3 \\ \overline{\sigma}_4 \\ \overline{\sigma}_5 \\ \overline{\sigma}_6 \end{bmatrix}_{6\times 1} = \underbrace{\begin{bmatrix} \sigma_{11} \\ \sigma_{22} \\ \sigma_{33} \\ \sigma_{23} \\ \sigma_{13} \\ \sigma_{12} \end{bmatrix}_{6\times 1}}_{\text{Voigt}} = \underbrace{\begin{bmatrix} \sigma_{11} \\ \sigma_{22} \\ \sigma_{33} \\ \sqrt{2}\sigma_{23} \\ \sqrt{2}\sigma_{13} \\ \sqrt{2}\sigma_{12} \end{bmatrix}_{6\times 1}}_{\text{Kelvin}}, \quad \overline{\boldsymbol{\epsilon}}^{\mathrm{e}} = \begin{bmatrix} \overline{\epsilon}^{\mathrm{e}}_1 \\ \overline{\epsilon}^{\mathrm{e}}_2 \\ \overline{\epsilon}^{\mathrm{e}}_3 \\ \overline{\epsilon}^{\mathrm{e}}_4 \\ \overline{\epsilon}^{\mathrm{e}}_5 \\ \overline{\epsilon}^{\mathrm{e}}_6 \end{bmatrix}_{6\times 1} = \underbrace{\begin{bmatrix} \epsilon^{\mathrm{e}}_{11} \\ \epsilon^{\mathrm{e}}_{22} \\ \epsilon^{\mathrm{e}}_{33} \\ 2\epsilon^{\mathrm{e}}_{23} \\ 2\epsilon^{\mathrm{e}}_{13} \\ 2\epsilon^{\mathrm{e}}_{12} \end{bmatrix}_{6\times 1}}_{\text{Voigt}} = \underbrace{\begin{bmatrix} \epsilon^{\mathrm{e}}_{11} \\ \epsilon^{\mathrm{e}}_{22} \\ \epsilon^{\mathrm{e}}_{33} \\ \sqrt{2}\epsilon^{\mathrm{e}}_{23} \\ \sqrt{2}\epsilon^{\mathrm{e}}_{13} \\ \sqrt{2}\epsilon^{\mathrm{e}}_{12} \end{bmatrix}_{6\times 1}}_{\text{Kelvin}}. \tag{44}$$

In comparison to Voigt-notated vectors and matrices, Kelvin notation's significant advantage is immediately apparent upon contraction: norms of both second-order tensors like the stress $\boldsymbol{\sigma}$ and fourth-order tensors like the elastic stiffness tensor $\boldsymbol{C}^{\mathrm{e}}$ are preserved, leading to a geometric interpretation of matrix eigenvectors [77]. Nonetheless the strain tensor resolves quadratically as $\boldsymbol{\epsilon}^{\mathrm{e}} : \boldsymbol{C}^{\mathrm{e}} : \boldsymbol{\epsilon}^{\mathrm{e}} = \overline{\boldsymbol{\epsilon}}^{\mathrm{e}\,\mathrm{T}} \mathbf{C}^{\mathrm{e}} \overline{\boldsymbol{\epsilon}}^{\mathrm{e}}$, and so forth. For symmetric fourth-order elastic stiffness tensor $\boldsymbol{C}^{\mathrm{e}}$, the Kelvin-notation matrix equivalent is:

$$\mathbf{C}^{\mathrm{e}} = \underbrace{\begin{bmatrix} C^{\mathrm{e}}_{1111} & C^{\mathrm{e}}_{1122} & C^{\mathrm{e}}_{1133} & \sqrt{2}C^{\mathrm{e}}_{1123} & \sqrt{2}C^{\mathrm{e}}_{1113} & \sqrt{2}C^{\mathrm{e}}_{1112} \\ C^{\mathrm{e}}_{2211} & C^{\mathrm{e}}_{2222} & C^{\mathrm{e}}_{2233} & \sqrt{2}C^{\mathrm{e}}_{2223} & \sqrt{2}C^{\mathrm{e}}_{2213} & \sqrt{2}C^{\mathrm{e}}_{2212} \\ C^{\mathrm{e}}_{3311} & C^{\mathrm{e}}_{3322} & C^{\mathrm{e}}_{3333} & \sqrt{2}C^{\mathrm{e}}_{3323} & \sqrt{2}C^{\mathrm{e}}_{3313} & \sqrt{2}C^{\mathrm{e}}_{3312} \\ \sqrt{2}C^{\mathrm{e}}_{2311} & \sqrt{2}C^{\mathrm{e}}_{2322} & \sqrt{2}C^{\mathrm{e}}_{2333} & 2C^{\mathrm{e}}_{2323} & 2C^{\mathrm{e}}_{2312} & 2C^{\mathrm{e}}_{2312} \\ \sqrt{2}C^{\mathrm{e}}_{1311} & \sqrt{2}C^{\mathrm{e}}_{1322} & \sqrt{2}C^{\mathrm{e}}_{1333} & 2C^{\mathrm{e}}_{1323} & 2C^{\mathrm{e}}_{1313} & 2C^{\mathrm{e}}_{1312} \\ \sqrt{2}C^{\mathrm{e}}_{1211} & \sqrt{2}C^{\mathrm{e}}_{1222} & \sqrt{2}C^{\mathrm{e}}_{1233} & 2C^{\mathrm{e}}_{1223} & 2C^{\mathrm{e}}_{1213} & 2C^{\mathrm{e}}_{1212} \end{bmatrix}_{6\times 6}}_{\text{Kelvin}}. \tag{45}$$

Derivatives are also straightforward. Component-wise for example, we note that $\partial\overline{\boldsymbol{\sigma}}/\partial\overline{\sigma}_4 = [0 \quad 0 \quad 0 \quad 1 \quad 0 \quad 0]^{\mathrm{T}}$.

Finally, we note that the symmetry of second order tensors $\boldsymbol{\sigma}$ and $\boldsymbol{\epsilon}^{\mathrm{e}}$ enables $\overline{\boldsymbol{\sigma}}^{\mathrm{e}}$ and $\overline{\boldsymbol{\epsilon}}^{\mathrm{e}}$ to be six component vectors. Conversely, as $\mathbf{C}^{\mathrm{e}}$ is both symmetric and six-by-six matrix-representable, its fourth-order tensor equivalent $\boldsymbol{C}^{\mathrm{e}}$ exhibits both the major and minor symmetries, respectively. In our study, the elastoplastic tangent matrix $\mathbf{C}^{\mathrm{ep}}$ is also symmetric. As such, its tensor equivalent $\boldsymbol{C}^{\mathrm{ep}}$ similarly combines both the minor and major symmetries, and is hence 'super-symmetric' cf. [32].

Appendix B. Transversely isotropic elasticity

Per [78] for example, E and ν are the Young's modulus and Poisson ratio in the plane of isotropy and characterizing transverse contraction in the plane of isotropy due to tension applied in the perpendicular direction within the plane of isotropy, respectively. E_I and ν_I are the Young's modulus and Poisson ratio in the isotropic plane's normal direction and characterizing transverse contraction in the plane of isotropy due to tension applied in the isotropic plane's normal direction, respectively. In lieu of data, the shear modulus μ_I can be estimated Saint-Venant's formula [24,79]:

$$\frac{1}{\mu_I} \approx \frac{1}{E} + \frac{1}{E_I} + 2\frac{\nu_I}{E_I}. \tag{46}$$

Extracting c_1 through c_5 is then a series of purely algebraic steps. This begins with computing the compliance moduli (with unspecified rotation of material-to-global coordinate systems, assuming local x_3 is the out-of-isotropic-plane direction), see [78]:

$$S^{\mathrm{e}}_{11} = S^{\mathrm{e}}_{22} = \frac{1}{E}, \quad S^{\mathrm{e}}_{12} = -\frac{\nu}{E}, \quad S^{\mathrm{e}}_{13} = S^{\mathrm{e}}_{23} = -\frac{\nu_I}{E_I}, \quad S^{\mathrm{e}}_{33} = \frac{1}{E_I}, \quad S^{\mathrm{e}}_{44} = S^{\mathrm{e}}_{55} = \frac{1}{2\mu_I}, \quad S^{\mathrm{e}}_{66} = S^{\mathrm{e}}_{11} - S^{\mathrm{e}}_{12}.$$

For $1/C^{\mathrm{e}} = S^{\mathrm{e}}_{11} + S^{\mathrm{e}}_{12} - 2\left(S^{\mathrm{e}}_{13}\right)^2/S^{\mathrm{e}}_{33}$, the matrix-stiffness moduli are determined as:

$$C^{\mathrm{e}}_{11} = \frac{S^{\mathrm{e}}_{11} - \left(S^{\mathrm{e}}_{13}\right)^2/S^{\mathrm{e}}_{33}}{S^{\mathrm{e}}_{11} - S^{\mathrm{e}}_{12}} C^{\mathrm{e}}, \quad C^{\mathrm{e}}_{12} = -\frac{S^{\mathrm{e}}_{12} - \left(S^{\mathrm{e}}_{13}\right)^2/S^{\mathrm{e}}_{33}}{S^{\mathrm{e}}_{11} - S^{\mathrm{e}}_{12}} C^{\mathrm{e}},$$

$$C^{\mathrm{e}}_{13} = -\frac{S^{\mathrm{e}}_{13}}{S^{\mathrm{e}}_{33}}C^{\mathrm{e}}, \quad C^{\mathrm{e}}_{33} = \frac{S^{\mathrm{e}}_{11}+S^{\mathrm{e}}_{12}}{E_{\boldsymbol{l}}}C^{\mathrm{e}}, \quad C^{\mathrm{e}}_{44} = \frac{1}{S^{\mathrm{e}}_{44}}, \quad C^{\mathrm{e}}_{66} = \frac{1}{S^{\mathrm{e}}_{66}}.$$

Then the coefficients c_1 through c_6 are dimensioned Walpole-algebra coefficients [34]. In terms of $\mathbf{C}^{\mathrm{e}}$'s matrix-entries in Eq. (45), the Walpole coefficients are:

$$c_1 = C^{\mathrm{e}}_{33}, \quad c_2 = C^{\mathrm{e}}_{11} + C^{\mathrm{e}}_{12}, \quad c_3 = c_4 = \sqrt{2}C^{\mathrm{e}}_{13}, \quad c_5 = C^{\mathrm{e}}_{66}, \quad c_6 = C^{\mathrm{e}}_{44}. \tag{47}$$

By way of comparison between Kelvin and Voigt matrix–vector notations, the Voigt-notated expressions for the entries in the upper right-hand block of the compliance and stiffness matrices are identical with the Kelvin-notated expressions in [78]. Conversely for example, $S^{\mathrm{e}}_{44}\ldots S^{\mathrm{e}}_{66}$ and $C^{\mathrm{e}}_{44}\ldots C^{\mathrm{e}}_{66}$ differ because expressed in Kelvin notation. In particular for example, in Voigt notation $S^{\mathrm{e}}_{44} = S^{\mathrm{e}}_{55} = 1/\mu_{\boldsymbol{l}}$.

To construct $\boldsymbol{C}^{\mathrm{e}}$ per Eq. (6), all required fourth-order tensors are built as follows. First one obtains the microstructural tensors $\boldsymbol{\phi} = \boldsymbol{l}\otimes\boldsymbol{l}$ orthogonal to $\boldsymbol{\chi} = \mathbf{1} - \boldsymbol{l}\otimes\boldsymbol{l}$, with both idempotent. From these two second-order tensors, all the relevant fourth-order tensors are:

$$(\boldsymbol{E}_1)_{ijkl} = \phi_{ij}\phi_{kl}, \quad (\boldsymbol{E}_2)_{ijkl} = \frac{1}{2}\chi_{ij}\chi_{kl}, \quad (\boldsymbol{E}_3)_{ijkl} = \frac{1}{\sqrt{2}}\phi_{ij}\chi_{kl}, \quad (\boldsymbol{E}_4)_{ijkl} = \frac{1}{\sqrt{2}}\chi_{ij}\phi_{kl},$$
$$(\boldsymbol{F})_{ijkl} = \frac{1}{2}(\chi_{ik}\chi_{jl} + \chi_{il}\chi_{jk} - \chi_{ij}\chi_{kl}), \quad (\boldsymbol{G})_{ijkl} = \frac{1}{2}(\phi_{ik}\chi_{jl} + \phi_{il}\chi_{jk} + \chi_{ik}\phi_{jl} + \chi_{il}\phi_{jk}).$$

Since $\boldsymbol{E}_1$, $\boldsymbol{E}_2$, $\boldsymbol{F}$, and $\boldsymbol{G}$ each exhibits major symmetry, so does their every combination. I.e. G_{ijkl} contains $\phi_{ik}\chi_{jl}$ but also $\chi_{ik}\phi_{jl}$ to the same coefficient. Secondly they express minor symmetry, which is identifiable by applying the symmetry of $\boldsymbol{\phi}$ and $\boldsymbol{\chi}$. Thus their every combination qualifies as super-symmetric. In contrast, $\boldsymbol{E}_3$ and $\boldsymbol{E}_4$ are not super-symmetric. However as we constrain their coefficients such that $c_3 = c_4$, their every permissible combination exhibits the major symmetry [34].

Appendix C. Transversely isotropic plasticity

Semnani et al. [8] previously introduced a transversely isotropic plastic mapping tensor. This linear mapping can be represented by a super-symmetric fourth-order tensor, described by microstructural direction $\boldsymbol{l}$ and the coefficients α, β, and γ. To construct $\boldsymbol{P}^{\mathrm{p}}$ per Eq. (9), all required fourth-order tensors are built as follows.

$$(\boldsymbol{P}^{\mathrm{p}}_1)_{ijkl} = \frac{1}{2}\left(\delta_{ik}\delta_{jl} + \delta_{il}\delta_{jk}\right), \quad (\boldsymbol{P}^{\mathrm{p}}_2)_{ijkl} = \frac{1}{2}\left(\phi_{ik}\phi_{jl} + \phi_{il}\phi_{jk}\right),$$
$$(\boldsymbol{P}^{\mathrm{p}}_3)_{ijkl} = \frac{1}{4}\left(\delta_{ik}\phi_{jl} + \delta_{il}\phi_{jk} + \phi_{ik}\delta_{jl} + \phi_{il}\delta_{jk}\right),$$

Formally tensor $\boldsymbol{P}^{\mathrm{p}}$ is a mapping, as lacking idempotence in that $\boldsymbol{P}^{\mathrm{p}} \neq \boldsymbol{P}^{\mathrm{p}} : \boldsymbol{P}^{\mathrm{p}}$, see Section 2.4.1 in [45]. It is easy to show that, in terms of the Walpole algebra, Eq. (9) is

$$\boldsymbol{P}^{\mathrm{p}} = \alpha\boldsymbol{E}_1 + \beta(\boldsymbol{E}_2 + \boldsymbol{F}) + \gamma\boldsymbol{G}.$$

Alternately, also within the stress-space, the Walpole algebra contains an isotropic-to-transversely-isotropic stress-space mapping. Practically, this alternative mapping adds an additional coefficient δ to the mapping. The combination of tensors forming the basis for this mapping,

$$\alpha\boldsymbol{E}_1 + \beta\boldsymbol{E}_2 + \gamma\boldsymbol{F} + \delta\boldsymbol{G},$$

are derived as the symmetric (linearly independent) elements within the symmetric commutative Walpole subalgebra [80]. Each element within the subalgebra is idempotent, hence qualifies a projection in Kunin's terms. For all coefficients $\alpha\ldots\gamma$ equal to 1, these elements sum to the symmetric fourth-order identity tensor. Our notion extends naturally to additional material symmetries, wherein the mapping's basis remains the linearly independent elements summing to $\boldsymbol{I}$.

C.1. Local residual, tangent, and initialization

To derive the local residual $\bar{\mathbf{r}}$, we apply the chain rule to the stationary condition of optimality defining the local Euler–Lagrange equation. Minimizing over the elastic strain,

$$\frac{\delta W(\boldsymbol{\zeta}_{n+1})}{\delta\boldsymbol{\epsilon}^{\mathrm{e}}_{n+1}} = \frac{\partial W(\boldsymbol{\zeta}_{n+1})}{\partial\boldsymbol{\epsilon}^{\mathrm{e}}_{n+1}} = \frac{\partial W(\boldsymbol{\zeta}_{n+1})}{\partial\Delta\boldsymbol{\epsilon}^{\mathrm{p}}} : \frac{\partial\Delta\boldsymbol{\epsilon}^{\mathrm{p}}}{\partial\boldsymbol{\epsilon}^{\mathrm{e}}} = \mathbf{0}.$$

Expanding the above,

$$\begin{aligned}\frac{\partial W(\boldsymbol{\zeta}_{n+1})}{\partial \Delta\boldsymbol{\epsilon}^{\mathrm{p}}} : \frac{\partial \Delta\boldsymbol{\epsilon}^{\mathrm{p}}}{\partial \boldsymbol{\epsilon}^{\mathrm{e}}} &= \Bigg(\frac{\partial W^{\mathrm{e}}_{n+1}}{\partial \boldsymbol{\epsilon}^{\mathrm{e}}_{n+1}} : \frac{\partial \boldsymbol{\epsilon}^{\mathrm{e}}_{n+1}}{\partial \Delta\boldsymbol{\epsilon}^{\mathrm{p}}} + \overbrace{\frac{\partial W^{\mathrm{p}}_{\boldsymbol{\alpha}\,n+1}}{\partial \lambda_{n+1}} \frac{\partial \lambda_{n+1}}{\partial \Delta\lambda}}^{\partial W^{\mathrm{p}}_{\boldsymbol{\alpha}\,n+1}/\partial \Delta\lambda} \frac{\partial \Delta\lambda}{\partial \Delta\boldsymbol{\epsilon}^{\mathrm{p}}} + \frac{\partial W^{\mathrm{p}}_{\boldsymbol{\alpha}\,n+1}}{\partial \epsilon^{\mathrm{p}}_{v\,n+1}} \frac{\partial \epsilon^{\mathrm{p}}_{v\,n+1}}{\partial \Delta\epsilon^{\mathrm{p}}_{v}} \frac{\partial \Delta\epsilon^{\mathrm{p}}_{v}}{\partial \Delta\boldsymbol{\epsilon}^{\mathrm{p}}} \\ &\quad + \frac{\partial W^{\mathrm{p}}_{\lambda,n+1}}{\partial \lambda_{n+1}} \frac{\partial \lambda_{n+1}}{\partial \Delta\lambda} \frac{\partial \Delta\lambda}{\partial \Delta\boldsymbol{\epsilon}^{\mathrm{p}}} + \frac{\partial W^{\mathrm{p}}_{v\,n+1}}{\partial \epsilon^{\mathrm{p}}_{v\,n+1}} \frac{\partial \epsilon^{\mathrm{p}}_{v\,n+1}}{\partial \Delta\epsilon^{\mathrm{p}}_{v}} \frac{\partial \Delta\epsilon^{\mathrm{p}}_{v}}{\partial \Delta\boldsymbol{\epsilon}^{\mathrm{p}}} \Bigg) : \frac{\partial \Delta\boldsymbol{\epsilon}^{\mathrm{p}}}{\partial \boldsymbol{\epsilon}^{\mathrm{e}}_{n+1}} \\ &= \Bigg[\boldsymbol{\sigma}_{n+1} : (-\boldsymbol{I}) + \sigma_{q\,n+1} \frac{\partial \Delta\lambda}{\partial \Delta\boldsymbol{\epsilon}^{\mathrm{p}}} + \sigma_{p\,n+1} \boldsymbol{b}_v - k_\lambda \Big(\tilde{\lambda}_{n+1} - \lambda_{n+1} \Big) \frac{\partial \Delta\lambda}{\partial \Delta\boldsymbol{\epsilon}^{\mathrm{p}}} \\ &\quad - k_v \Big(\tilde{\epsilon}^{\mathrm{p}}_{v\,n+1} - \epsilon^{\mathrm{p}}_{v\,n+1} \Big) \boldsymbol{b}_v \Bigg] : (-\boldsymbol{I}) \,.\end{aligned}$$

After some auxiliary simplification, we obtain the residual $\bar{\mathbf{r}}$ associated with Eq. (26).

To derive the tangent $\partial \bar{\mathbf{r}} / \partial \bar{\mathbf{x}}$, we separately consider the purely local vs. the micromorphic terms in the derivatives of $W(\boldsymbol{\zeta}_{n+1})$. First, let us consider the purely local term

$$\begin{aligned}\frac{\partial^2 \left(W^{\mathrm{e}}_{n+1} + W^{\mathrm{p}}_{\boldsymbol{\alpha}\,n+1} \right)}{\partial \boldsymbol{\epsilon}^{\mathrm{e}}_{n+1} \otimes \partial \boldsymbol{\epsilon}^{\mathrm{e}}_{n+1}} &= \boldsymbol{C}^{\mathrm{e}} - \Bigg[\frac{\sigma_{q\,n+1}}{\Delta\lambda} \boldsymbol{B}_\lambda + \frac{\partial}{\partial \sigma_{q\,n+1}} \left(\frac{\partial W^{\mathrm{p}}_{\boldsymbol{\alpha}\,n+1}}{\partial \boldsymbol{\epsilon}^{\mathrm{e}}_{n+1}} \right) \otimes \frac{\partial \sigma_{q\,n+1}}{\partial \Delta\boldsymbol{\epsilon}^{\mathrm{p}}} + \frac{\partial}{\partial \Delta\lambda} \left(\frac{\partial W^{\mathrm{p}}_{\boldsymbol{\alpha}\,n+1}}{\partial \boldsymbol{\epsilon}^{\mathrm{e}}_{n+1}} \right) \otimes \frac{\partial \Delta\lambda}{\partial \Delta\boldsymbol{\epsilon}^{\mathrm{p}}} \\ &\quad + \frac{\partial}{\partial \sigma_{p\,n+1}} \left(\frac{\partial W^{\mathrm{p}}_{\boldsymbol{\alpha}\,n+1}}{\partial \boldsymbol{\epsilon}^{\mathrm{e}}_{n+1}} \right) \otimes \frac{\partial \sigma_{p\,n+1}}{\partial \Delta\boldsymbol{\epsilon}^{\mathrm{p}}} \Bigg] : \frac{\partial \Delta\boldsymbol{\epsilon}^{\mathrm{p}}}{\partial \boldsymbol{\epsilon}^{\mathrm{e}}_{n+1}},\end{aligned}$$

where

$$\begin{aligned}\frac{\partial}{\partial \sigma_{q\,n+1}} \left(\frac{\partial W^{\mathrm{p}}_{\boldsymbol{\alpha}\,n+1}}{\partial \boldsymbol{\epsilon}^{\mathrm{e}}_{n+1}} \right) \otimes \frac{\partial \sigma_{q\,n+1}}{\partial \Delta\boldsymbol{\epsilon}^{\mathrm{p}}} &= \left(\frac{\boldsymbol{B}_\lambda : \Delta\boldsymbol{\epsilon}^{\mathrm{p}}}{\Delta\lambda} \right) \otimes \left[-\frac{M}{2} \left(\partial_{\epsilon^{\mathrm{p}}_v} p_{c\,n+1} \boldsymbol{b}_v \right) \right], \\ \frac{\partial}{\partial \Delta\lambda} \left(\frac{\partial W^{\mathrm{p}}_{\boldsymbol{\alpha}\,n+1}}{\partial \boldsymbol{\epsilon}^{\mathrm{e}}_{n+1}} \right) \otimes \frac{\partial \Delta\lambda}{\partial \Delta\boldsymbol{\epsilon}^{\mathrm{p}}} &= -\left(\frac{\sigma_{q\,n+1}}{\Delta\lambda^2} \boldsymbol{B}_\lambda : \Delta\boldsymbol{\epsilon}^{\mathrm{p}} \right) \otimes \left(\frac{\boldsymbol{B}_\lambda : \Delta\boldsymbol{\epsilon}^{\mathrm{p}}}{\Delta\lambda} \right), \\ \frac{\partial}{\partial \sigma_{p\,n+1}} \left(\frac{\partial W^{\mathrm{p}}_{\boldsymbol{\alpha}\,n+1}}{\partial \boldsymbol{\epsilon}^{\mathrm{e}}_{n+1}} \right) \otimes \frac{\partial \sigma_{p\,n+1}}{\partial \Delta\boldsymbol{\epsilon}^{\mathrm{p}}} &= \boldsymbol{b}_v \otimes \frac{1}{2} \left[\partial_{\epsilon^{\mathrm{p}}_v} p_{c\,n+1} \left(\boldsymbol{b}_v - M \frac{\boldsymbol{B}_\lambda : \Delta\boldsymbol{\epsilon}^{\mathrm{p}}}{\Delta\lambda} \right) - M \Delta\lambda \partial^2_{\epsilon^{\mathrm{p}}_v \epsilon^{\mathrm{p}}_v} p_{c\,n+1} \boldsymbol{b}_v \right],\end{aligned}$$

of which the first and last terms combine to produce symmetry. Second, consider the micromorphic terms

$$\begin{aligned}\frac{\partial^2 W^{\mathrm{p}}_{\tilde{\boldsymbol{\alpha}}\,n+1}}{\partial \boldsymbol{\epsilon}^{\mathrm{e}}_{n+1} \otimes \partial \boldsymbol{\epsilon}^{\mathrm{e}}_{n+1}} &= -k_\lambda \left(\tilde{\lambda}_{n+1} - \lambda_{n+1} \right) \frac{\partial}{\partial \Delta\boldsymbol{\epsilon}^{\mathrm{p}}} \left(\frac{\boldsymbol{B}_\lambda : \Delta\boldsymbol{\epsilon}^{\mathrm{p}}}{\Delta\lambda} \right) + k_\lambda \left(\boldsymbol{B}_\lambda : \boldsymbol{n}_{n+1} \right) \otimes \left(\boldsymbol{B}_\lambda : \boldsymbol{n}_{n+1} \right) \\ &\quad + k_v \boldsymbol{b}_v \otimes \boldsymbol{b}_v,\end{aligned}$$

where

$$\frac{\partial}{\partial \Delta\boldsymbol{\epsilon}^{\mathrm{p}}} \left(\frac{\boldsymbol{B}_\lambda : \Delta\boldsymbol{\epsilon}^{\mathrm{p}}}{\Delta\lambda} \right) = \frac{1}{\Delta\lambda} \left[\boldsymbol{B}_\lambda - \left(\boldsymbol{B}_\lambda : \boldsymbol{n}_{n+1} \right) \otimes \left(\boldsymbol{B}_\lambda : \boldsymbol{n}_{n+1} \right) \right].$$

Summing the purely local term and the micromorphic terms, we obtain the tangent $\partial \bar{\mathbf{r}} / \partial \bar{\mathbf{x}}$.

Appendix D. Initialization

The mapped invariant-dependent flow rule of Eq. (30) is useful on occasion. For instance, even when the simulated specimen is normally consolidated, it oftentimes clarifies interpretation to begin simulations at: zero displacement, zero plastic strain, and zero field $\tilde{\lambda}$ and $\tilde{\epsilon}^{\mathrm{p}}_v$. In this instance, it suffices to initialize $\epsilon^{\mathrm{p}}_{v\,0} = 0$ and $p_{c\,0}$ as follows. Specify a minimum input preconsolidation pressure $p_{c\,0}$. For any given in situ stress tensor $\boldsymbol{\sigma}_0$ at time zero, $\Delta\lambda = 0$ so Eq. (31) becomes

$$p^*_0 \Big(p^*_0 - p_{c\,0} \Big) + \frac{q^{*\,2}_0}{M^{\,2}} = 0, \tag{48}$$

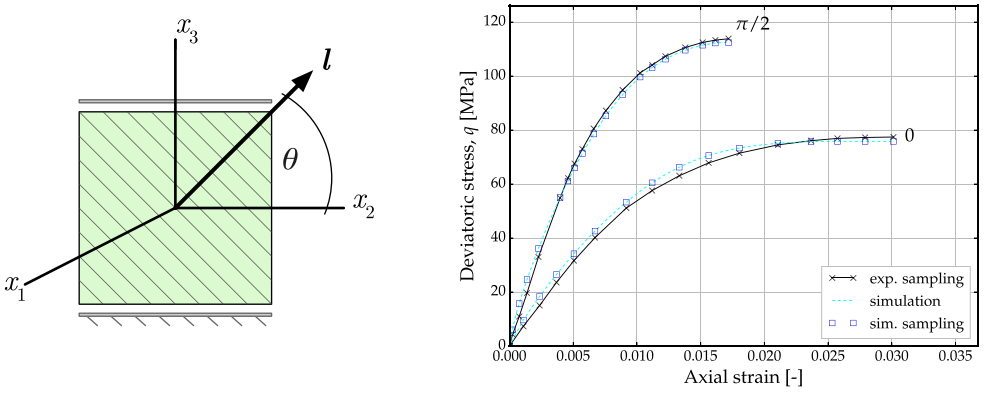

(a) Setup of the material point problem. **(b)** Confining stress $\sigma_c = -30$ MPa.

Fig. 31. Material point plasticity simulations, showing: (a) the problem geometry with microstructural angle $\theta_{\boldsymbol{l}}$ describing the angle between the microstructural direction and its projection onto the x_1-x_2 plane; and, (b) simulation curves labeled by $\theta_{\boldsymbol{l}}$, compared to sampled points from the experimental curve described by Niandou et al. [79].

where subscripting 0 indicates the initialization time and state. Solving, $p_{c\,0} = \min(p_{c\,0},\ \ p_0^* + q_0^{*\,2}/M^2 p_0)$. By use of the mapping tensor, used whilst computing the starred scalars, this method accounts for plastic anisotropy during initialization. Regarding Eq. (8), W_n^{p} at time zero is both ambiguous and without impact on the plasticity stress-return method's result. That is, because lacking the entire strain history, W_0^{p} at time zero is difficult to determine, even if the stored consolidation work can be approximated from Eq. (38). Further, given the material is elastically and plastically anisotropic, we anticipate the initial W_0^{p} to change with the microstructural direction (even between different simulations run at the same initial confining stress).

Thus an unwieldy quadratic case can be avoided by $\boldsymbol{b}_v = \boldsymbol{P}^{\mathrm{p\,vol}\,-1} : \mathbf{1}$, as highlighted in Eq. (31). This idea has advantages and disadvantages. On one hand, mapping the trace operator is nontraditional. Naturally, the purely volumetric definition of scalar ϵ_v^{p} also changes. On the other, mapping the trace-like constraint is somewhat akin to the concomitant mapping of both stress and back-stress into the plane-stress-space [81]. Hence it promotes both simplicity of initialization and conceptual consistency. This topic will be investigated in later work.

Regardless of the trace-like constraint for plasticity, the initial elastic strains are always computed in the same manner. For the simulations herein, some divergence-free isotropic stress state is read-in, with mean stress equal to the normal confining stress σ_c applied along the lateral boundaries. Elastic compliance $\boldsymbol{C}^{\mathrm{e}\,-1}$ is multiplied into the read-in isotropic stress tensor. In this manner, the elastic strains are initialized.

Appendix E. Material point calibration

We calibrate the local mapping against experimental curves describing Tournemire shale specimens undergoing compressive triaxial loading [79], as did [8]. Specifically they compared axial strain against deviatoric stress for various orientations of the local microstructural direction $\boldsymbol{l}$ at three confining pressures σ_c, using material point simulations. Our procedure is similar, in that we assume that the experimental specimens both are initially homogeneous and deform homogeneously. Under these assumptions, the experimental data for the Tournemire shale is applicably modeled by a material point simulation.

An optimization procedure was applied to simplify calibration. Loading is imposed as in Fig. 31(a), with a compressive confining pressure σ_c applied in the x_1-x_2 plane, and axial strain imposed in the x_3 direction. Microstructural direction $\boldsymbol{l}$ is parameterized w.r.t. microstructural angle $\theta_{\boldsymbol{l}}$ from the x_1-x_2 plane. For the initial optimization problem, confining pressure $\sigma_c = -40$ MPa was selected because: it is the lowest confining pressure with data available for all three microstructural angles $\theta_{\boldsymbol{l}} = 0, \pi/4, \pi/2$. Optimization of the calibration was performed with the NL2SOL algorithm [82] using the Dakota software toolkit as a driver program [83]. The objective function is set to minimize the difference between sampled experimental and simulation curve data points, Fig. 32(a).

From the initial calibration at $\sigma_c = -40$ MPa, the elastic material parameters obtained were $E = 25\,500$ MPa, $E_{\boldsymbol{l}} = 9070$ MPa, $\nu = 0.161$, $\nu_{\boldsymbol{l}} = 0.295$, and $\mu_{\boldsymbol{l}} = 2300$ MPa. Parenthetically, the most distinct trend observable

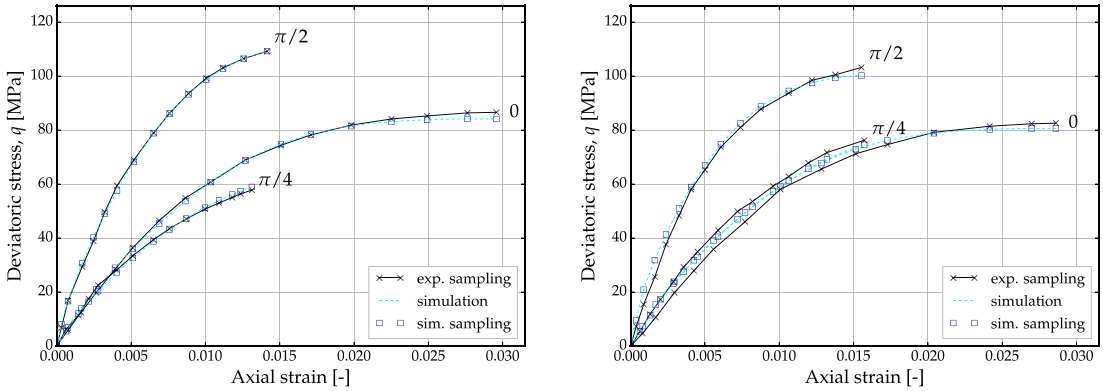

(a) Confining stress $\sigma_c = -40$ MPa. **(b)** Confining stress $\sigma_c = -50$ MPa.

Fig. 32. Simulation curves labeled by θ_l, compared to sampled points from the experimental curve described by Niandou et al. [79].

Table 3
Calibrated plasticity parameters.

σ_c [MPa]	C_d	α^{dev}	β^{dev}	α^{vol}	β^{vol}
−30	0.00202	0.883	0.542	0.819	0.988
−40	0.00178	0.942	0.631	0.784	0.866
−50	0.00211	1.17	0.739	0.917	0.992

during the initial optimization relates to the limited selection of the microstructural angles $\theta_l = 0, \pi/4, \pi/2$ and optimized value for μ_l. Simply put, due to the paucity of experimental curves available, changing modulus μ_l's value can move the $\theta_l = \pi/4$ curve, without effecting simulation results for either $\theta_l = 0$ or $\theta_l = \pi/2$. For this reason, the identical elastic parameters were applied during subsequent optimizations, at both confining pressures $\sigma_c = -30,\ -50$ MPa. Also, the critical state line's slope was fixed at $M = 1.0$, as was $\gamma^{\text{dev}} = \gamma^{\text{vol}} = 1.0$. Calibrated plasticity material parameters are presented in Table 3, using the results from Figs. 31(b) and 32, and assume constraint $\boldsymbol{b}_v = \mathbf{1}$.

As one important caveat, however, we highlight the rightward shifts of our simulation curves w.r.t the experimental data sets initial data point [79]. We attempt to use quantitatively the same shifts as applied in [8], in order to account for an initial fracture 'closure phase' associated with macroscopically apparent convex hardening. They interpret this closure phase concludes prior to the otherwise concave hardening towards the critical state. Heuristically however, we observe that selection of the initial experimental datum for simulation curve-fitting can significantly impact the calibrated plasticity parameter values.

In general, our calibrated material parameters agree reasonably with the results of Semnani et al. [8]. This is true for the elastic and plastic material parameters, and C_d in particular. We credit this agreeance to the use of an exponential stored consolidation work per Eq. (8), rather than the hyperbolic stored work proposed by Ortiz and Pandolfi [43], i.e.

$$W_c^{\text{p}} - W_{c\,0}^{\text{p}} = p_{c\,0} C_d \left[1 - \cosh\left(\frac{\epsilon_v^{\text{p}} - \epsilon_{v\,0}^{\text{p}}}{C_d} \right) \right].$$

In our experience, the hyperbolic law calibrated very different values of C_d, taking $\epsilon_{v\,0}^{\text{p}} = 0$ and for the same $p_{c\,0}$.

References

[1] G. Desbois, J.L. Urai, J.H. de Bresser, Fluid distribution in grain boundaries of natural fine-grained rock salt deformed at low differential stress (qom kuh salt fountain, central Iran): Implications for rheology and transport properties, J. Struct. Geol. 43 (2012) 128–143.
[2] K.C. Bennett, L.A. Berla, W.D. Nix, R.I. Borja, Instrumented nanoindentation and 3D mechanistic modeling of a shale at multiple scales, Acta Geotech. 10 (1) (2015) 1–14.
[3] K. Collins, A. McGown, The form and function of microfabric features in a variety of natural soils, Géotechnique 24 (2) (1974) 223–254.

[4] W. Weibull, A statistical distribution function of wide applicability, J. Appl. Mech. 18 (3) (1951) 293–297.
[5] M.S. Paterson, T.-f. Wong, Experimental rock deformation-the brittle field, Springer Science & Business Media, 2005.
[6] S. Na, W. Sun, M. Ingraham, H. Yoon, Effects of spatial heterogeneity and material anisotropy on the fracture pattern and macroscopic effective toughness of mancos shale in Brazilian tests, J. Geophys. Res.: Solid Earth 122 (8) (2017) 6202–6230.
[7] P. Habib, J. Bernaix, et al., The fissuration of rocks, in: 1st International Society for Rock Mechanics Congress, International Society for Rock Mechanics, 1966.
[8] S. Semnani, J. White, R. Borja, Thermoplasticity and strain localization in transversely isotropic materials based on anisotropic critical state plasticity, Int. J. Numer. Anal. Methods Geomech. 40 (18) (2016) 2423–2449.
[9] S. Forest, Nonlinear regularization operators as derived from the micromorphic approach to gradient elasticity, viscoplasticity and damage, Proc. R. Soc. A: Math. Phys. Eng. Sci. 472 (2188) (2016) 20150755.
[10] C. Miehe, S. Teichtmeister, F. Aldakheel, Phase-field modelling of ductile fracture: A variational gradient-extended plasticity-damage theory and its micromorphic regularization, Phil. Trans. R. Soc. A 374 (2066) (2016) 20150170.
[11] S. Forest, J. Mayeur, D. McDowell, Micromorphic crystal plasticity, Handb. Nonlocal Contin. Mech. Mater. Struct. (2018) 1–44.
[12] K. Bennett, R. Regueiro, D. Luscher, Anisotropic finite hyper-elastoplasticity of geomaterials with drucker-prager/Cap type constitutive model formulation, Int. J. Plast. (2019) in press.
[13] A. Stankiewicz, J. Pamin, Gradient-enhanced Cam-clay model in simulation of strain localization in soil, Found. Civil Environ. Eng. 7 (2006) 293–318.
[14] O.C. Zienkiewicz, A.H.C. Chan, M. Pastor, B.A. Schrefler, T. Shiomi, Computational Geomechanics, Wiley Chichester, 1999.
[15] W. Sun, J.T. Ostien, A.G. Salinger, A stabilized assumed deformation gradient finite element formulation for strongly coupled poromechanical simulations at finite strain, Int. J. Numer. Anal. Methods Geomech. 37 (16) (2013) 2755–2788.
[16] W. Sun, Q. Chen, J.T. Ostien, Modeling the hydro-mechanical responses of strip and circular punch loadings on water-saturated collapsible geomaterials, Acta Geotech. 9 (5) (2014) 903–934.
[17] W. Sun, A stabilized finite element formulation for monolithic thermo-hydro-mechanical simulations at finite strain, Internat. J. Numer. Methods Engrg. 103 (11) (2015) 798–839.
[18] K. Wang, W. Sun, A semi-implicit discrete-continuum coupling method for porous media based on the effective stress principle at finite strain, Comput. Methods Appl. Mech. Engrg. 304 (2016) 546–583.
[19] G. Scovazzi, B. Carnes, X. Zeng, S. Rossi, A simple, stable, and accurate linear tetrahedral finite element for transient, nearly, and fully incompressible solid dynamics: a dynamic variational multiscale approach, Internat. J. Numer. Methods Engrg. 106 (10) (2016) 799–839.
[20] K. Wang, W. Sun, A multiscale multi-permeability poroplasticity model linked by recursive homogenizations and deep learning, Comput. Methods Appl. Mech. Engrg. 334 (2018) 337–380.
[21] W. Sun, J.E. Andrade, Diffuse bifurcations of porous media under partially drained conditions, in: Multiscale and Multiphysics Processes in Geomechanics, Springer, 2011, pp. 61–64.
[22] W. Sun, A unified method to predict diffuse and localized instabilities in sands, Geomech. Geoeng. 8 (2) (2013) 65–75.
[23] A. Krischok, C. Linder, On the enhancement of low-order mixed finite element methods for the large deformation analysis of diffusion in solids, Internat. J. Numer. Methods Engrg. 106 (4) (2016) 278–297.
[24] A. Crook, J.-g. Yu, S. Willson, Development of an orthotropic 3D elastoplastic material model for shale, in: SPE/ISRM Rock Mechanics Conference, Society of Petroleum Engineers, 2002.
[25] S. Forest, Micromorphic approach for gradient elasticity, viscoplasticity, and damage, J. Eng. Mech. 135 (3) (2009) 117–131.
[26] F. Aldakheel, C. Miehe, Coupled thermomechanical response of gradient plasticity, Int. J. Plast. 91 (2017) 1–24.
[27] A. Schofield, P. Wroth, Critical state soil mechanics, Vol. 310, McGraw-Hill London, 1968.
[28] D.M. Wood, Soil behaviour and critical state soil mechanics, Cambridge university press, 1990.
[29] N. Abboud, G. Scovazzi, Elastoplasticity with linear tetrahedral elements: A variational multiscale method, Internat. J. Numer. Methods Engrg. 115 (8) (2018) 913–955.
[30] S. Reese, H. Bayat, S. Wulfinghoff, On an equivalence between a discontinuous Galerkin method and reduced integration with hourglass stabilization for finite elasticity, Comput. Methods Appl. Mech. Engrg. 325 (2017) 175–197.
[31] J. Cheng, A. Shahba, S. Ghosh, Stabilized tetrahedral elements for crystal plasticity finite element analysis overcoming volumetric locking, Comput. Mech. 57 (5) (2016) 733–753.
[32] M. Itskov, On the theory of fourth-order tensors and their applications in computational mechanics, Comput. Methods Appl. Mech. Engrg. 189 (2) (2000) 419–438.
[33] R. Borja, C. Tamagnini, CaM-clay plasticity, part III: Extension of the infinitesimal model to include finite strains, Comput. Methods Appl. Mech. Engrg. 155 (1–2) (1998) 73–95.
[34] L.J. Walpole, Fourth-rank tensors of the thirty-two crystal classes: multiplication tables, Proc. R. Soc. A: Math. Phys. Eng. Sci. 391 (1800) (1984) 149–179.
[35] K. Roscoe, A. Schofield, Mechanical behaviour of an idealized 'wet-clay', in: 2nd European Conference on Soil Mechanics and Foundation Engineering, Wiesbaden, 1963, pp. 47–54.
[36] R.I. Borja, Plasticity: Modeling & Computation, Springer-Verlag Berlin Heidelberg, 2013.
[37] K. Hashiguchi, M. Ueno, From hvorslev's failure criterion to failure condition, in: Proc. Intern. Conf. Soil Mech. and Found. Eng., 9th., Tokyo, Vol. 50, 1977, pp. 123–126.
[38] R. Butterfield, A natural compression law for soils (an advance on e-log p'), Géotechnique 29 (4) (1979).
[39] D.M. Potts, L. Zdravkovic, L. Zdravković, Finite element analysis in geotechnical engineering: application, Vol. 2, Thomas Telford, 2001.

[40] F. Hashagen, R. de Borst, Enhancement of the hoffman yield criterion with an anisotropic hardening model, Comput. Struct. 79 (6) (2001) 637–651.
[41] D. Versino, K.C. Bennett, Generalized radial-return mapping algorithm for anisotropic von mises plasticity framed in material eigenspace, Internat. J. Numer. Methods Engrg. 116 (3) (2018) 202–222.
[42] J. Simo, Numerical analysis and simulation of plasticity, Handb. Numer. Anal. (1998) 183–499.
[43] M. Ortiz, A. Pandolfi, A variational Cam-clay theory of plasticity, Comput. Methods Appl. Mech. Engrg. 193 (27–29) (2004) 2645–2666.
[44] K. Weinberg, A. Mota, M. Ortiz, A variational constitutive model for porous metal plasticity, Comput. Mech. 37 (2) (2006) 142–152.
[45] J. Simo, T. Hughes, Computational Inelasticity, Springer-Verlag New York, 1998.
[46] C. Miehe, F. Aldakheel, S. Mauthe, Mixed variational principles and robust finite element implementations of gradient plasticity at small strains, Int. J. Numer. Methods Eng. 94 (11) (2013) 1037–1074.
[47] F. Aldakheel, Micromorphic approach for gradient-extended thermo-elastic–plastic solids in the logarithmic strain space, Contin. Mech. Thermodyn. 26 (6) (2017) 1207–1217.
[48] K. Wang, W. Sun, S. Salager, S. Na, G. Khaddour, Identifying material parameters for a micro-polar plasticity model via x-ray micro-CT images: lessons learned from the curve-fitting exercises, Int. J. Multiscale Comput. Eng. 14 (4) (2016) 389–413.
[49] J. Clayton, J. Knap, Phase field modeling of directional fracture in anisotropic polycrystals, Comput. Mater. Sci. 98 (2015) 158–169.
[50] S. Teichtmeister, D. Kienle, F. Aldakheel, M. Keip, Phase field modeling of fracture in anisotropic brittle solids, Int. J. Non-Linear Mech. 97 (2017) 1–21.
[51] E.C. Bryant, W. Sun, A mixed-mode phase field fracture model in anisotropic rocks with consistent kinematics, Comput. Methods Appl. Mech. Engrg. 342 (2018) 561–584.
[52] M. Ortiz, L. Stainier, The variational formulation of viscoplastic constitutive updates, Comput. Methods Appl. Mech. Engrg. 171 (3–4) (1999) 419–444.
[53] Q. Yang, L. Stainier, M. Ortiz, A variational formulation of the coupled thermo-mechanical boundary-value problem for general dissipative solids, J. Mech. Phys. Solids 54 (2) (2006) 401–424.
[54] F. Armero, J. Simo, A new unconditionally stable fractional step method for non-linear coupled thermomechanical problems, Internat. J. Numer. Methods Engrg. 35 (4) (1992) 737–766.
[55] M. Wheeler, T. Wick, W. Wollner, An augmented-Lagrangian method for the phase-field approach for pressurized fractures, Comput. Methods Appl. Mech. Engrg. 271 (2014) 69–85.
[56] C. Miehe, M. Hofacker, F. Welschinger, A phase field model for rate-independent crack propagation: Robust algorithmic implementation based on operator splits, Comput. Methods Appl. Mech. Engrg. 199 (45) (2010) 2765–2778.
[57] C. Miehe, M. Hofacker, L.-M. Schänzel, F. Aldakheel, Phase field modeling of fracture in multi-physics problems. part ii. coupled brittle-to-ductile failure criteria and crack propagation in thermo-elastic–plastic solids, Comput. Methods Appl. Mech. Engrg. 294 (2015) 486–522.
[58] J. Choo, W. Sun, Coupled phase-field and plasticity modeling of geological materials: from brittle fracture to ductile flow, Comput. Methods Appl. Mech. Engrg. 330 (2017) 1–32.
[59] E. de Souza Neto, D. Peric, D. Owen, Computational Methods for Plasticity, John Wiley & Sons, Ltd, 2008.
[60] W. Bangerth, R. Hartmann, G. Kanschat, Deal.ii – a general purpose object-oriented finite element library, ACM Trans. Math. Software 33 (4) (2007) 24/1–24/27.
[61] J.A. White, R.I. Borja, Stabilized low-order finite elements for coupled solid-deformation/fluid-diffusion and their application to fault zone transients, Comput. Methods Appl. Mech. Engrg. 197 (49–50) (2008) 4353–4366.
[62] J. Choo, J.A. White, R.I. Borja, Hydromechanical modeling of unsaturated flow in double porosity media, Int. J. Geomech. 16 (6) (2016) D4016002.
[63] R. Borja, Conditions for instabilities in collapsible solids including volume implosion and compaction banding, Acta Geotech. 1 (2) (2006) 107–122.
[64] A. Mota, Q. Chen, J. Foulk, J. Ostien, Z. Lai, A Cartesian parametrization for the numerical analysis of material instability, Internat. J. Numer. Methods Engrg. 108 (2) (2016) 156–180.
[65] S. Reese, P. Wriggers, A stabilization technique to avoid hourglassing in finite elasticity, Internat. J. Numer. Methods Engrg. 48 (1) (2000) 79–109.
[66] J.-S. Chen, S. Yoon, C.-T. Wu, Non-linear version of stabilized conforming nodal integration for Galerkin mesh-free methods, Internat. J. Numer. Methods Engrg. 53 (12) (2002) 2587–2615.
[67] Y. Liu, W. Sun, Z. Yuan, J. Fish, A nonlocal multiscale discrete-continuum model for predicting mechanical behavior of granular materials, Internat. J. Numer. Methods Engrg. 106 (2) (2016) 129–160.
[68] J. Choo, S. Lee, Enriched Galerkin finite elements for coupled poromechanics with local mass conservation, Comput. Methods Appl. Mech. Engrg. 341 (2018) 311–332.
[69] K. Ikeda, Y. Yamakawa, S. Tsutsumi, Simulation and interpretation of diffuse mode bifurcation of elastoplastic solids, J. Mech. Phys. Solids 51 (9) (2003) 1649–1673.
[70] Y. Tien, M. Kuo, C. Juang, An experimental investigation of the failure mechanism of simulated transversely isotropic rocks, Int. J. Rock Mech. Min. Sci. 43 (8) (2006) 1163–1181.
[71] H. Oku, B. Haimson, S.-r. Song, True triaxial strength and deformability of the siltstone overlying the chelungpu fault (chi-chi earthquake), Taiwan, Geophys. Res. Lett. 34 (9) (2007) 293–304.
[72] A. Vachaparampil, A. Ghassemi, Failure characteristics of three shales under true-triaxial compression, Int. J. Rock Mech. Min. Sci. 100 (2017) 151–159.
[73] K. Bennett, L. Berla, W. Nix, R. Borja, Instrumented nanoindentation and 3D mechanistic modeling of a shale at multiple scales, Acta Geotech. 10 (1) (2015) 1–14.

[74] W. Ehlers, B. Scholz, An inverse algorithm for the identification and the sensitivity analysis of the parameters governing micropolar elasto-plastic granular material, Arch. Appl. Mech. 77 (12) (2007) 911.
[75] C. Miehe, N. Apel, M. Lambrecht, Anisotropic additive plasticity in the logarithmic strain space: modular kinematic formulation and implementation based on incremental minimization principles for standard materials, Comput. Methods Appl. Mech. Engrg. 191 (47–48) (2002) 5383–5425.
[76] P. Neff, I.-D. Ghiba, Loss of ellipticity for non-coaxial plastic deformations in additive logarithmic finite strain plasticity, Int. J. Non-Linear Mech. 81 (2016) 122–128.
[77] J. Dellinger, D. Vasicek, C. Sondergeld, Kelvin notation for stabilizing elastic-constant inversion, Rev. Inst. Français Pétrole 53 (5) (2006) 709–719.
[78] V. Lubarda, M. Chen, On the elastic moduli and compliances of transversely isotropic and orthotropic materials, J. Mech. Mater. Struct. 3 (1) (2008) 153–171.
[79] H. Niandou, J. Shao, J. Henry, D. Fourmaintraux, Laboratory investigation of the mechanical behaviour of tournemire shale, Int. J. Rock Mech. Min. Sci. 34 (1) (1997) 3–16.
[80] I. Kunin, An algebra of tensor operators and its applications to elasticity, Internat. J. Engrg. Sci. 19 (12) (1981) 1551–1561.
[81] J. Simo, R. Taylor, A return mapping algorithm for plane stress elastoplasticity, Internat. J. Numer. Methods Engrg. 22 (3) (1986) 649–670.
[82] J. Dennis, D. Gay, R. Welsch, Algorithm 573: Nl2sol – an adaptive nonlinear least-squares algorithm [e4], ACM Trans. Math. Software 7 (3) (1981) 369–383.
[83] B. Adams, M. Ebeida, M. Eldred, G. Geraci, J. Jakeman, K. Maupin, J. Stephens, J. Monschke, L. Swiler, D. Virgil, T. Wildey, D. Gay, W. Bohnhoff, K. Dalbey, J. Eddy, J. Frye, R. Hooper, K. Hu, P. Hough, M. Khalil, E. Ridgway, J. Winokur, DAKOTA, a multilevel parallel object-oriented framework for design optimization, parameter estimation, uncertainty quantification, and sensitivity analysis: Version 6.8 users manual. Technical report, Sandia National Laboratories, 2018.